Electrochemical Energy Reviews (2024) 7:17
https://doi.org/10.1007/s41918-024-00215-y

REVIEW ARTICLE

Recent Progress in Sodium-Ion Batteries: Advanced Materials, Reaction Mechanisms and Energy Applications

Yujun Wu[1] · Wei Shuang[1] · Ya Wang[1] · Fuyou Chen[1] · Shaobing Tang[1] · Xing-Long Wu[2,3] · Zhengyu Bai[1] · Lin Yang[1] · Jiujun Zhang[4,5]

Received: 12 February 2023 / Revised: 13 September 2023 / Accepted: 2 December 2023

Abstract

For energy storage technologies, secondary batteries have the merits of environmental friendliness, long cyclic life, high energy conversion efficiency and so on, which are considered to be hopeful large-scale energy storage technologies. Among them, rechargeable lithium-ion batteries (LIBs) have been commercialized and occupied an important position as secondary batteries due to their high energy density and long cyclic life. Nevertheless, the uneven distribution of lithium resources and a large number of continuous consumptions result in a price increase for lithium. So, it is very crucial to seek and develop alternative batteries with abundant reserves and low cost. As one of the best substitutes for widely commercialized LIBs, sodium-ion batteries (SIBs) display gorgeous application prospects. However, further improvements in SIB performance are still needed in the aspects of energy/power densities, fast-charging capability and cyclic stability. Electrode materials locate at a central position of SIBs. In addition to electrode materials, electrolytes, conductive agents, binders and separators are imperative for practical SIBs. In this review, the latest progress and challenges of applications of SIBs are reviewed. Firstly, the anode and cathode materials for SIBs are symmetrically summarized from aspects of the design strategies and synthesis, electrochemical active sites, surrounding environments of active sites, reaction mechanisms and characterization methods. Secondly, the influences of electrolytes, conductive agents, binders and separators on the electrochemical performance are elucidated. Finally, the technical challenges are summarized, and the possible future research directions for overcoming the challenges are proposed for developing high performance SIBs for practical applications.

Keywords Sodium-ion batteries · Design strategies and synthesis · Active sites · Reaction mechanism · Characterization methods

✉ Zhengyu Bai
baizhengyu@htu.edu.cn

✉ Lin Yang
yanglin@htu.edu.cn

✉ Jiujun Zhang
jiujun.zhang@i.shu.edu.cn

[1] Collaborative Innovation Center of Henan Province for Green Manufacturing of Fine Chemicals, Key Laboratory of Green Chemical Media and Reactions, Ministry of Education, School of Chemistry and Chemical Engineering, Henan Normal University, Xinxiang 453007, Henan, China

[2] MOE Key Laboratory for UV Light-Emitting Materials and Technology, Northeast Normal University, Changchun 130024, Jilin, China

[3] Key Laboratory of Organo-Pharmaceutical Chemistry of Jiangxi Province, Gannan Normal University, Gan Zhou 341000, Jiangxi, China

[4] College of Materials Science and Engineering, Fuzhou University, Fuzhou 350108, Fujian, China

[5] College of Sciences, Institute for Sustainable Energy, Shanghai University, Shanghai 200444, China

Published online: 07 May 2024

1 Introduction

In an effort to mitigate the fast exhaustion of unrenewable fossil fuels and the associated environmental pollution, a shift from fossil fuels to green and renewable energy sources has been observed throughout the world [1–3]. Therefore, it is imperative to explore renewable and green energy sources, for example solar energy, waterfall energy, wind energy, etc. Unfortunately, these sustainable energy sources are weather dependent, and the energy generated from them is intermittent, which limits their further practical applications. Hence, it is necessary to find and develop the corresponding technologies to store and then convert this intermittent energy for easy usage [4, 5]. In this regard, energy storage and conversion systems based on battery technologies, especially lithium-ion batteries (LIBs), have been advanced fast. LIBs were first commercialized in 1991 and were dominant in secondary batteries. The growing market for LIBs would inevitably bring the scarcity of Li resources and a costly price rise as a result of their limited abundance. The scarcity of lithium results in the difficulty for LIBs to meet both electric vehicles and other massive energy storage. Hence, it is very necessary to develop other energy storage technologies with low-cost and plentiful reserves. In this regard, sodium-ion batteries (SIBs) are a decent substitution for LIBs. In fact, SIBs were developed as early as in the 1980s along with LIBs. Due to their lower energy density than LIBs, research on SIBs has been almost stalled for the next 20 years [6]. SIBs have been back in the spotlight of the people and have evolved rapidly since the 2010s [7] because of their attractive advantages: (1) there is an abundance of Na resources on the Earth [8]; (2) Na^+ ions have a fast diffusion in the solid phase, making a superior performance of SIBs; (3) Al foil as the current collector in SIB anodes not only can reduce the price, but also can reduce the battery mass and over-discharge problems for providing safe battery shipping [8]; and (4) the cathode has high safety even in highly charged states.

Electrode materials, electrolytes, conductive agents, binders and separators are of prime importance for SIBs. The cathode materials and anode materials play crucial roles in the electrochemical performance. These cathode materials are essentially classified into layer transition oxides, organic compounds, Prussian blue analogues (PBAs) and polyanionic compounds, for example, phosphates, fluorosulfates, pyrophosphates and oxychlorides [9]. In recent years, the research on cathode materials has developed rapidly, and a series of new materials with excellent properties have been discovered, including high-entropy materials. In order to reduce environmental pollution, cathode materials tend to be developed as cobalt-free materials. SIB anode materials are essentially classified into four types on the basis of the charge/discharge reaction mechanisms: the metal type of sodium anodes, the insertion reaction type (carbon-based materials and titanium oxides), the alloying reaction type (tin, silicon, antimony, germanium, phosphorus, etc.) and the conversion reaction type (metal oxides, metal sulfides, metal phosphides, etc.) [10]. Some new types of anodes have been developed in recent years. These new anode materials contain multiple reaction pathways with multiple active sites. It is worth emphasizing that metal–organic frameworks (MOFs) as anodes of SIB have gained more and more attention in recent years. MOFs as inorganic–organic hybrids can provide multiple active sites. Both organic ligands and metal nodes can be active sites to provide specific capacity. However, the reaction mechanism of MOFs as anode materials still lacks deep investigation. Along with the electrode materials, electrolytes, conductive agents and binders are also vital in the improvement in SIBs. The electrolyte generally contains ether electrolyte and ester electrolyte. So as to promote electrochemical performance, new types of additive agents are also explored. Common conductive conductors include super-P, acetylene black (AB) and ketjen black (KB). SIB binders are mainly polyvinylidene fluoride (PVDF), polyacrylic acid (PAA), polyvinyl alcohol (PVA) and carboxymethyl cellulose (CMC). It should be emphasized that there is still large room for developing SIBs [11]. Electrode materials, electrolytes, conductive agents, binders and separators still need to be improved and optimized in light of the cycle-life, energy density and security of SIBs. With the purpose of improving the performance of SIBs, more and more researches are focusing on reaction mechanisms at the atomic and molecular levels.

The research community may need a systematic review to summarize the latest progress of SIBs owing to the recent intense spike in research interest. SIBs have been significantly developed with high volumes of progress being published almost every week in the current time [12]. This review summarizes the research progress of SIBs in the last five years. The review mainly in depth reviews the design strategies and fabrication of SIB electrode materials, the influences of electrodes on electrochemical performance and the reaction mechanisms. Meanwhile, the influences of electrolytes, conductive agents, binders and separators on electrochemical performance are elucidated. The contents of this review are different from those of previously reported reviews in the aspects of molecular and atomic scales, reaction mechanisms of electrochemical active sites (such as metal sites, anion sites, organic groups C = O, C = N, and N = N which possess electrochemical activity, participate in electrochemical reaction, and contribute specific capacity), surrounding environments of active sites and the latest characterization methods. We believe that the review can deliver meaningful opinions for developing SIBs. The structure diagram of the review is shown in Fig. 1.

2 Cathode Materials

To achieve extraordinary performance, SIB cathode materials are the critical point to improve the SIB specific energy and promote their practical application. These cathode materials are essentially classified into layer transition metal oxides, polyanionic compounds, PBAs and organic compounds.

2.1 Layered Transition Metal Oxides

Layered sodium transition metal oxides Na_xMO_2 ($0.5 \leqslant x \leqslant 1$, M: Mn, Fe, Cr, Co, Ni, Cu, etc.) possess a facile synthesis process, amazing theoretical specific capacity (~220−270 mAh g^{-1}), excellent ionic conductivity and so on. These advantages make layered Na_xMO_2 one of the commonest SIBs cathode materials. In 1980, Hagenmuller et al. reported on the layered Na_xCoO_2 with four different structures [13]. Delmas and Hagenmuller et al. also reported the structural classification and characteristics of the layered metal oxides in 1980 [14]. The crystal structures of the layered Na_xMO_2 are named along with the coordination environment of Na^+ and the packing sequence of oxygen atom. For each phase, Na^+ ions are introduced with octahedral (O) or trigonal prismatic (P) environment between the MO_6 edge-sharing octahedra to obtain $(MO_2)_n$ sheets. Layered Na_xMO_2 mostly includes P2-phase, P3-phase, O2-phase and O3-phase (as shown in Fig. 2). The number is the stacking layer of the least repeated unit of oxygen. Among them, P2-phase and O3-phase are widely studied, because many O3 and P2 cathode materials show impressive high capacities with nearly 40%–60% of the theoretical value (~120–150 mAh g^{-1}) and superior cyclic performance in the voltage range of about 1.5–4.1 V [9]. The active sites of the layered oxides are often transition metals. The structure, surface and doped metal influence their activity of transition metals. In this section, the design strategies and synthesis method, active sites and surrounding environments of active sites, and the reaction mechanism of the layered oxides are summarized.

2.1.1 Design Strategies and Synthesis Method

As cathode materials, the conductivity, robustness, stability and active sites play big roles in the electrochemical performance. Hence, design strategies should be considered to increase the conductivity, robustness and stability of the cathode materials. Coating and composition with a conductive matrix (graphene, carbon nanotubes, conductive polymers, etc.) are useful ways to increase the conductivity, robustness and stability of the cathode materials [15]. For transition metal oxide cathodes, irreversible harmful phase transitions are common. The metal ion doping strategy was previously shown to be an effective method to avoid detrimental and irreversible phase transition. Solid-state reaction and co-precipitation are common methods for synthesizing the transition metal oxide cathodes. The sol-gel method, solvothermal method and electrospinning method are also adopted to synthesize transition metal oxides cathodes, but they are less common than the solid-state reaction and the co-precipitation method. The obtained transition metal oxides cathodes usually need to be preserved in one argon-filled glovebox to isolate them from moisture and air atmosphere. The solid-state reaction is mixed sodium carbonate (Na_2CO_3) and Na_xCoO_2 (manganese oxide, iron oxide, nickel oxides, and copper oxide, etc.) with stoichiometric ratios, and then, the mixture is ground by ball mill. The mixture is pressed into pellets and then annealed in the air atmosphere usually between 850 and 1 000 °C. Sodium sources should be oversupplied 5% to make up for the loss during calcination [16]. The co-precipitation is to mix metal salt solutions with alkali solution with stoichiometric ratios under heated or room temperature and stirring condition to obtain precipitates $TM(OH)_2$. The $TM(OH)_2$ precursor is centrifuged, washed and dried. The obtained $TM(OH)_2$ precursor is mixed with Na_2CO_3 and Li_2CO_3 with stoichiometric ratios and milled, then calcined at relatively low temperature (500 °C) to remove impurities. Finally, the mixture is ground and pressed into pellets to be calcined at high temperature (usually 850–1 000 °C) in air [17]. The sol-gel method usually involves adding a metal acetate solution into a citric acid solution at room temperature or heated for some time to get wet gel. Next, the above gel is dried just to get the dry gel. Lastly, the dry gel is calcined in air at high temperature (usually 850–1 000 °C) [18, 19]. The electrospinning synthesis steps are as follows: metal acetate and sodium salts are added into a polyvinylpyrrolidone (PVP) solution by stirring overnight; then, the viscous solution is fed into a plastic syringe. The solution is electrospun on an Al film under a high voltage. The film is peeled off from the Al film and calcined at high temperature (usually 850–1 000 °C) in the air [20].

2.1.2 Active Sites and Surrounding Environments of Active Sites

Although the layered Na_xMO_2 materials are one of the most studied cathodes of SIBs, their inferior air stability, sluggish kinetics and detrimental phase transition during charge/discharge limit their further commercial application. In order to improve and solve these problems, structural optimization [21, 22], surface coating [23], ionic doping and replacement [16, 24, 25] are mostly adopted. In the layered Na_xMO_2 cathodes, the active sites are mostly metal with variable valence states. Partial anionic ions can be activated by ionic doping and replacement. The surrounding environments of active

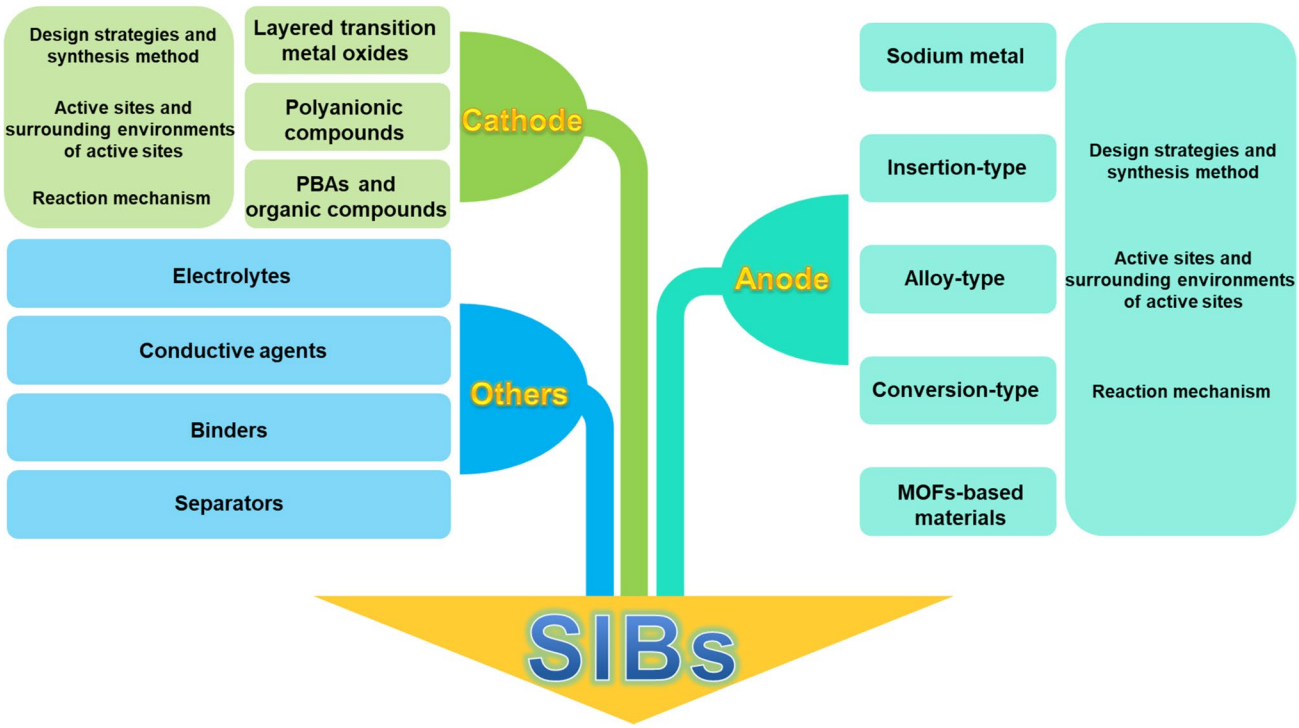

Fig. 1 Structure diagram of the review

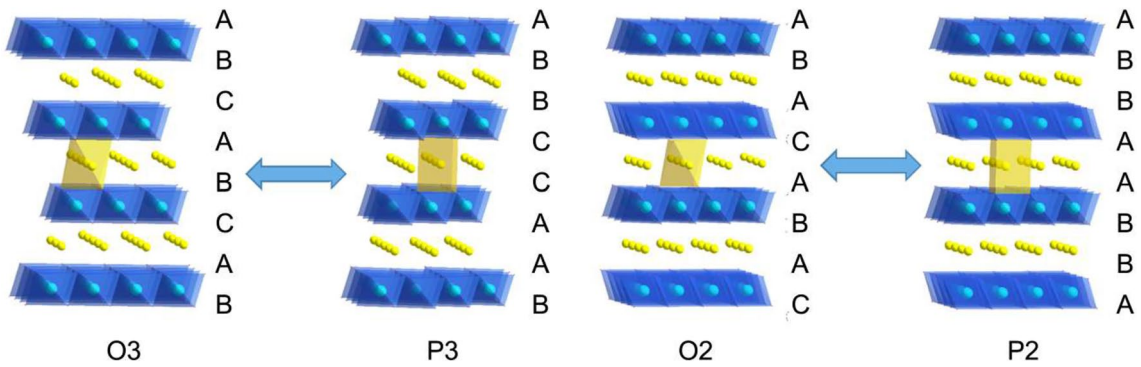

Fig. 2 Crystal structure illustration of layered oxides with O3, P3, O2, P2 structures. Adapted with permission from Ref. [9]. Copyright©2008, Beijing University Press

sites (structural adjustment, surface coating, ionic doping and replacement, etc.) have a great influence on the active sites.

Among the disadvantages of the layered Na_xMO_2, detrimental and irreversible phase transition during charge/discharge frequently occurs, which should be addressed first. Cationic doping or replacement (including active and inactive cations) is usually adopted. Cations prefer to substitute TM sites because the radiuses of TM ions are closer to these substituted cations than those of Na^+ ions. Inactive Li doping was previously proved an effective method to avoid detrimental and irreversible phase transition. Arumugam Manthiram's group reported Li-substituted O3-type layered Na_xMO_2. Because of the low overlap between the O 2p and Li 1s orbitals, the doping of Li could decrease the coordination numbers of the O atom. Thus, the other coordinate bonds of O–TM were strengthened, and the Ni–O bond was significantly enhanced. Hence, the doping of Li into TM sites could decrease the Jahn–Teller effect of the active site (Ni), further suppressed the undesirable P3-P'3 phase change at high voltage. Additionally, the doping of Li could also effectively suppress the development of metal fluorides upon the surface of cathodes, which reduced the damage of active metal ions. Because of

the dual functions, the Li-doped layered Na_xMO_2 cathodes showed a high-voltage performance with an extraordinary reversible capacity [24]. Similar effects of doped Li were common and also reported by other groups. For example, Chen and co-workers reported P2-$Na_x(Li_yMn_{1-y})O_2$ cathodes with a single phase pathway [16]. In 2021, Yu and co-workers studied Na^+ ion kinetics and thermodynamics in P2-type oxygen redox Mn-Ni layered oxides operated through Li substitution, while Ni ions were the active site. The Li substitution suppressed the phase transition and accelerated the migration of Na^+ [26]. The double and multiple doping of Li and other active and inactive metals were also commonly reported to suppress detrimental phase transition. Chen and co-works reported inactive Li and active Fe co-doped P2-$Na_{0.66}Li_{0.18}Fe_{0.12}Mn_{0.7}O_2$ cathode. From Fig. 3a, the synchrotron X-ray diffraction (SXRD) preferred occupancy at the Na_e site, and the peaks at 4.02 Å were indexed to the "1/3 1/3 0" superlattice. The inset of Fig. 3a presented that Li located in TM position. The neutron diffraction (ND) data (Fig. 3b) showed that there was no long-range assembling between Fe and Mn. The active sites were Mn ions and Fe ions. The Li dopant could eliminate the irreversible and adverse P2-O2 phase transition. The Fe dopant could diminish the Li escape from the TM layer; thus, Li was efficiently reserved in the lattice with partially reversibly transfer between the Na^+ layer and TM layer. The Li-doped cathode showed an extraordinary capacity of 190 mAh g^{-1} and an excellent retention rate of ~ 87% over 80 cycles in a broad voltage window of 1.5–4.5 V (as shown in Fig. 3e) [16]. In 2022, Wang's group explored the effects of inactive Li and Zn co-doping on the performance of P2-type $Na_{0.7}Li_{0.06}Zn_{0.06}Ni_{0.21}Mn_{0.67}O_2$ cathode. Li and Zn occupied partial Ni^{2+} sites, which could increase the lattice spacing to speed up the transfer of Na^+ ions. What's more, Li and Zn co-substitution restrained the Jahn–Teller effect of active Mn^{3+} to avoid the phase transition of P2-O2. As a result, the as-prepared cathode presented a superb cyclic stability (91.9% retention after 100 cycles) [27].

In addition to stabilizing the structure and inhibiting harmful phase transitions of cathodes, Li substitution also has the effect of stimulating the redox reaction of anions to provide capacity. In 2022, Liu and co-workers obtained low-cost layered oxide cathode with a solid-solution reaction during the charge/discharge process. In addition to Mn^{3+}/Mn^{4+} active sites and Fe^{3+}/Fe^{4+} active sites, O^{2-}/$(O_2)^{n-}$ sites were also active. The O 2p states nearby the Fermi level could be promoted by Li dopant and vacancy in the TM layer to trigger the redox reaction of O^{2-}/$(O_2)^{n-}$ [28].

The doping of Fe, Ni, Co, Zn, Cu, Zr, etc. into TM is also usually reported, in addition to the doping of Li. Liu's group adopted Zr^{4+} doping to adjust the redox reaction of anion and crystal structure stability of O3-type layered oxide cathode in 2021 [23]. The strong bonding of Zr–O made the TM–O short, and made the Na–O long, which enlarged the Na layer resulting in an easy transfer of Na^+ and stability of the structure. Zhou's group obtained O3-type Ru-doped Cr-based layered oxide cathode with excellent cycling stability with super capacity retention (80.7%) after 1 100 cycles in 2019. The Ru ion has a great attraction for electrons, resulting in the decrease in the electronic density of the neighboring Cr ion. Thus, the transfer tendency of electrons from Cr cation to O anion was lowered, which effectively inhibited the disproportionation reaction and the migration of active sites Cr ions. The Ru-doping NCRO electrode delivered an enhanced discharge capacity (156 mAh g^{-1} at 0.5 C), which had a reversible O3-P3 phase transition [29]. Metal substitution could also induce abnormal layered-tunnel hetero-structure. Xiao et al. adopted an optimized crystal structure engineering regulation method to obtain an abnormal layered-tunnel hetero-structure which named $Na_{0.44}Co_{0.1}Mn_{0.9}O_2$ cathode material through Co doping. The XRD results (Fig. 3c) showed that the cathode material possessed P2 phase possessing the space group *P63/mmc* with JCPDS: 27-0752 and the tunnel phase having the space group *Pbma* with JCPDS: 27-0750. The crystal structure is shown in Fig. 3d. The unique abnormal layered-tunnel hetero-structure could reduce the Jahn–Teller effect and realize the contribution of both the diffusion-controlled course and capacitive controlled course. Benefiting from the novel structure, the electrochemical performance was enhanced. The cathode material showed an energy density of 296.5 Wh kg^{-1} and a remarkable specific capacity of 108.3 mAh g^{-1} even at 5 C. The full cell system with $Na_{0.44}Co_{0.1}Mn_{0.9}O_2$ as cathode showed a great specific energy of 453.9 Wh kg^{-1} and a reversible specific capacity of 171.6 mAh g^{-1} and at 0.2 C (Fig. 3f) [21]. In recent years, high-entropy compounds including layered oxide become a research hotspot. The high-entropy compounds are single-phase solid solutions that include five or more than five types of metals. The high-entropy compounds show some specific properties. For example, the increased entropy enhances structural stability, heat/air stability and electronic conductivity. Chen's group reported a high-entropy $NaCu_{0.1}Ni_{0.3}Fe_{0.2}Mn_{0.2}Ti_{0.2}O_2$ cathode material with an O3-type layer-structure with a reversible capacity of 130 mAh g^{-1} and outstanding long cyclic performance (nearly 71% retention rate after 500 cycles at 0.5 C). In the high-entropy cathode, Fe, Cu and Ni ions were active, while Mn^{4+} and Ti^{4+} were inactive to stabilize the structure [25].

In most cases, metal is doped in the TM layer, and few literatures reported metal substitution on the Na site. The Li would prefer to substitute the Na^+ site in the case where the high oxidation states of TM are not stable. Kim and Jung reported the doping of Li at the Na site of layered $Na_x[Fe_yMn_{1-y}]O_2$ by adjusting the composition of TM for

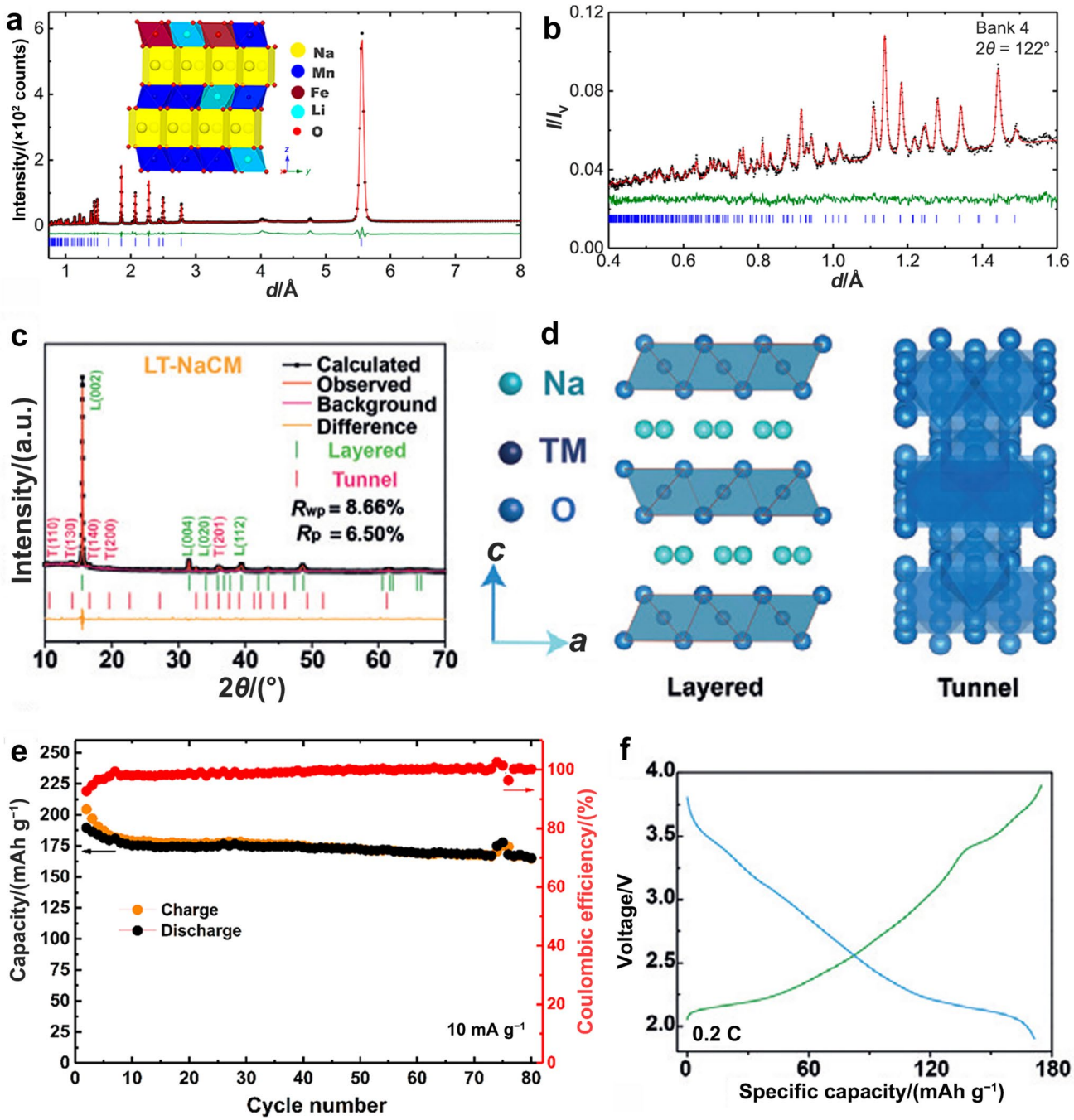

Fig. 3 **a** Synchrotron XRD, inset of **a** crystal structure, **b** neutron diffraction patterns and Rietveld refinement plot and **e** cyclic performance of P2-$Na_{0.66}Li_{0.18}Fe_{0.12}Mn_{0.7}O_2$ cathode. Adapted with permission from Ref. [16]. Copyright©2019, American Chemical Society. **c** XRD pattern, **d** crystal structures of tunnel and layered phases of the LTNaCM and **f** charge/discharge plots vs. specific capacity at 0.2 C of the LTNaCM as cathode in full cell. Adapted with permission from Ref. [21]. Copyright©2020, Wiley–VCH

the first time in 2018 [30]. Li at the Na site could not only stabilize the layered structure but also lower the energy barrier of Na-hopping. Other metals such as Ca substituted in Na sites have also been reported. The Ca^{2+} ions substituted in Na sites acted as pillars to avoid the gliding of TM layers. In addition, the strong Ca–O bonding could further suppress the loss of oxygen [28].

Decomposition of the electrolyte, interface side reactions, structural degradation, electrode cracking and TM dissolution can result in the interfacial failure of cathode/

electrolyte, which further leads to the poor electrochemical performance. Surface coating is a helpful method to solve these problems. In 2021, Xiao's group adopted an atomic layer deposition (ALD) metal oxide protective layer to inhibit the interfacial failure. The Al_2O_3 ALD could avoid the HF attack from the electrolyte to protect cathode and resist the side reaction [31]. In 2021, Liu reported that the ZrO_2 coating could effectively relieve the corrosion of electrolyte and inhibit the formation of Na_2CO_3 to keep the structural integrity. The XRD results showed that the peaks at about 28.0° and 31.3° were indexed to the ZrO_2 (*P*2/*c*). Moreover, the transmission electron microscope (TEM) and scanning electron microscope (SEM) further suggested the coating of ZrO_2 layer on the surface. Benefitting from the ZrO_2 layer and Zr^{4+} doping, the cycling stability and specific capacity of ZrO_2@MFN were larger than those of MFN at diverse voltages [23]. Besides the above strategies, the synthesis of biphasic cathode can also enhance the cycling stability. For example, Xiao [31], Adelhelm [18], Tang [32] etc. reported the biphasic strategy to improve the electrochemical performance.

2.1.3 Reaction Mechanism

The layered Na_xMO_2 cathodes usually have phase transformation during the charge/discharge process. The active sites of the layered Na_xMO_2 cathodes are transition metals with variable valences. The in situ and ex situ characterizations combined with density functional theory (DFT) calculations are adopted to investigate and reveal the electrochemical reaction mechanism of the cathode materials. The XRD measurement is the most common way to characterize the phase transition. The X-ray absorption spectroscopy and X-ray photoelectron spectroscopy spectrometer (XPS) are common methods to verify the valence change of metals. The operando synchrotron XRD of the P2-$Na_{2/3}(Mn_{6/8}Ni_{2/8})O_2$ and P2-$Na_{2/3}(Li_{1/8}Mn_{5/8}Ni_{2/8})O_2$ (as shown in Fig. 4a–f) illustrated the impact of Li-doping on the phase conversion in the charge and discharge course. The shifts of (112) peaks of the P2-$Na_{2/3}(Mn_{6/8}Ni_{2/8})O_2$ cathode were not continuous at high voltage, as shown in the area among two green patterns in Fig. 4c. What's more, new weak peaks developed at 12.3° and 68.4° of P2-type $Na_{2/3}(Mn_{6/8}Ni_{2/8})O_2$ cathode material. The peak at 68.4° was from the stacking faults of (112) in O2-type structure. The operando synchrotron XRD results showed that the P2-type $Na_{2/3}(Mn_{6/8}Ni_{2/8})O_2$ cathode material that at the high voltage state experienced a two phase reaction. In contrast, the XRD peaks of the Li-doped P2-$Na_{2/3}(Li_{1/8}Mn_{5/8}Ni_{2/8})O_2$ cathode showed continuous shifts during the all charge/discharge process, and no phase splitting or new peaks, which indicated a quasi-solid-solution reaction [26]. TEM and STEM are also used to characterize the phase evolution in detail. For instance, Lu and team members studied the lattice fringes of the NFMO-P2/O3 cathode material of 100 cycles by STEM, which indicated that the NFMO-P2/O3 cathode still kept P2/O3 phase coexisting (as shown in Fig. 4g and h) [33].

The local structure and redox behavior of active sites are important for the study of reaction mechanism, which can be investigated by extended X-ray absorption fine structure (EXAFS) and X-ray absorption near edge structure (XANES). For instance, Mn, Fe and Ni in NFMO-P2/O3 cathode materials at diverse charge/discharge voltage states were studied (Fig. 5). The XANES and EXAFS results showed that Mn^{4+}, $Ni^{2+/4+}$ and Fe^{3+} occurred in the initial cathode. Ni^{2+} was oxidized to Ni^{4+} during the charging process and the core edge and white line peaks finally coincided with the pristine at discharge states indicating the formation of $Ni^{2+/4+}$ (Fig. 5a–c). Meanwhile, Fe^{3+} and Fe^{4+} inter-transformed during the process of discharge/charge process. In addition, the Fe K-edge removed into higher energy region in charged to 4.5 V indicating the P2-OP4 transition and Na removal from the Fe face-shared active sites [33].

The phase transition and structural evolution are also studied by crystal orbital Hamilton populations (COHP) and DFT. As shown in Fig. 6a and b, the impact of Li substitution on the strength of TM–O bond was revealed by COPH analysis. The Li-doping helped to decrease the coordination numbers of the O atom, which was compensated by other enhanced TM–O bonds in NLNMF cathode especially for Ni–O bond. As shown in Fig. 6b, the orbital overlap between O atom and Ni atom was increased by 10%, which led to abstraction of e_g orbital degeneracy and inhibition of Ni^{3+} J–T effect. In addition, the impact of Li doping on solvent intercalation was also further revealed by DFT. As shown in Fig. 6c, the charge-density analysis showed that the Li–O chemical bond in NLNMF had a COPH value of 0.395 indicating a greatly ionic level. The lithium ions from the TM layer were easily attacked by the O atoms with the unbonded 2p electrons from the PC and EC molecules or the fluoride ions from the decomposition of FEC. As shown in Fig. 6d, the construction of TM fluorides from route I and route II were both forbidden owing to the scavenging influence of Li^+ ions, which resulted in a stable electrolyte-cathode interphase [24].

2.2 Polyanionic Compounds

Polyanionic compounds mainly including phosphates, pyrophosphates, fluorosulfates and sulfates are widely studied as cathode for SIBs [34–39]. Polyanionic compounds are generally in the form of $Na_xM_y[(XO_m)^{n-}]_z$. M represents metal ions with adjustable valence states, and X represents P, S, Si, V, etc. The X polyhedrons and the M polyhedrons are connected through co-edges or co-points to form the polyhedrons of the polyanionic compounds. Na^+ ions are

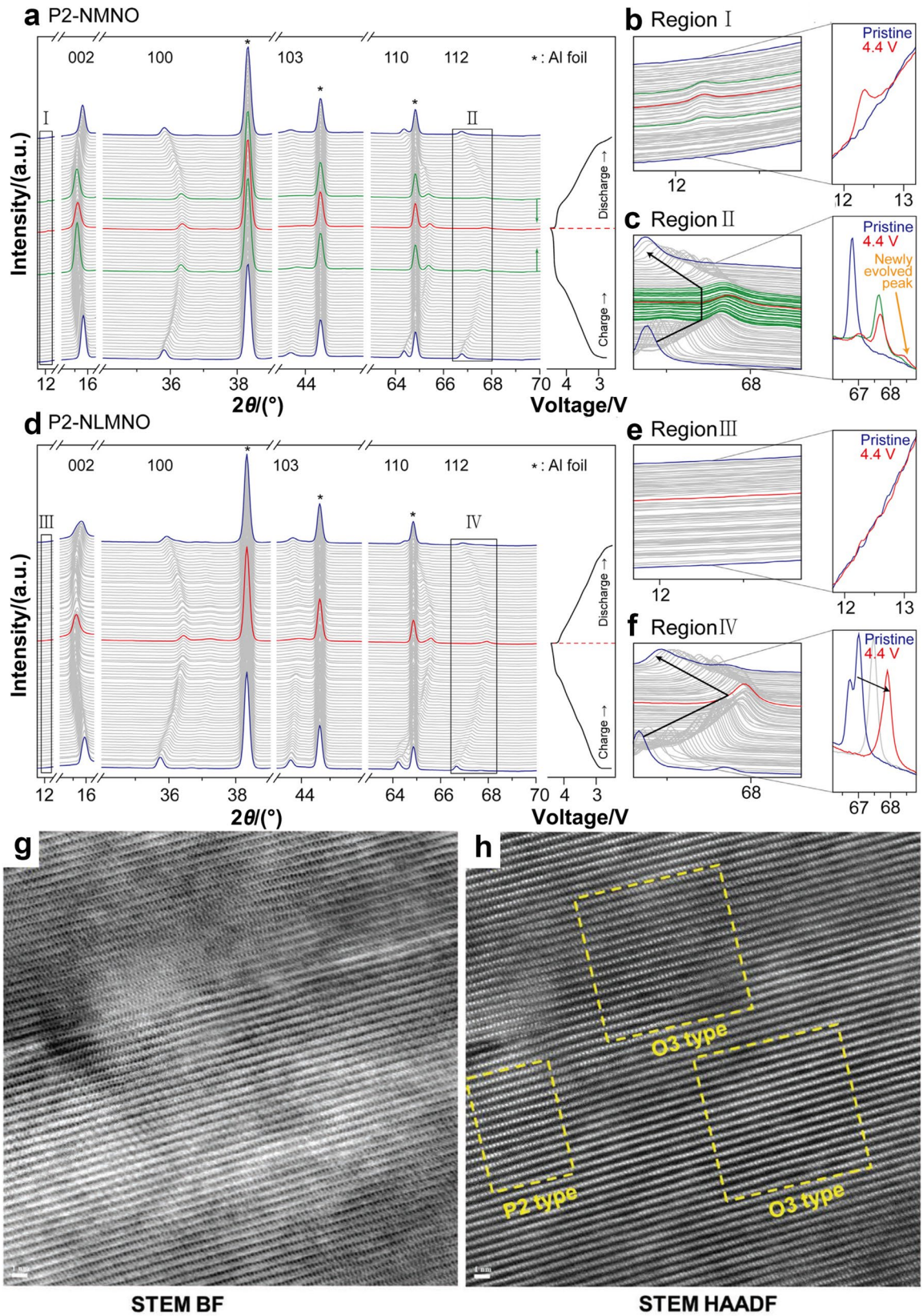
a P2-NMNO
002
100
103
110
112
*: Al foil
I
II
Intensity/(a.u.)
2θ/(°)
Discharge →
Charge →
Voltage/V
b Region I
Pristine
4.4 V
c Region II
Pristine
4.4 V
Newly evolved peak
d P2-NLMNO
III
IV
e RegionIII
f RegionIV
g
h
O3 type
P2 type
O3 type
STEM BF
STEM HAADF

◂**Fig. 4** In situ XRD patterns at different voltages of **a** P2-NMNO and **d** P2-NLMNO as cathodes for SIBs. Magnified XRD pictures of (**b, c**) P2-NMNO cathode material and **e**, **f** P2-NLMNO cathode material of the designated areas. Adapted with permission from Ref. [26]. Copyright©2021, Elsevier. **g**, **h** STEM images of NFMO P2/O3 cathode material of 100 cycles. Adapted with permission from Ref. [33]. Copyright©2022, Wiley–VCH

dispersed between the gaps in the system. Polyanionic compounds show high cycling performance and high safety as cathode due to their high thermodynamic stability. However, polyanionic compounds have low electronic conductivity and low volume energy density. The low electronic conductivity is not conducive to the rate performance and fast-charging capacity. There is an increasing demand for fast-charging SIBs, which are largely influenced by the transport of ions and electrons in the electrodes, and the stability of electrodes. Ionic substitution or doping, coating, stoichiometric number variation in Na, size and morphology design can optimize these problems. In addition, some X polyhedrons can trigger the electrochemical activity of metals with variable valance states to increase the charge/discharge voltage.

2.2.1 Design Strategies and Synthesis Method

The polyanionic compounds usually have low electronic conductivity and low volume energy density, which will further influence the rate performance and fast-charging capacity. Design strategies of ionic substitution or doping, coating, stoichiometric number variation in Na, size and morphology design are adopted to optimize these problems. The kinds of metal, the reaction time and temperature, and the heating rates of calcination are adjusted to optimize the structure, morphology and crystalline. For the polyanionic compounds, the synthesis methods mainly include the sol-gel method [40], hydrothermal and solvothermal method [41, 42] combined with calcination under the inert atmosphere. For the sol-gel synthetic technique, citric acid also acts as the carbon source. For example, Ma and Huang et al. adopted the sol-gel method to obtain Na-deficient $Na_{3.41}£_{0.59}FeV(PO_4)_3$. The cathode material shows fast Na intercalation kinetics and fast-charging capacity [43].

2.2.2 Active Sites and Surrounding Environments of Active Sites

Phosphate compound cathode materials mainly include olivine type, sodium super ionic conductor (NASICON), pyrophosphate, mixed phosphates, etc. $NaFePO_4$ was early reported as cathode for SIBs. $NaFePO_4$ has maricite and olivine crystal type, while the maricite crystal type has inferior electrochemical activity [9]. In recent years, amorphous phosphate also has been verified to be an excellent cathode owing to its great theoretical specific capacity and good electrochemical reversibility. To further improve the performance of amorphous phosphate, Zhou and team members cleverly designed a yolk-shell structured amorphous $FePO_4$ cathode. The amorphous yolk-shell cathode showed a long cyclic stability, possessing a high capacity retention rate of 91.3% over 1 000 cycles [44]. In addition, the environments of active sites (specific surface area, morphology and structure, carbon coating, and atom doping, etc.) have a great impact on the reactivity of active sites.

NASICON has a three dimensional (3D) frame structure, which is formed by XO_4 tetrahedrons and MO_6 octahedrons (as shown in Fig. 7a) [45]. Na^+ ions of NASICON with fast mobility are located in the gap formed by the frame. However, not all of the Na^+ ions can provide reversible capacity. Take $Na_3V_2(PO_4)_3$ as an example, Na atom is located at two different sites, Na1 is located at the six-coordination M1 site, while Na2 is located at the eight-coordination M2 site. The Na^+ ions located at M2 can reversibly de-intercalate and intercalate with electrochemical activity, while Na1 at M1 site de-intercalate difficultly due to the small room. The possible diffusion paths based on the first principles calculations are presented in Fig. 7b–d. The possible migration diffusion paths for Na^+ ion are b path (along the *x* direction), c path (along the *y* direction), and d path (along the *z* direction and the voids/channels between the neighboring VO_6 octahedron and PO_4 tetrahedron). Except for d path (along the *z* direction), the transfer energies of b, c and d (bypass the octahedron) are small enough to realize the migration [45]. The results illustrate that the NASCION cathode material has a 3D open framework for fast ionic transport. However, the NASICON cathode has low electronic conductivity. In 2017, Zhang's group reported upgraded reversibility of Fe^{3+}/Fe^{4+} redox active sites in $Na_3Fe_2(PO_4)_3$ by carbon coating. The carbon layers could distribute microscopic stresses, enhance the shear strength of the cathode material to avoid the crack construction, and further avoid the degradation and agglomeration of these active particles. The improved carbon coated $Na_3Fe_2(PO_4)_3$ displayed a discharge capacity of about 109 mAh g^{-1} and superb cyclic performance (> 96% capacity retention exceeded 200 cycles [46]. For most phosphate cathode materials, the energy density is < 500 Wh kg^{-1} because of the limited number of electrons (one or two per formula unit) involved in the electrochemical reaction. In 2020, Chen's group developed an NASICON-type $Na_4MnCr(PO_4)_3$ cathode material that involved a three-electron reaction process for SIBs. The active sites were Cr^{3+}/Cr^{4+} (4.4 V), Mn^{3+}/Mn^{4+} (4.2 V) and Mn^{2+}/Mn^{3+} (3.6 V) active sites. The synergetic effect of Cr ions and Mn ions could make the structure stable and increase the working voltage to increase the specific capacity. The high-potential Cr active center could relieve the Mn^{3+} Jahn–Teller effect. The $Na_4MnCr(PO_4)_3$ cathode showed a super high energy density of 566.5 Wh kg^{-1} [47].

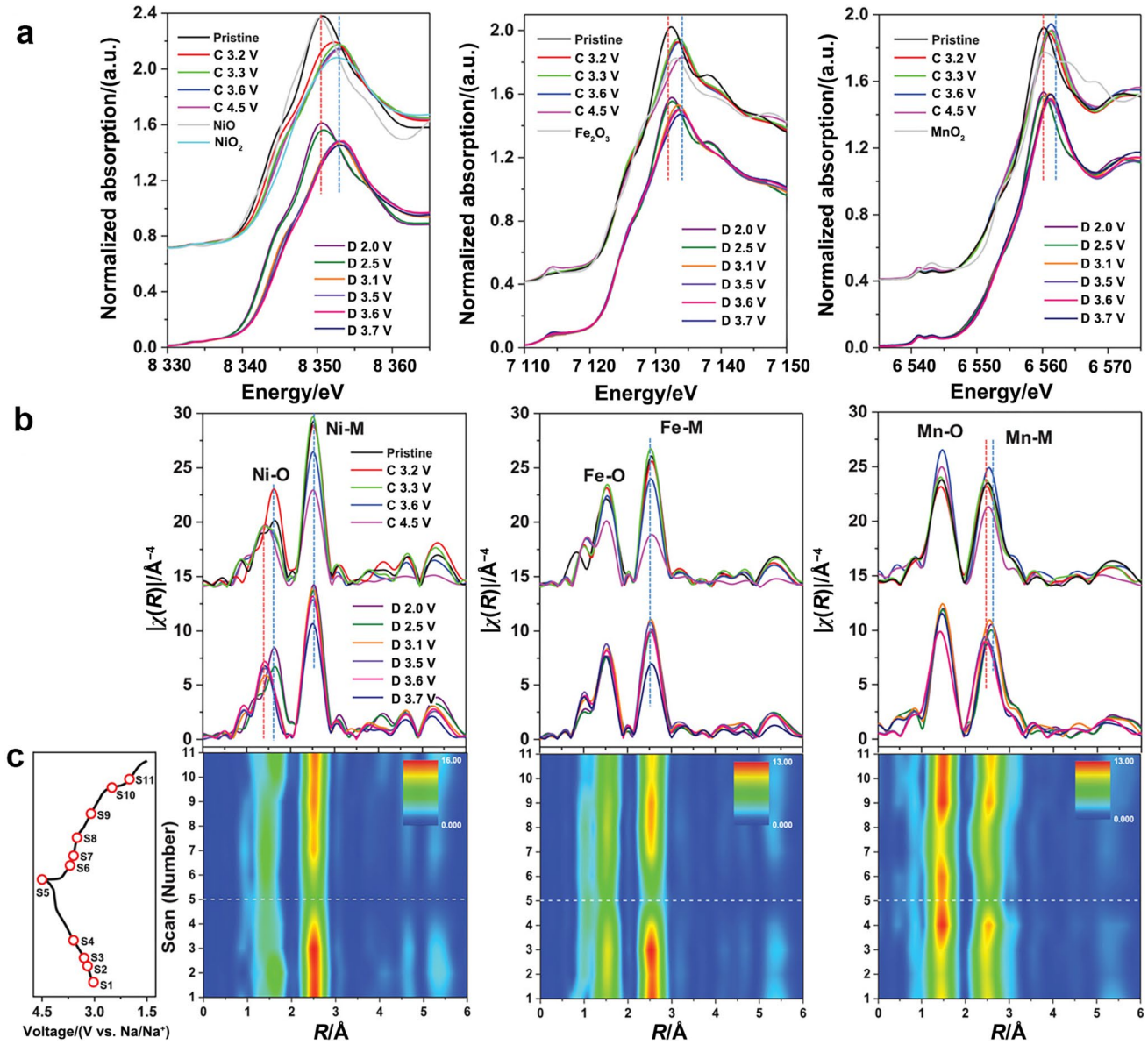

Fig. 5 **a** Ex situ XANES and **b** EXAFS curves, and **c** 2D contour pictures of Mn, Fe, Ni elements and corresponding voltage curve of NFMO-P2/O3 cathode material. Adapted with permission from Ref. [33]. Copyright©2022, Wiley–VCH

In recent years, many studies in the literatures have demonstrated that ionic doping and substitution are functional strategies to enhance the electronic conductivity and trigger multi-electron reaction, such as K, Ca, Mn, Ni, Cu, Al, Cr, La, Fe, Mg, etc. The doping contents have great effects on the electrochemical performance. In 2021, Igor V. Zatovsky and co-workers constructed a sequence of Co- and Cu-doped $Na_{3+x}V_{2-x}M^{II}x\ (PO_4)_3$/C ($x = 0.01, 0.03, 0.05$) cathode materials. The doped Cu and Co replaced the V sites. The doped Cu and Co made the sample have porous structure, which could expose more active sites of electrode materials to electrolyte. The electrochemical performance was adjusted by changing the doping contents of Cu and Co. The results showed that low doping contents could increase the electronic conductivity to enhance the capacity and cycling stability. The enhanced electrochemical performance could be due to the porous structure. And the doped metal might have reactive activity to improve capacity [40]. In 2022, Lai and co-workers adopted a Cr-doped strategy to active a three-electron transfer reaction (V^{5+}/V^{4+}, V^{4+}/V^{3+}, V^{3+}/V^{2+} redox sites) in $Na_3Cr_{0.5}V_{1.5}(PO_4)_3$ NASICON cathode material. The valence bands of the $Na_3Cr_{0.5}V_{1.5}(PO_4)_3$ cathode material were made up of the hybridized Na 3s, O 2p, P 2p V 3d and Cr 3d orbitals. Since Cr has one more valence electron than V, the forbidden-band gap could be reduced, while the high-potential V^{5+}/V^{4+} could be activated as active sites.

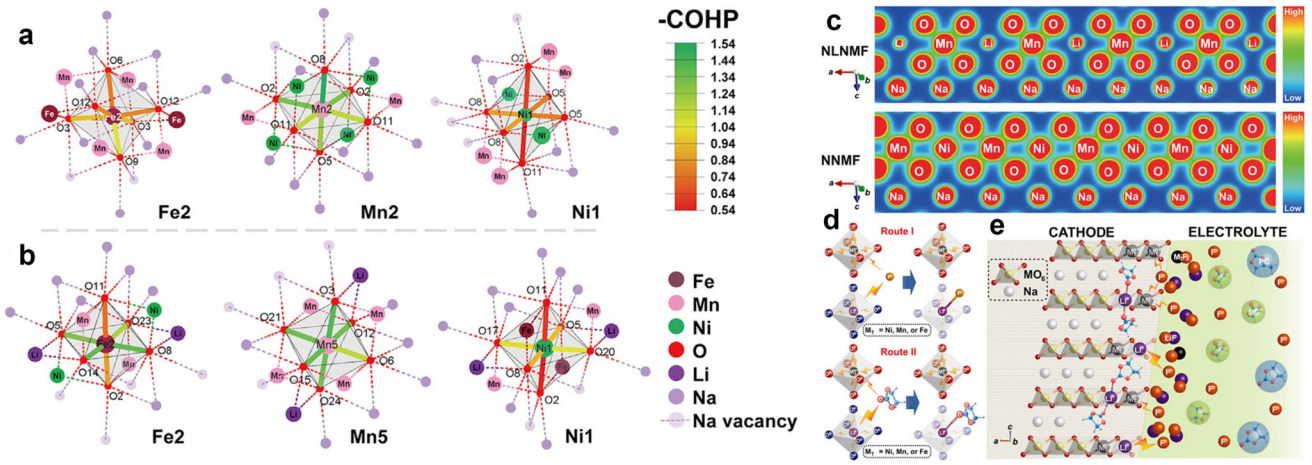

Fig. 6 Mechanism of the structural evolution studied by COHP analysis: **a** NNMF and **b** NLNMF. Mechanism of the chemical evolution at the cathode/electrolyte interphase: **c** DFT charge density schemes for the NNMF and NLNMF cathodes, **d** the reactions route between F^- anions and TM cations and **e** the generation of TM fluorides. Adapted with permission from Ref. [24]. Copyright©2018, Royal Society of Chemistry

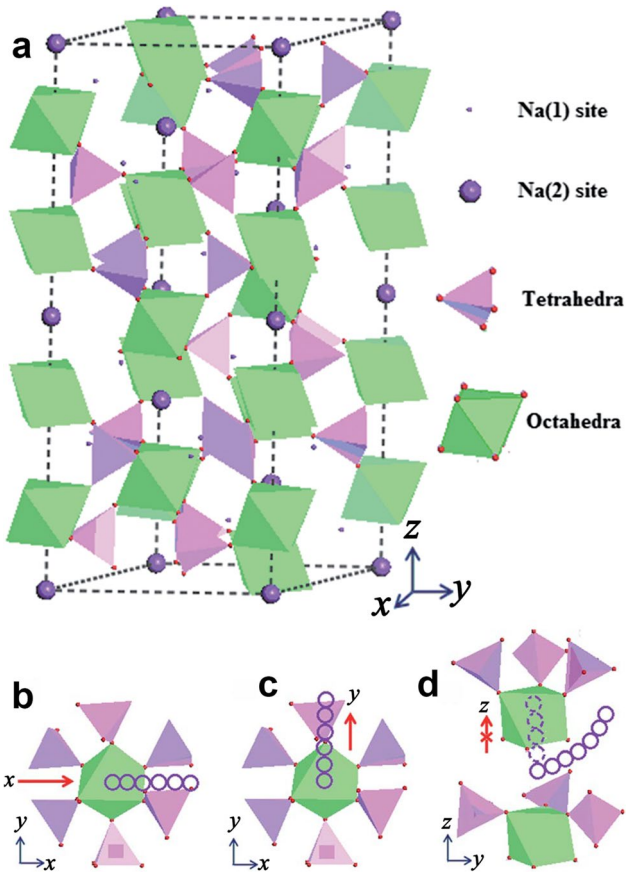

Fig. 7 **a** Schematic graphic of the $Na_3V_2(PO_4)_3$ cathode structure. **b–d** Possible migration paths of Na^+ ion in $Na_3V_2(PO_4)_3$ along different directions. Adapted with permission from Ref. [45]. Copyright©2014, Royal Society of Chemistry

As a result, the designed cathode material showed a reversible capacity of 176 mAh g^{-1} with a high energy density of 470 Wh kg^{-1} at 0.2 C, a fine rate capability, an outstanding cyclic stability reaching up to 1 000 cycles at 20 C and excellent fast-charging performance (≈11 min to reach 80% state of charge) [37]. Developing high mean working voltage NASCION is meaningful and is beneficial to increase energy density. In 2022, Wu's group first introduced a high-entropy to design NASCION cathodes. $Na_3V_{1.9}$(Ca, Mg, Al, Cr, Mn)$_{0.1}(PO_4)_2F_3$ fluorophosphate cathode material was synthesized without changing the V active center and showed an improved electrochemical performance with an extraordinary energy density (445 Wh kg^{-1}), a high average working voltage (3.8 V), and an inspiring structural stability with capacity retention rate of 80.4% over 2 000 cycles at 20 C. The enhanced Na storage performance was because that the high-entropy effect could increase electronic conductivity, thus decreasing the diffused energy barrier of Na^+ ions to accelerate the migration rate of Na^+ ions. Additionally, the high-entropy effect was beneficial to enhance the Na(2) sites occupation, inhibit the phase change even though in a low-voltage area, and improve mean voltage [48].

Pyrophosphate [$Na_xM_y(P_2O_7)_n$] belongs to the triclinic system and $p\bar{1}$ space group. The MO_6 octahedron and PO_4 tetrahedron generate the diffusion channel of sodium ion in the direction of [011] through the co-vertex oxygen atoms, thus showing the electrochemical activity of sodium storage. M_2O_{11} dimer also occurs in the pyrophosphate formed by P_2O_7 through co-angle or co-edge. Pyrophosphate has an open framework for Na^+ ions migration, stable structure and high working voltage. However, the poor electronic conductivity limits its further development. Many studies demonstrated that nanocrystallization, carbon

coating and structural design were effective to enhance and improve the electrochemical performance of the pyrophosphate cathodes. Most pyrophosphate cathodes are coated carbon layer along with structural optimization. In 2018, Lai and co-workers reported triclinic off-stoichiometric $Na_{3.12}Mn_{2.44}(P_2O_7)_2$/C cathode materials with a high energy density. Due to the strong electronegativity of the $(P_2O_7)^{4-}$, P–O covalent bonds could drive the electron from the Mn center, which weaken the Mn–O bonds. Thus, the Mn^{3+}/Mn^{2+} redox site to possess the high voltage platforms above 3.6 V [49]. In 2018, Deng et al. designed "bubble-in-nanorod" hierarchical hybrid fiber pyrophosphate-based freestanding cathodes. The $Fe^{2+/3+}$ was active couple. The special structure was beneficial to the contact of active sites and electrolyte. The freestanding cathodes had high ratio of active materials, which could improve energy density. Carbon coated pyrophosphate nanoscale crystals hollow sphere bubbles were homogeneously dispersed in the 1D porous carbon fiber, so the cathode had two carbon layers. The obtained hierarchical structure "bubble-in-nanorod" could not only offer a bi-continuous conductive network to speed up electron transport fast to active sites, but also avoid the structure deterioration to keep integrity. In addition, the carbon layer could protect the surface of cathode from reacting with O_2 and CO_2 in air. The "bubble-in-nanorod" hierarchical hybrid fiber pyrophosphate-based cathodes showed enhanced rate performance and specific capacity [34]. Similarly, Xu's group used a sponge-like 3D porous carbon coated Na-rich Fe pyrophosphate for long-life and high-rate cathode material [50], Li and co-workers reported carbon covered $Na_{3.64}Fe_{2.18}(P_2O_7)_2$ nanoparticles with a long life for SIBs [51].

Compared with phosphate cathode materials, sulfate cathode materials are wide resource and low cost. In addition, sulfate cathode materials have tunable structure, high voltage, stable skeletons and high electronegativity. Among these sulfate cathode materials, Fe-based sulfate materials are mostly studied because of high voltage, low cost and wide resources. Fe^{2+} is easily oxidized to Fe^{3+} resulting in low electrochemical activity. In order to inhibit the oxidation of the Fe^{2+} ions, Gao and co-workers implanted carbon nanotubes (CNTs) into $Na_6Fe_5(SO_4)_8$ particles. The CNTs and $Na_6Fe_5(SO_4)_8$ were bridged through $[SO_4]_2$…CNTs conjunctions. Meanwhile, the CNTs enhanced the conductivity and structural stability. As a result, the (CNTs)/$Na_6Fe_5(SO_4)_8$ cathode exhibited a high voltage of 3.7 V versus Na^+/Na [52]. Low conductivity also limits the advance of sulfate cathode materials. Conductive carbon materials (CNTs, rGo, etc.) are mostly used to improve the electronic conductivity of cathodes. In 2020, Chen and team members reported a hierarchical and high-voltage $Na_2Fe(SO_4)_2$@rGO/C cathode material with an enhanced energy density for SIBs. The rGO sheets urged the evenly electrostatic self-assembly process among carbon matrix and active materials. The cross-linked carbon network largely boosted the electron transfer and reaction kinetics, and inhibited an aggregation of active sites. The special $Na_2Fe(SO_4)_2$@rGO/C cathode material showed a superb sodium storage performance with an extraordinary voltage plateau (3.75 V), energy density (330 Wh kg^{-1}) and specific capacity (85 mAh g^{-1}) at 0.005 C [53].

2.2.3 Reaction Mechanism

Similarly, there are also structural evolutions for polyanionic compounds during charge/discharge process, which are usually disclosed by in situ XRD. Based on Fig. 8a and b, all peaks agreed with a rhombohedral phase ($R\bar{3}c$ space group) at the initial stage. All of the signals gradually shifted into the higher angles during charging process suggesting a solid-solution reaction, except the $(2\bar{1}6)$ peak disappeared indicating a biphasic reaction. During the discharge process, the $(2\bar{1}6)$ peak went back again, while all peaks removed to lower angles suggesting a mixture of reversible solid-solution and biphasic reaction mechanism. In addition, the lattice parameters with different charge/discharge states were collected (Fig. 8c) in order to further illustrate the structure evolution. The volume changes of the $Na_3Cr_{0.5}V_{1.5}(PO_4)_3$ cathode was only 7.79%, suggesting the well stability. Based on the results of Fig. 8a–c, the structural developments of the $Na_3Cr_{0.5}V_{1.5}(PO_4)_3$ cathode are illustrated in Fig. 8d. The cathode underwent the reaction mechanism of $Na_3Cr_{0.5}V_{1.5}(PO_4)_3 \leftrightarrow Na_1Cr_{0.5}V_{1.5}(PO_4)_3 \leftrightarrow Na_4Cr_{0.5}V_{1.5}(PO_4)_3$ through extraction/insertion of Na^+ ions [37].

To further confirm the reaction mechanism and active sites, the galvanostatic charge and discharge profiles, and synchrotron radiation technique are used. The galvanostatic charge and discharge curves of NMCP/C cathode material in the voltage window of 1.4–4.6 V versus Na^+/Na showed that three distinct voltage plateaus occurred at 3.6 V, 4.2 V, and 4.4 V, which corresponded to Mn^{2+}/Mn^{3+}, Mn^{3+}/Mn^{4+}, and Cr^{3+}/Cr^{4+} redox sites, respectively (as shown in Fig. 9a). The results were further verified by XANES and EXAFS (Fig. 9b–d). As shown in Fig. 9b, the energy of K-edge shifted to a higher energy area at charged state of 3.8 V and further moved to the higher energy area at charged state of 4.3 V, which corresponded to the oxidation from Mn^{2+} to Mn^{3+}, Mn^{3+} to Mn^{4+}, respectively. Figure 9c shows that the pre-edge signal split into double signals situated at 5 990 eV and 5 992 eV charged to 4.3 V, and the peak at 5 992 eV increased further charged to 4.6 V, which suggested the Cr^{3+} was oxidized to Cr^{4+}. All peaks came back to their initial states discharged to 1.4 V, which indicated a reversible three electrons reaction,

$Na_4Mn(II)Cr(III)(PO_4)_3–3Na^+–3e^- \leftrightarrow NaMn(IV)Cr(IV)(PO_4)_3$. To further study the structural evolution and mechanism reaction, the in situ XRD (shown in Fig. 9e) was conducted. There were some peaks reversible shifts suggesting a solid-state reaction. The (211) peak shifted to higher angles and disappeared, and the (300) peak split to two peaks upon charge. The changes of these peaks returned to initial locations, which suggested that the cathode underwent a reversible phase transition [47].

For the polyanionic compounds, the electronic conductivity is usually low. In order to study the electronic conductivity and propose an optimized strategy, the DFT calculation including density of states (DOS) is used. Figure 10a–f shows the transfer path of Na from Na(2) sites to Na(1) sites in HE-NVPF and p-NVPF, where IS represented the initial state, TS was the transition state and FS was the final state. The calculated migration energy barriers according to the technique of climbing-image nudged elastic band (CI-NEB) were 0.963 and 1.984 eV for HE-NVPF and p-NVPF, respectively. The results indicated that the Na^+ ions in HE-NVPF were easier diffusion than p-NVPF. The energy of FS was 0.537 0 and 1.675 0 eV for HE-NVPF and p-NVPF, respectively, which suggested that Na^+ ions in HE-NVPF were easier to escape from Na site than p-NVPF. The low FS energy helped to inhibit the phase transition and rearrangement of the Na site. From Fig. 10h, the bandgaps of HE-NVPF and p-NVPF were 0.71 and 1.68 eV, respectively. The lower bandgap of HE-NVPF indicated the better electronic conductivity [48].

2.3 PBAs and Organic Compounds

In recent years, PBAs and organic compounds as cathodes for SIBs have gained more and more attention. The PBAs have a large tunnel structure and the structure is stable in the charge/discharge course; but the tap density of the PBAs is low, the crystallization water in the PBAs is difficult to remove, and there are safety hazards in heating conditions for the PBAs. The organic compounds possess high theoretical capacity, abundant raw materials,

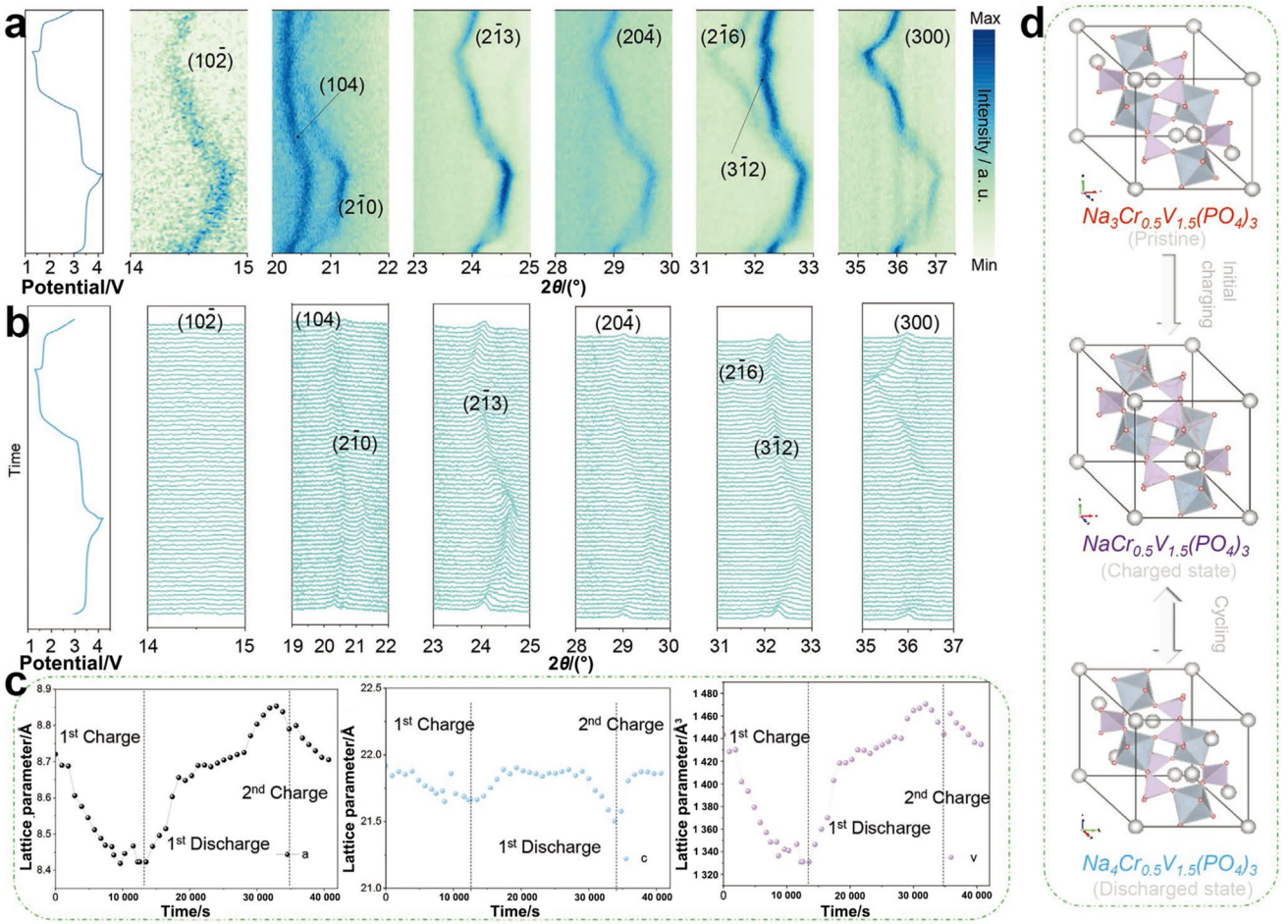

Fig. 8 **a** In situ XRD contour mapping. **b** Stacked line plots. **c** Variation in the lattice parameters. **d** Schematic graphic of the crystal structure at different charged/discharged states of $Na_3Cr_{0.5}V_{1.5}(PO_4)_3$. Adapted with permission from Ref. [37]. Copyright©2022, Wiley–VCH

environmental friendliness, low price and flexible structure design; however, the organic compounds have low electronic conductivity and easy dissolution in organic electrolytes.

2.3.1 Design Strategies and Synthesis Method

The PBAs often have crystal defects and interstitial water. So, many design strategies are adopted, such as regulating reaction temperature and time to synthesize specific crystalline products and adding surfactants to modulate the special structure. In addition, to improve the structural stability and electronic conductivity, in situ synthesis or later addition of conductive materials is adopted. The raw materials to synthesize PBAs are corresponding metal salts and $Na_4Fe(CN)_6{\cdot}10H_2O$. The ball milling solid-state method [54], solvothermal method [55] and facile stirring at different temperature [56] are used to synthesize PBAs. The obtained PBAs require no further calcination with high temperature, due to their low thermal stability. If there needs to enhance crystalline and remove impurities, low calcination temperature (below temperature of pyrolysis) is used [54].

The synthesis and modification methods are similar for organic compounds cathode and anode materials. For example, Wang and co-workers reported a carbomethoxy-modified disodium organic material, which shows stable fast-charging performance [57]. Some organic compounds are synthesized by reflux at different heating temperatures. The organic compounds have the low conductivity and easy solubility in organic electrolytes. The ALD is used to coat thin film on the surface of the organic compounds to avoid the dissolution in the electrolytes [58]. The CNT and rGO are mixed with the organic compounds through ultrasound, stirring, hydrothermal and solvothermal methods [59–62]. Sometimes, subsequent calcination is adopted to strengthen the combination between the organic compounds and CNTs or rGO.

2.3.2 Active Sites and Surrounding Environments of Active Sites

PBAs are commonly face-centered cubic structure in the form of $A_xM_A[M_B(CN)_6]{\cdot}zH_2O$ (A is the alkali metal ions and M is the transition metal ions). The alkali metal ions are located in coordination pores and 3D channels. The large 3D multi-channels provide big room for the insertion/extraction of Na^+ ions. The PBAs possess high voltage, high reversible capacity and low cost. So, the PBAs have a great potential application prospect in SIBs [63]. However, the PBAs often have crystal defects and interstitial water, resulting in the low cycling stability. In addition, the

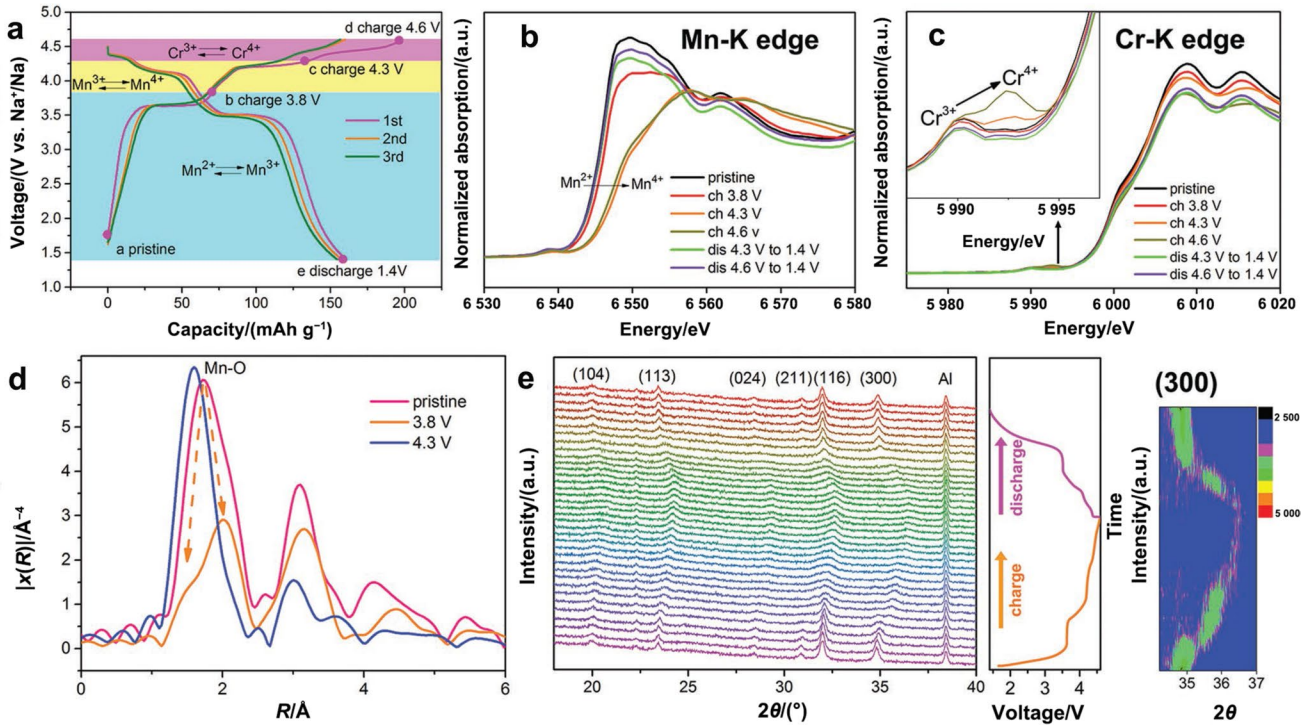

Fig. 9 **a** Galvanostatic charge–discharge profiles. XANES curves of **b** Mn K-edge and **c** Cr K-edge measured at different charge/discharge states. **d** Corresponding Fourier-transformed Mn K-edge EXAFS spectra of the charge process. **e** In situ XRD patterns of the 1st cycle of the NMCP/C electrode. Adapted with permission from Ref. [47]. Copyrigh©2020,Wiley–VCH

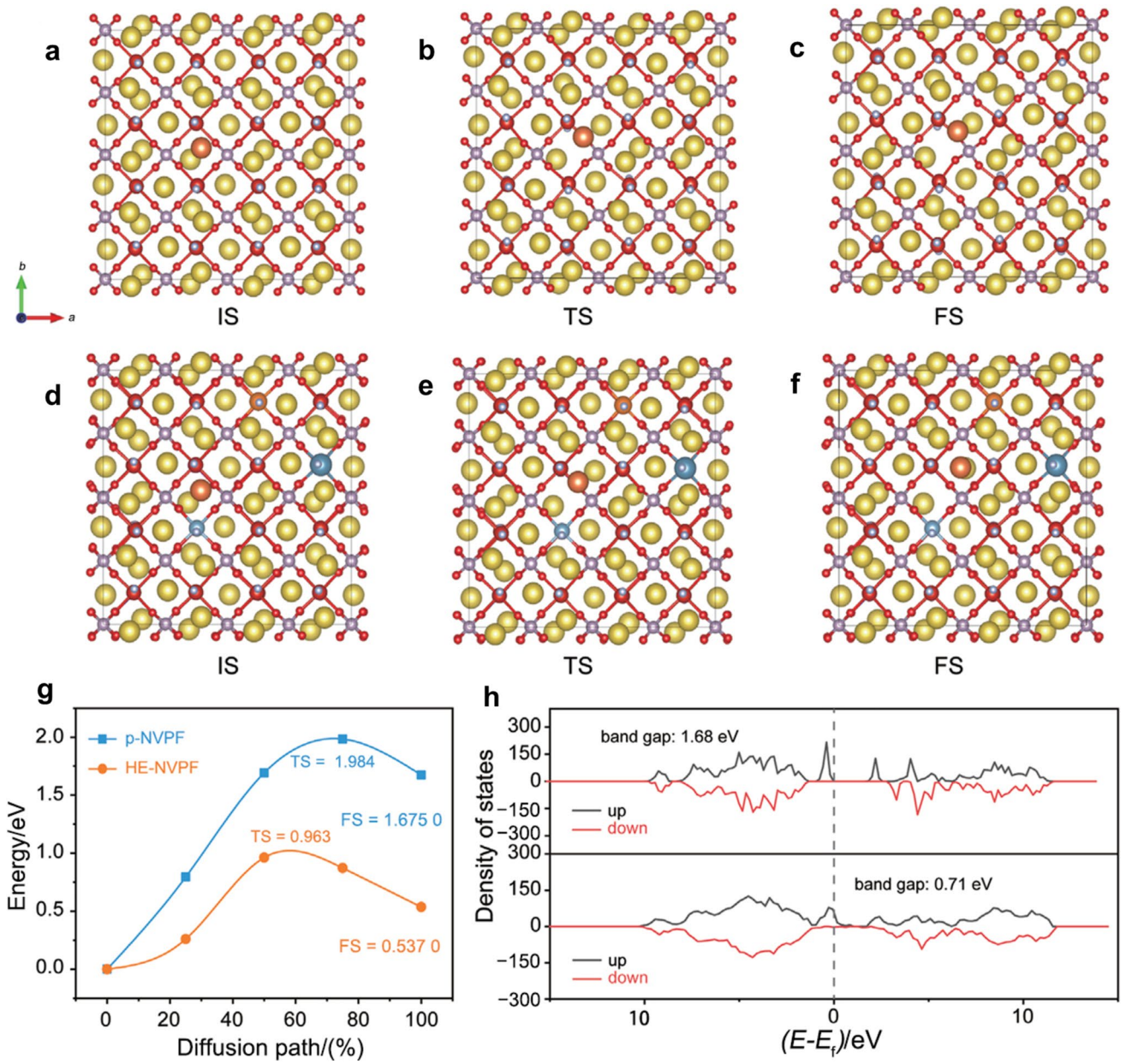

Fig. 10 Na^+ ion transfer pathways in p-NVPF (**a**–**c**) and HE-NVPF (**d**–**f**). **g** The corresponding migration energy and **h** DOS of HE-NVPF (down) and p-NVPF (top). Adapted with permission from Ref. [48]. Copyright©2022, Wiley–VCH

PBAs are easy to decompose at high temperature, leading to safety risks. In 2020, Jiang and co-workers adjusted the crystal type to regulate the electrochemical stability. They obtained cubic and monoclinic structured $Na_xMnFe(CN)_6$ cathode materials, and the active sites were Mn and Fe sites. The monoclinic $Na_xMnFe(CN)_6$ cathode occurred undesirable phase transition as a result of the Mn^{3+} Jahn–Teller effects, thus giving rise to low cycling stability. The cubic structure possessed high structural symmetry, which still maintained structural stability in the repeated charge/discharge course with a specific capacity of about 120 mAh g^{-1} and a capacity retention rate of 70% over 500 cycles at density of 200 mA g^{-1} [56]. The structural design and optimization are also operative ways for enhancing the robustness of framework. In 2020, Wan et al. designed a stepwise hollow cubic single-crystal PBA nanoframes and

carbon nanotubes composite as one kind of binder-free cathode material for SIBs. Among the framework, both of the N-linked Fe_1(6-coordination) and C-linked Fe_2(8 coordination) were redox active sites. The stepwise hollow cubic structure could increase the reactive sites, reduce the diffusion distance of ions and quicken the ion transport process. The reduced path of Na^+ ion diffusion, the excellent charge–discharge relaxation and optimized redox reactions of Fe atoms made the hybrid PBA nanoframes/CNTs film show outstanding electrochemical performances (about 92% capacity retention over 500 cycles at 5 C) [55]. In 2022, Chou's group adopted a ball milling way to synthesize highly crystallized PBAs $Na_{1.66}Mn[Fe(CN)_6]_{1.00}$ (MnHCF-S-170) as cathode materials for all-climate SIBs. They proposed a "water-in-salt" nanoreactor to obtain highly crystallized PBAs with low water contents and defects (suppressed $[Fe(CN)_6]$ vacancy), and high contents of Fe^{2+}. The PBAs cathode possessed Fe^{II}–C≡N–Mn^{II}/Fe^{III}–C≡N–Mn^{III} redox-active sites. The little $Fe(CN)_6$ vacancies in Fe^{II}–C≡N–Mn^{II} sites of the MnHCF-S-170 were beneficial to enhance the integrity of frame and provide smooth channels for Na-ion transport, thus possessing quick Na^+ ions and electrons migration kinetics to enhance the rate performance. In addition, the high content of Fe^{2+} active sites could offer high specific capacity. Consequently, the MnHCF-170 displayed the big specific capacity of 164 mAh g^{-1} at 10 mA g^{-1}, and a super all-climate electrochemical performance between 10 and 50 °C for SIBs [54].

Organic compounds cathodes mainly include quinones, anhydrides, amides, phenols and polymers. Organic compounds cathodes possess the merits of low price, abundant raw materials, environmental friendliness, high theoretical specific capacity and the flexible structure design. However, the low conductivity and solubility in organic electrolytes also limit their further development. In 2020, Lee's group coated ultrathin (Å-level) metal oxide on the perylene-3,4,9,10-tetracarboxylicacid dianhydride (PTCD) as a cathode for SIBs. The active sites were C=O. The coating layer could provide more channels for Na^+ ions diffusion and enhance the Na^+ ions diffusion into the active sites to improve the specific capacity and the kinetics of the redox reaction [58]. The polymerization of small organic molecules can also effectively solve the dissolution in organic electrolytes and improve the electrical conductivity. Zhang's group reported conjugated porous polyimide poly (2,6-diaminoanthraquinone) benzamide (CP-PDAB) with enhanced electronic conductivity and small volume expansion. The obtained CP-PDAB intriguingly combined redox active carbonyl groups of quinone compounds with anhydride/imide groups of dianhydride compounds to obtain an appropriate voltage. Moreover, the conjugated structure of CP-PDAB could increase electron delocalization, resulting in enhanced electronic conductivity. As a result, the active site C=O could react with Na^+ ion reversibly with the three-electron redox mechanism for the CP-PDAB cathode material in charge/discharge courses to show excellent cyclic performance and rate performance [61]. In addition, designing porous structure and adding conductive carbon are also all-right ways to prevent the organic compounds from the dissolution in organic electrolytes and enhance electronic conductivity [59].

2.3.3 Reaction Mechanism

For PBAs, there is a redox reaction of the active metal and reversible phase transition. The reaction mechanism can be proved by in situ Raman and XRD. As indicated in Fig. 11a–c, the Raman spectra showed three low peaks at 2 050, 2 078, and 2 090 cm^{-1} and two high peaks at 2 070, 2 110 cm^{-1} at the fully charged state, which were indexed to Fe^{III}–C≡N–Mn^{III} groups. During the insertion of Na^+ ions, the low peaks at 2 050, 2 078 and 2 090 cm^{-1} disappeared regularly, which suggested that the Mn^{3+}/Fe^{3+} were reduced to Mn^{2+}/Fe^{2+}. During the charging process, these peaks returned to their original states, which indicated that the Mn^{2+}/Fe^{2+} were oxidized to Mn^{3+}/Fe^{3+}. The in situ XRD (Fig. 11d, f) presented that double peaks were united into single peak at 25°, and a new peak appeared and became strong at 16.8° combined with the original peaks disappeared during the charging process, which suggested that the monoclinic phase transferred into the cubic phase. Interestingly, the XRD peak returned to the primary states in the subsequent discharging process, suggesting the reversibility of the MnHCF-S-170 cathode [54]. For multi-metal PBAs (medium- or high-entropy) cathodes, there are multiple active sites, and their electrochemical reaction mechanisms are more complex. However, not all metals in PBAs undergo electrochemical redox reaction as active sites. Chou and co-workers reported a disordered rubik's cube high-entropy PBAs with fast-charge and long cyclic performance. In situ XANES, PXRD and theoretical calculations (DFT) suggested that Cu, Co, Fe and Mn were active sites because of their DOS peaks near the Fermi level, while the Ni site was inert due to its DOS peak far away from the Fermi level. The role of Ni in the HE-HCF is to make the HE-HCF electrode have superb Na^+ ion diffusion kinetics. In addition, theoretical calculations showed that the high entropy materials had good thermal stability [64].

For organic compounds, the organic functional groups have redox reaction during the charge/discharge process. FTIR combined with DFT is usually used to illustrate the reaction mechanism for the organic cathode. For example, the FTIR of the CP-PDAB cathode presented that the stretching vibration of the C–N bond located at 1 359 cm^{-1} and the C=C bond signal of the anthraquinone ring located

at 1 590 cm^{-1} showed no change, which indicated that the C–N and C=C showed no reactive activity during charge/discharge process. The stretching vibration of the C=O bond located at 1 782 and 1 729 cm^{-1} gradually disappeared during the discharging process and became stronger and stronger during the charging process. In the meantime, new peaks located at 1 390 and 775 cm^{-1} aroused indexed to the stretching vibration of the C–O–Na bond, which was because of the creation of the SEI layer (Fig. 12b). The result of FTIR proved that the C=O bond took part in the redox reaction, which could contribute capacity. Based on the results of the FTIR, the electrochemical redox reaction process was proposed (as shown in Fig. 12c). The CP-PDAB cathode underwent three electrons transfer with two electrons for carbonyl and one electron for the AQ unit. The redox reaction was divided into three steps [61]. In addition to the C=O active site, the C=N in organic electrodes is also one type of active sites. Wang and coworkers reported a hexaazatriphenylene-based polymer as the electrode for alkali metal-ion batteries. The in situ FTIR and ex situ XPS indicated that the C=O and the C=N were both active sites [65]. N=N can also act as active sites to offer capacity. For example, N=N of azo compounds could react with Na^+ ion to form Na–N–N–Na during the sodiation process and regenerated N=N during the desodiation process [66].

The DFT was made to calculate the energy gap of the cathode materials. As shown in Fig. 12d, the $[CuDEPP]^{2+}$ and $[CuDEPP]^{2-}$ possessed low energy gap with 0.76 eV and 1.81 eV, respectively, which made them show highly reversible electrochemical reactions and reversibly transfer two positive charges and two negative charges during the charge/discharge process [67].

3 Anode Materials

Anode materials have been studied extensively as an essential part of SIBs. SIBs anode materials are generally classified into four types based on the reaction mechanism: (1) sodium metal anode materials based on sodium deposition; (2) insertion-type mechanisms; (3) alloy-type materials and (4) conversion-type materials.

3.1 Na Metal Anode Material

Sodium metal anode possesses high capacity and low redox potential. However, uneven sodium ion transfer in bulk sodium anodes can result in local deposition/dissolution of Na during high speed plating/stripping behavior and result in severe dendrite growth and accumulation. Compared to other types of anode materials, the research on Na metal anode materials is little.

3.1.1 Design Strategies and Synthesis Method

In view of the problems existing in sodium metal batteries (SMBs), most of researches synthesize and design metal anode materials from the perspective of sodiophilicity. It is also an effective solution to start with the electrolyte. For example, Wang et al. used a concentration effect of the electrolyte to design a diluted electrolyte for SMB low-temperature operation [68]. In the case of low concentration salt and tetrahydrofuran solvent, the interaction between solvent and sodium ions is low to realize fast reaction kinetics at low temperatures.

3.1.2 Reaction Mechanism

The Na anode has high reactivity and is prone to deposition. In order to characterize the key part of SEI in Na deposition behavior, XPS (Fig. 13) was performed on Na metal anodes with diverse electrolytes. According to the comparison of Fig. 13a and b, it could be seen that the induced SEI layers in these different electrolytes were measured to have a stronger Na-auger signal at − 20 °C, suggesting that the SEI layer was thinner at lower temperature. The SEI layer formed at 0.3-D/T (0.3 mol L^{-1} $NaPF_6$ in DEGDME/THF electrolyte) showed a lower NaF strength, but more oligomers and flexible alkyl carbonate esters. This suggested that free THF molecules resulted in more solvent-derived SEI layer. The enriched organic components in SEI layer provided adequate Na^+ ion transport, thus promoting low-temperature dynamics. The DFT study (Fig. 14a–d) of Liu et al. showed that the coexistence of N and O functional groups on the carbon matrix could give a strong sodiophilicity and could adjust the Na deposition behavior to plane extension. The uniform distribution and dendrite-free structure of Na^+ could be promoted by preparing strong 3D carbon nanofibers with N and O functional groups [69]. Zhao et al. designed a Na_3Bi hybrid anode with sodiophilicity, which had abundant ion diffusion channels. The low ion diffusion barrier and adsorption energy in Na_3Bi ensured uniform Na^+ ion nucleation and fast migration within the Na^+ mixed anode, resulting in uniform deposition and dissolution even at high current density [70]. Moreover, the bismuth compounds could achieve compact sodium deposition in the sodiophilic framework during the cycle, which was conducive to promote the sodium storage behavior.

3.2 Insertion-Type Materials

The insertion type usually has a small volume change and superior cycling stability during the charge/discharge

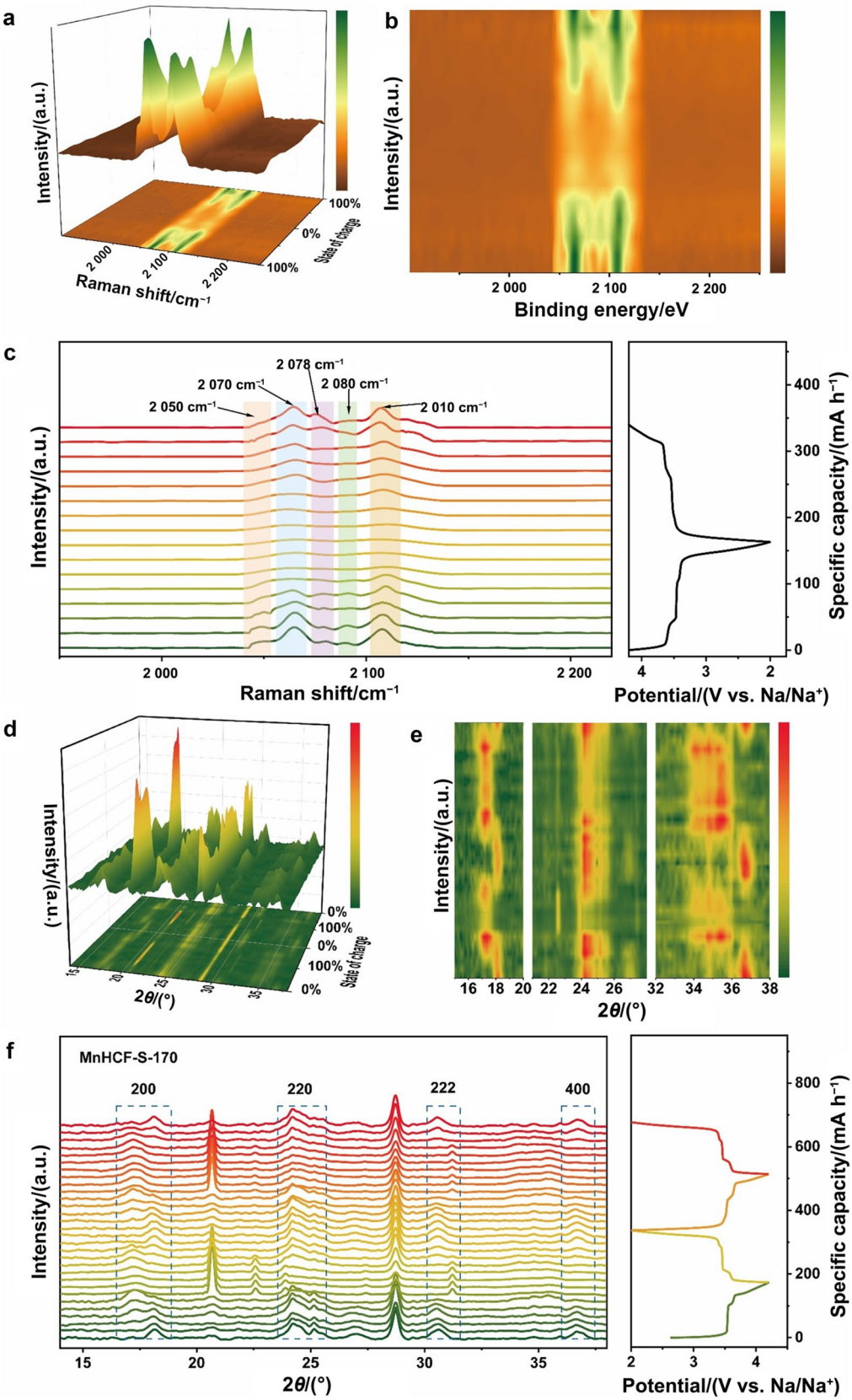

Fig. 11 **a** In situ Raman 3D color mapping. **b** 2D contour plot, and **c** stacked line spectra. **d** In situ PXRD 3D color mapping. **e** 2D contour plot, and **f** stacked line spectra of MnHCF-S-170. Adapted with permission from Ref. [54]. Copyright©2022, Wiley–VCH

process. Among the insertion-type anodes, the non-graphene-based carbon materials are deemed to the "first generation" choice of SIBs anode materials owing to their low price and abundant resources. Nevertheless, such materials have a low operating voltage, which will cause safety problems in practical applications. In addition, the carbon materials have a low charge/discharge specific capacity. Titanium oxides (TiO_2, $Ti_{0.94}Nb_{0.06}O_2$, $Li_4Ti_5O_{12}$, $Na_2Ti_3O_7$, etc.) have a suitable operating voltage, moderate price and non-toxicity, but they have poor electrical conductivity. Combining their strengths and weaknesses, a lot of excellent work has been reported.

3.2.1 Design Strategies and Synthesis Method

Micro-/nanostructure design, nanocomposite optimization, defect introduction and heteroatom doping can be used as valid methods to design carbon-based anode materials with electrochemical and structural stability, enhanced capacity and fast-charging capacity. Ni et al. reported an N,S-doped mesoporous hollow carbon sphere. S-doping enhanced the Na^+ ion transfer kinetics and N-doping improved the capacity, which made the anode show a fast-charging capacity [71]. Chen et al. prepared vanadium-modified submicron hard carbon materials with stable interface by hydrothermal carbonization and high temperature pyrolysis, whose pseudographitic structure played an important role in sodium storage and interface stability [72]. Yu et al. grew fully crystallized carbon in hard carbon precursors by calcination. At low temperature (380 °C), the graphite skeleton could effectively prompt the decomposed carbon atoms and atomic fragments to be ordered in a parallel manner, making them move in an orderly manner and convert sp^3 hybrid carbon into sp^2 hybrid carbon, thus helping to generate crystal structure. Subsequent high temperature calcination (1 300 °C) was adopted to increase crystal quality, resulting in the formation of fully crystallized carbon [73]. Compared to graphite, graphene with a 2D structure has a higher potential to create more active sites for ionic carriers. There are many synthesis methods of graphene, such as electrochemical synthesis, thermal reduction, liquid phase stripping and so on. Yu et al. successfully synthesized a sequence of N-rich low-layer graphene (N-FLG) with interlayer distances in the range of 0.45 nm and 0.51 nm by annealing g-C_3N_4 at 800 °C catalyzed by zinc. Pyrrole N increased the interlayer distances because of its stronger electrostatic repulsion [73]. Thus, the N-FLG-800 achieved optimal performance in terms of layer spacing, nitrogen configuration, and electronic conductivity.

The modification of titanium oxide is mainly through doping, usually heteroatomic doping (N, F, P, S). Tao et al. investigated the sodium storage behavior of titanium oxides with a low price for the first time. They prepared a sequence of titanium oxides (TiO and Ti_2O) through electric field control, and precisely adjusted their stoichiometric ratios through regulating the electrolytic time and voltage [74]. Meanwhile, the choice of composites with other materials is also a common method, such as CNT, GO, rGO and phosphide.

3.2.2 Active Sites and Surrounding Environments of Active Sites

Carbon material is rich in resources, low in cost, environmentally friendly, non-toxic and harmless, which can be a good candidate SIB anode material. According to the structure, it is consisted of soft carbon, hard carbon and nanocarbon materials. However, the capacity of carbon as an anode material for SIBs is lower than that of carbon as an anode for LIBs. Owing to the large radius of the Na^+ ion, it is difficult to insert/extract Na^+ from carbon materials. In addition, NaC_6 is also an intercalated compound, which is not conducive to energy conversion [75].

Hard carbon usually has good sodium storage capacity owing to its high structural disorder and large layer spacing. Nevertheless, its abundant surface defects and low electrical conductivity result in low first-loop Coulombic efficiency (CE) and inferior rate performance. To enhance the CE of the 1st circle of hard carbon, Chou et al. obtained biomass (hazelnut shell) by carbonizing the hazelnut shell with hydrochloric acid, which expanded the layer spacing and obtained more active sites [76]. The biomass hazelnut shell had a high reversible capacity of 342 mAh g^{-1} and a high CE of 91%. Wu et al. constructed a homotype heterojunction on hard carbon to induce a steady solid electrolyte interface, effectively increasing the 1st cycle CE of hard carbon from 64.7% to 81.1%. Utilizing a facile surface engineering strategy to coat homogeneous amorphous Al_2O_3 layer on hard carbon can also shield the active site (pores, defects and functional groups) on the surface to hinder the decomposition of electrolyte, so as to form a thin SEI layer, and reduce resistance. The optimized hard carbon showed an enhanced initial CE, a reversible capacity of 321.5 mAh g^{-1} at 50 mA g^{-1}, and a high capacity retention rate up to 86.9% over 2 000 cycles of 1 A g^{-1} [77].

Soft carbon has been less studied than hard carbon as an anode for SIBs. Soft carbon has high electrical conductivity, but its regular microcrystalline structure is not helpful for the storage of Na^+ ions [77]. The suitable precursors can be selected to optimize the sodium-storage properties of soft carbon by morphology control, heteroatom doping and pore structure construction. Wu et al. reported an N/P co-doped soft carbon nanoboxes (NPSC) prepared from petroleum asphalt. The introduction of N and P provided more active sites for Na^+ ion storage [78]. In addition, the nanoboxes structure of the material

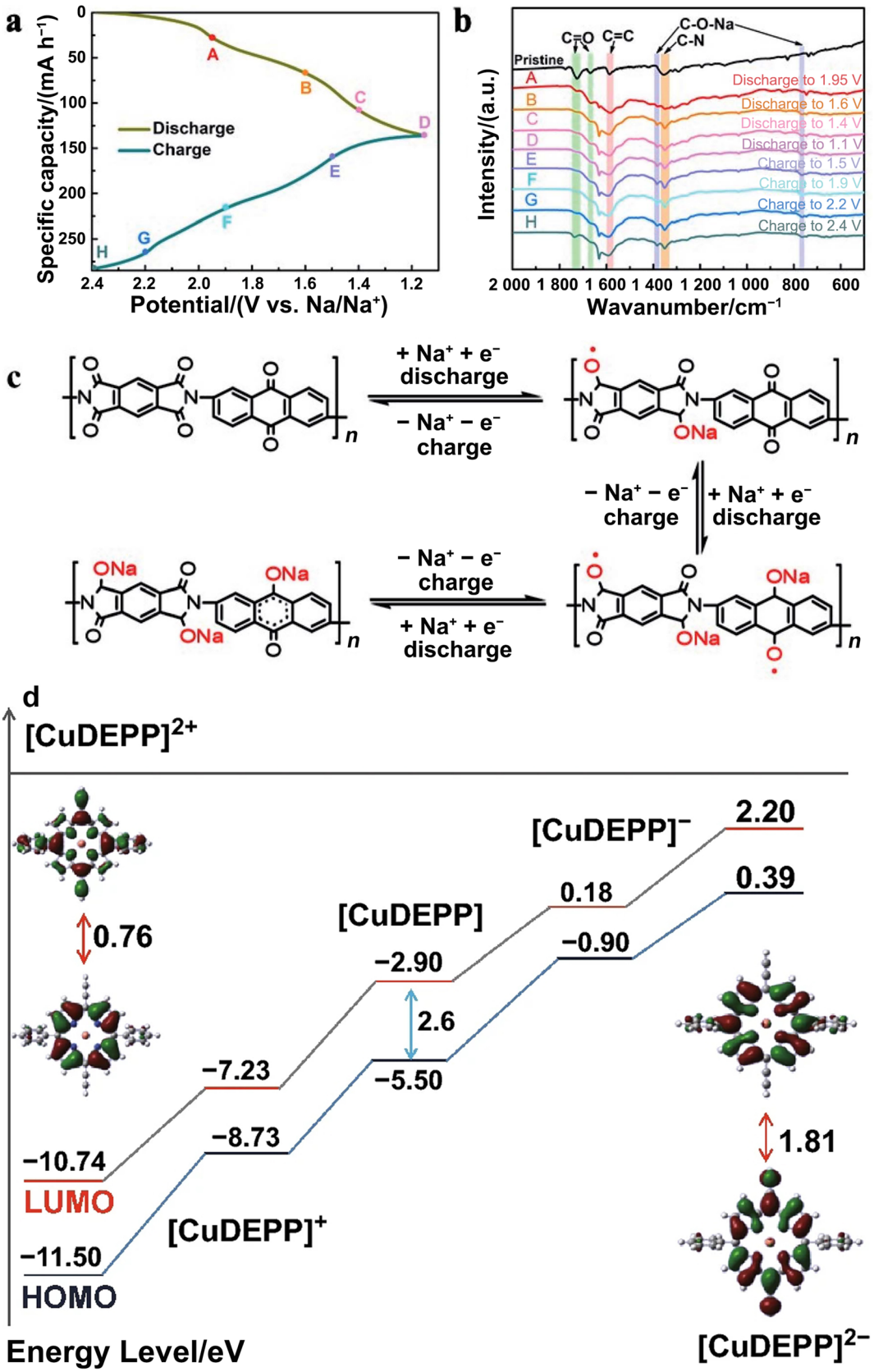
a
Specific capacity/(mA h⁻¹)
Potential/(V vs. Na/Na⁺)
Discharge
Charge
A
B
C
D
E
F
G
H
b
Intensity/(a.u.)
Wavanumber/cm⁻¹
C=O
C=C
C-O-Na
C-N
Pristine
Discharge to 1.95 V
Discharge to 1.6 V
Discharge to 1.4 V
Discharge to 1.1 V
Charge to 1.5 V
Charge to 1.9 V
Charge to 2.2 V
Charge to 2.4 V
c
+ Na⁺ + e⁻ discharge
− Na⁺ − e⁻ charge
ONa
d
[CuDEPP]²⁺
[CuDEPP]⁻
[CuDEPP]
[CuDEPP]⁺
[CuDEPP]²⁻
2.20
0.39
0.18
−0.90
−2.90
2.6
−7.23
−5.50
−8.73
0.76
1.81
−10.74
LUMO
−11.50
HOMO
Energy Level/eV

◂**Fig. 12** Electrochemical and structural change of the CP-PDAB cathode material during the charge/discharge process: **a** charge/discharge profiles of the 1st cycle, **b** ex situ FTIR spectra, **c** charge/discharge redox reaction mechanism. Adapted with permission from Ref. [61]. Copyright©2022, Royal Society of Chemistry. **d** Energy levels of $[CuDEPP]^{2+}$, $[CuDEPP]^{+}$, [CuDEPP], $[CuDEPP]^{-}$, and $[CuDEPP]^{2-}$ based on DFT simulation study. Adapted with permission from Ref. [67]. Copyright©2021, Springer Nature

itself and more defects are more conducive to Na^+ ion storage, and the larger layer spacing was also conducive to fast transmission and diffusion of Na^+ ion. As shown in Fig. 15, the DFT calculation showed that the N/P co-doped structure had strong adsorption energy for Na^+ ion. Before P doping (Fig. 15 a and c), the adsorption energy between N6 (pyridine-N) and Na^+ ion was higher than that between N5 (pyrrorole-N). After P doping (Fig. 15b, d), the Na^+ ion adsorption energies for N5-NPSC and N6-NPSC increased to − 3.10 and − 2.57 eV, respectively. The enhanced adsorption energy suggested that the N/P co-doping structure was beneficial to the Na^+ ion adsorption. By calculating the state density (Fig. 15e and f) of NPSC and NSC near the Fermi level, it could be seen that N, P co-doped carbon had more electrons than N-doped carbon, suggesting that P doping further enhanced electron transport.

Graphene materials with expandable layer space and abundant defects can be used as efficient anodes for SIB. Heteroatom doping can enlarge the layer space and introduce defects. Yan et al. designed a graphene sheet co-doped with nitrogen and sulfur [79]. The introduction of heteroatoms could expand the interlayer space of the material and improve electrical conductivity, which was conducive to sodium ion insertion and electron transport. Zhou et al. designed a kind of N, S co-doped GO hollow spheres (NSGHS) [80]. The cooperative effect of N and S, the hollow structure, excellent porosity, and enlarged interlayer distance gave the NSGHS anode superb sodium storage performance. The S doping improved the binding between the sodium and graphene matrix to obtain a higher capacity. In addition, Chen et al. adjusted layer spacing by explosive decomposition thermal reduction graphene oxide (FSG) [81]. The highly porous structure, abundant surface oxygen-reducing groups, layer spacing of about 0.38–0.39 nm, were separated by large voids, which provided rapid mass transfer paths, and allowed the expansion and contraction of microcrystals during reversible Na embedding.

Titanium oxides. As the anode material of SIBs, titanium oxides have the advantages of being rich, safe and environmental friendly. Among them, TiO_2 is usually used as anodes for SIBs. According to different crystal structures, TiO_2 can be divided into rutile, anatase and bronze. However, its poor electron conductivity and low diffusion rate of Na^+ ions lead to the unsatisfactory electrochemical performance for TiO_2 [82, 83]. At present, many researchers have put forward many improvement measures to remedy the shortcomings of TiO_2 as an anode material for SIBs. It is mainly modified by doping of nitrogen, sulfur, fluorine and phosphorus, as well as by combining with carbon materials to form nanoarrays and heterostructures.

Kang et al. synthesized nitrogen-doped mesoporous TiO_2 ($NMTiO_2$) structures by controlled pyrolysis of MOF [84]. The porous structure provided a channel for the fast diffusion and transport of Na^+ ions. At the same time, the mixed $NMTiO_2$/NG full battery had super-strong cycle stability in 10 000 cycles of charge and discharge, showing an excellent capacity retention rate. Lu et al. suggested a defect-assisted phosphorus doping method to improve the electronic conductivity of TiO_2 and regulate its ion diffusion kinetics [85]. The DFT calculation results showed (Fig. 16) that when the P concentration was high, the state density (DOS) increased significantly (Fig. 16a, e, i) at the valence band maximum (VBM), and the charge density of TiO_2 around P also increased significantly (Fig. 16c, g, k). A high concentration of P introduction could efficiently promote the conductivity and lower the energy barrier of the sodium intercalation process (Fig. 16d, h, l), so as to improve the electrochemical performance. The surface functionalized TiO_2-x-P thin layer could endow TiO_2@TiO_2-x-P with significantly improved electronic conductivity and speeded sodium ion transport, which brought about an superb magnification performance (167 mAh g^{-1} at 10 A g^{-1}) as well as superior cyclability (capacity retention rates up to 99% over 5 000 cycles at 10 A g^{-1}). Fang et al. obtained a sodium titanate/titanium dioxide/C (C-NTC) heterostructure composite with oxygen vacancies (OVs). The cooperative effect of the OVs and heterostructure accelerated the electron/ion transfer dynamics, and the robust network structure and SEI membrane ensured its long cycle stability. In addition, low cost titanium oxide can also show high capacity and excellent rate performance. Compared with conventional TiO_2, the low-cost titanium oxide can perform the conversion reaction with excellent electrochemical properties. DFT calculations show that low Ti–O bond energy is beneficial to Ti–O bond fracture and recombination, leading to high capacity by multi-electron conversion reaction. The high conductivity of titanium oxide is favorable to the fast transfer of electrons, thus realizing a high electrochemical utilization [86].

3.2.3 Reaction Mechanism

Due to the unique open channel structure, TiO_2 can also act as a good host for Na insertion. The sodification/desorption process is shown in the equation: $xNa^+ + TiO_2 + xe^- \leftrightarrow Na_xTiO_2$. The stable storage mechanism is explored through ex situ and in situ XRD combined with the relationship between unit cell volume and charge/

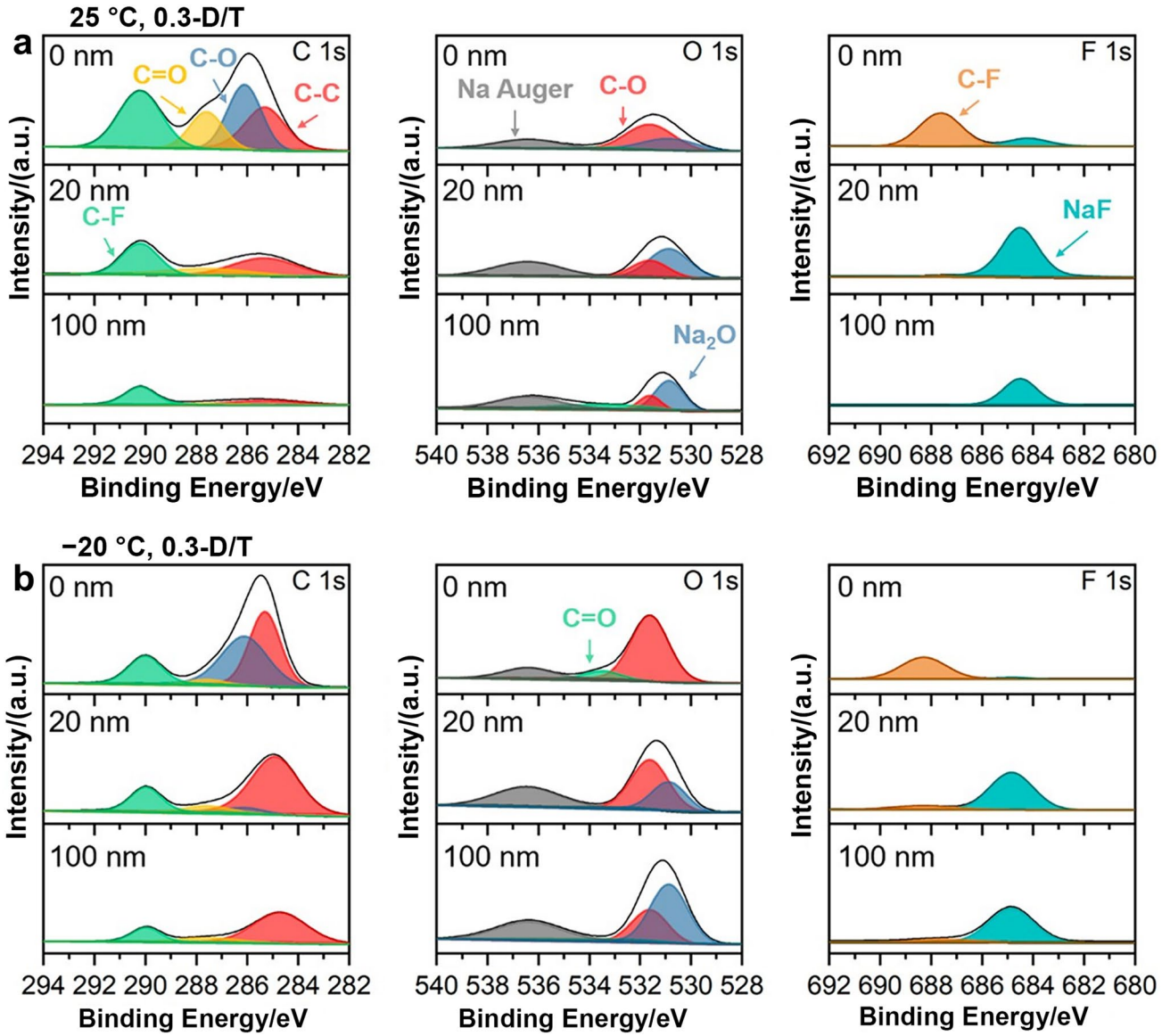

Fig. 13 High-resolution XPS spectra of C 1s, O 1s, and F 1s for Na metal after 10 cycles in the 0.3-D/T electrolyte at **a** 25 °C and **b** − 20 °C. Adapted with permission from Ref. [68]. Copyright©2022, American Chemical Society

discharge voltage. Figure 17a–d shows an outstanding reversible capacity and excellent mechanical integrity of the TiO_2@TiO_2-x-P upon charge/discharge process. This defect-assisted selective P-doping method also provided useful ideas for other heteroatomic doping (such as N, S, and B doping).

For soft carbon, the Na^+ storage mechanism is still difficult to determine clearly. Jian et al. studied the storage mechanism of soft carbon for the first time by in situ TEM and off situ XRD. When sodium ions were embedded in the graphene layer, resulting in an irreversible quasi-plateau at ~ 0.5 V relative to Na^+/Na, irreversible expansion could be observed. This high-potential platform was associated with the local structure of defects within the vortex-layer stack of soft carbon and the high binding energy associated with sodium ions. Soft carbon has more local defects and exhibits higher sodium potential than hard carbon. During the first sodiation process, the soft carbon exhibits long inclined regions above and below the quasi-platform, in which the inclined regions exhibit highly reversible behavior. The reversible capacity of soft carbon depends on the reversible binding of sodium ions to local defects (the vacancy on the sp^2 graphite layer) [87].

The way sodium interacts with hard carbon is mainly divided into three ways, namely adsorption at the surface active site, filling similar adsorption nanopore and embedding appropriate layer spacing. Most studies have shown that there are "adsorption-intercalation" and

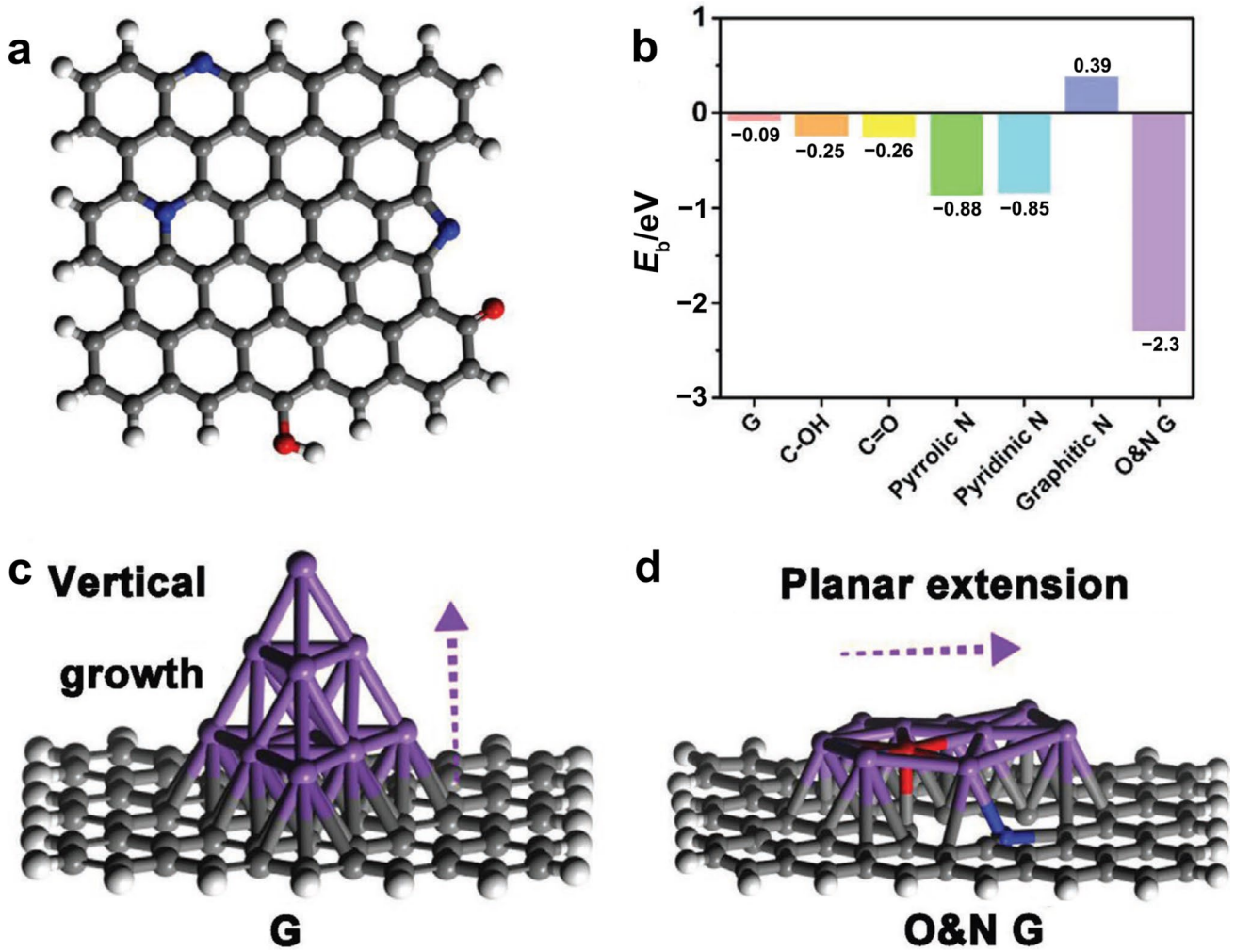

Fig. 14 **a** DFT theoretical structure model. **b** Comparison of the binding energy between the sodium atom and G modified by different functional groups. Schematic diagram of the Na^+ ion stacking mode **c** G and **d** O&N co-decorated G. Adapted with permission from Ref. [69]. Copyright©2021, Wiley–VCH

"intercalation-adsorption" storage mechanisms for sodium ions. For hard carbon, its storage mechanism is still controversial [88]. Initially, Stevens et al. demonstrated through in situ SAXS that the tilted regions were attributable to the embedding of sodium between the graphite layers and that the platform regions corresponded to the insertion of nanoporosity [89]. Qiu et al. revealed the "adsorption-intercalation" storage mechanism of sodium ions by in situ XRD and non-in situ NMR. The results showed that the high voltage inclined region was related to the adsorption of sodium ions, and in the other stage, sodium ions were embedded in the carbon material layers at appropriate spacing to form NaC_x compounds, resulting in a flat low voltage platform [90]. The enhancement of the flat low voltage platform in other words, the enhancement of sodium ion embedding is conducive to the improvement in reversible capacity and CE.

Yin et al. used in situ method (Raman spectroscopy and XRD) to demonstrate the sodium storage mechanism of the carbon material (HMm-1300-Zbe electrode) in charging and discharging process [91]. As indicated in the Raman spectrum (Fig. 18a, b), the I_D/I_G value continuously decreased after discharge, indicating the adsorption of sodium ions upon the surface of electrode materials or defect sites. From the Raman spectrum of HCM1300-ZBE, a new dual peak emerged at 1 450 cm^{-1} when discharged to about 0.45 V, indicating the generation of a new Na–C compound. C–O–Na species could be formed at ≈0.5–0.6 V by the reaction between oxygen functional groups and Na^+. In situ XRD (Fig. 18c) is used to illustrate that Na^+ is embedded between stacked graphene layers. The relative symmetry trend of XRD and Raman curves also indicated that the prepared HCM material had an excellent reversibility of sodium storage during the charge–discharge course.

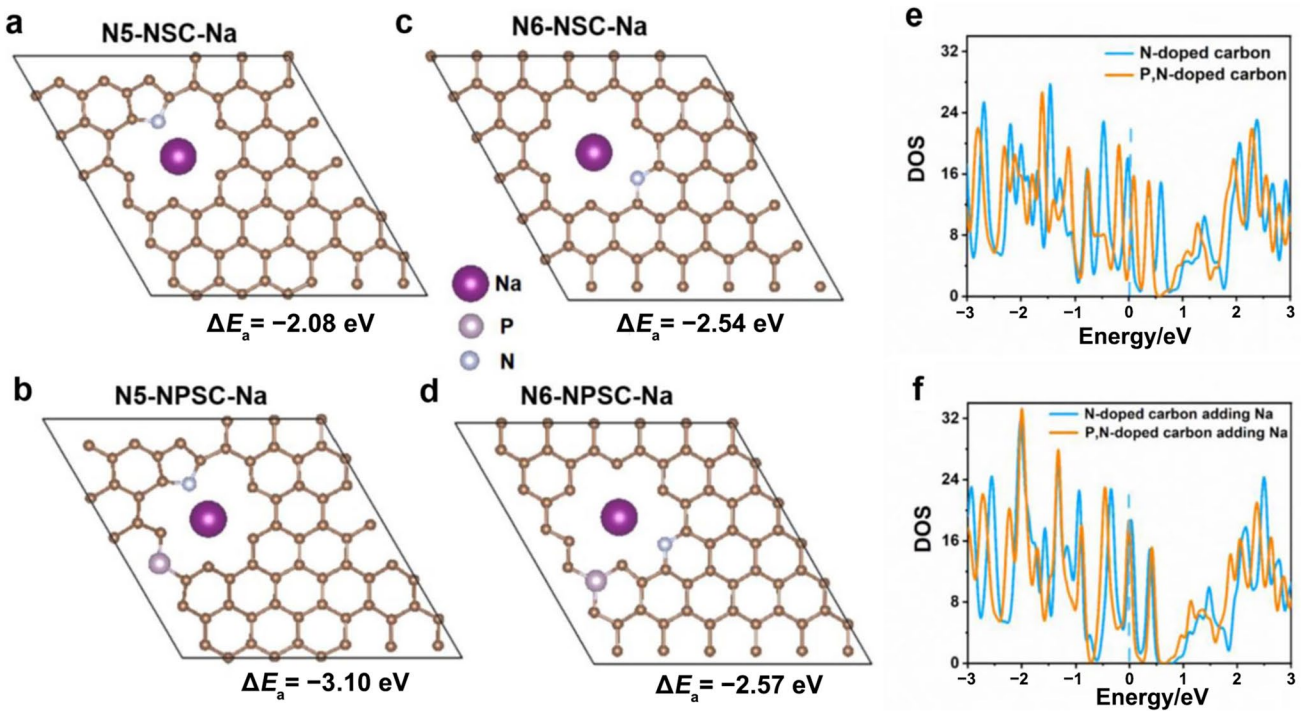

Fig. 15 Top view of a single sodium atom absorption **a** N5-NSC, **b** N5-NPSC, **c** N6-NSC and **d** N6-NPSC structures. TDOS for **e** the N6-NSC and N6-NPSC structures, and **f** N6-NSC and N6-NPSC after Na^+ ion absorption. Adapted with permission from Ref. [78]. Copyright©2022, Elsevier

3.3 Alloy-Type Materials for SIBs

The alloy-type anode materials have the largest theoretical specific capacity among the three types of anode materials, but their volume changes in the course of charge and discharge are the most significant.

3.3.1 Design Strategies and Synthesis Method

Up to now, the elements of the IV A (Pb, Sn, Ge, Si) and V A (Bi, Sb, P) have been studied extensively. The energy storage behavior of electrode materials is intimately relied upon its synthesis strategy. The chemical bonding, element distribution, structure and morphology of electrode materials are derived from their synthesis approaches, so electrode materials show numerous energy storage properties. Some common physical and chemical synthesis methods mainly include phase inversion, ball milling, thermal reduction, solvothermal, electrospinning and so on [92]. Many efforts have been made to solve the volume changes and electronic conductivity. For example, Liu used electrospinning to prepare ultra-fine Ge nanoparticles inserted in layered N-doped multi-channel carbon fibers, which mitigated massive volume expansion in the sodification and desodification cycles [93]. Ryu and co-workers designed multiscale hierarchical CMT@Bi-C material. Beneficial from the special and hierarchical structure, the anode material showed an ultrafast-charging capacity [94]. MOF material is a new type of porous material. MOF derivatives are also widely used as electrode materials. Li et al. synthesized superfine antimony in embedded porous carbon nanocomposite by conveniently in situ substituting Cu nanoparticles in an octahedral carbon framework derived from Cu-BTC [95]. This good electrochemical property was mainly attributed to the 3D porous carbon framework derived from MOF and ultra-fine Sb nanoparticles, which could both provide a penetration network for the speedy movement of charge carriers and mitigate the volume expansion and agglomeration of Sb in the cycle. In addition, defects can be introduced into the active anode materials and vacancies can be created in the active materials by dealloying to form porous nanoalloy materials. Nanoporous structure can effectively enhance electrolyte penetration and ion/electron migration, synchronously alleviating volume expansion. The structure formed by coating carbon material on the active materials has good electrochemical performance, which is beneficial to maintaining the integrity of the structure and providing flexible carbon matrix buffer volume change. Coupling of alloy-type anode with carbon-based material is regarded as one of the most promising methods to solve the problem of great volume variation and slow redox kinetics. However, due to the large proportion of carbon materials and low

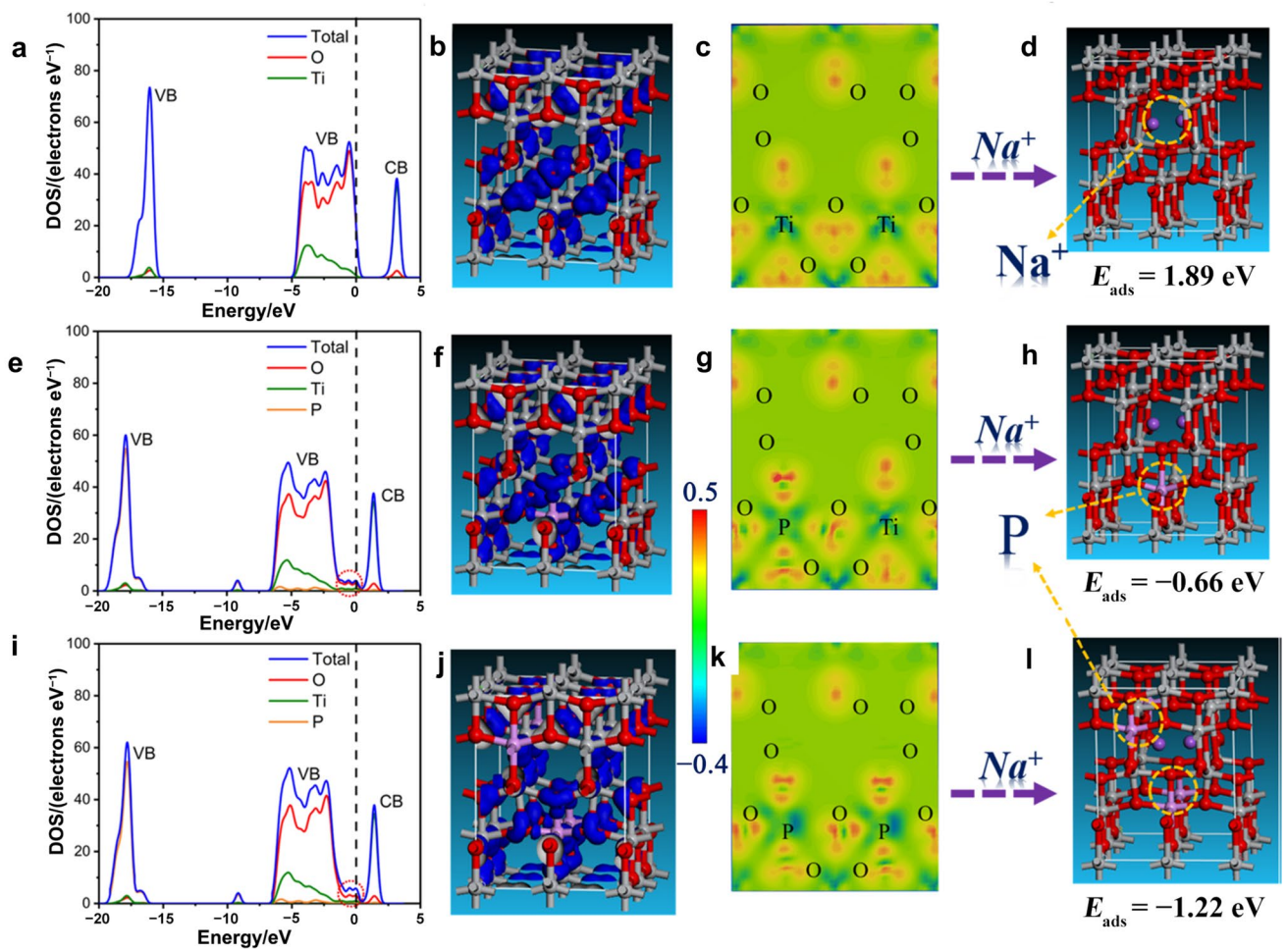

Fig. 16 **a**, **e**, **i** DOSs, **b**, **f**, **j** structural models, **c**, **g**, **k** charge density distributions, and **d**, **h**, **l** Na^+ ion inserted models for (**a**–**d**) pristine TiO_2, (**e**–**h**) TiO_2 with a low concentration of P introduction, and (**i**–**l**) TiO_2 with a high concentration of P introduction. Adapted with permission from Ref. [85]. Copyright©2019, American Chemical Society

sodium storage capacity, the specific capacity of the whole electrode will be greatly reduced. The alloy-type anode has a very high capacity and the research on high performance sodium storage will continue.

3.3.2 Active Sites and Surrounding Environments of Active Sites

Alloy-type anode materials possess an extraordinary theoretical specific capacity (300–2 000 mAh g^{-1}) and a lower sodium potential (< 1.0 V, Na/Na^+) [96], so it can be used as a good candidate material for the anode of SIBs. However, alloy-type anode materials have severe volumetric effects, resulting in dramatic volumetric expansion during alloying/dealloying with sodium, which easily causes structure breakage and electrode material powder. These shortcomings bring about the problems of short life and speedy capacity decay of alloy-type anode materials [97, 98].

Si can be alloyed with Na to obtain the NaSi phase which has a high theoretical capacity of 954 mAh g^{-1}, but simultaneously has a large volume effect in the alloying process with sodium (~ 420%). Moreover, the slow reaction kinetics and poor positive binding energy of Si and Na further hinder its application in SIBs. Qian et al. designed an amorphous silicon material as the anode electrode of SIBs that had a spongy structure, which had a more favorable binding between sodium and silicon and a reversible capacity of 176 mAh g^{-1} at 100 mA g^{-1} [99]. Due to the high diffusion barrier of Na in the Ge lattice, the activation energy of migration was high (1.5 eV). Similarly to silicon, the insertion/expulsion of Na^+ in Ge is also very difficult [100]. In order to solve the problem of poor Na^+ storage capacity of Ge-based materials, Chen et al. prepared a Cu_3Ge/Ge@N–C heterostructure material. The authors reached their conclusions by DFT calculation that the presence of Cu_3Ge/Ge heterostructure could slow the diffusion barrier

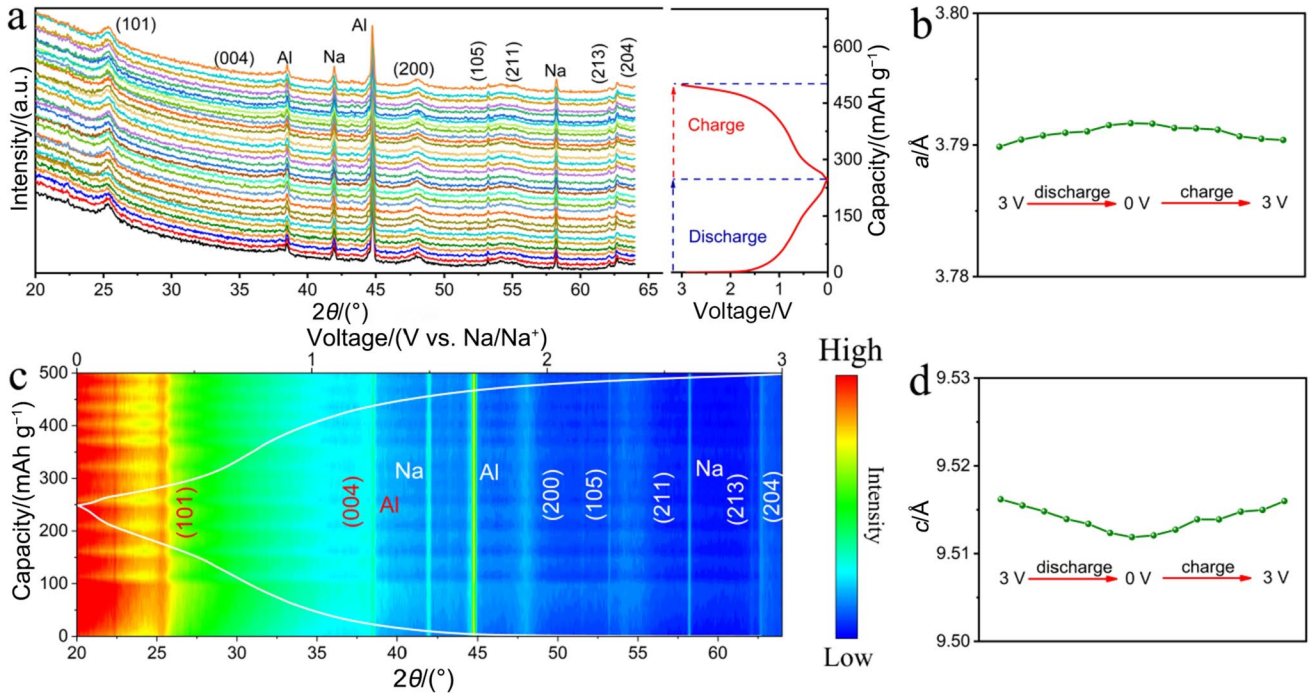

Fig. 17 **a** In situ XRD patterns and **c** contour plots of the TiO_2@TiO_2-x-P anode material in the 5th discharge-charge process at 50 mA g^{-1}. Refined structural parameters **b** *a*, **d** *c*, unit-cell volume as a function of charge−discharge voltage. Adapted with permission from Ref. [85]. Copyright©2019, American Chemical Society

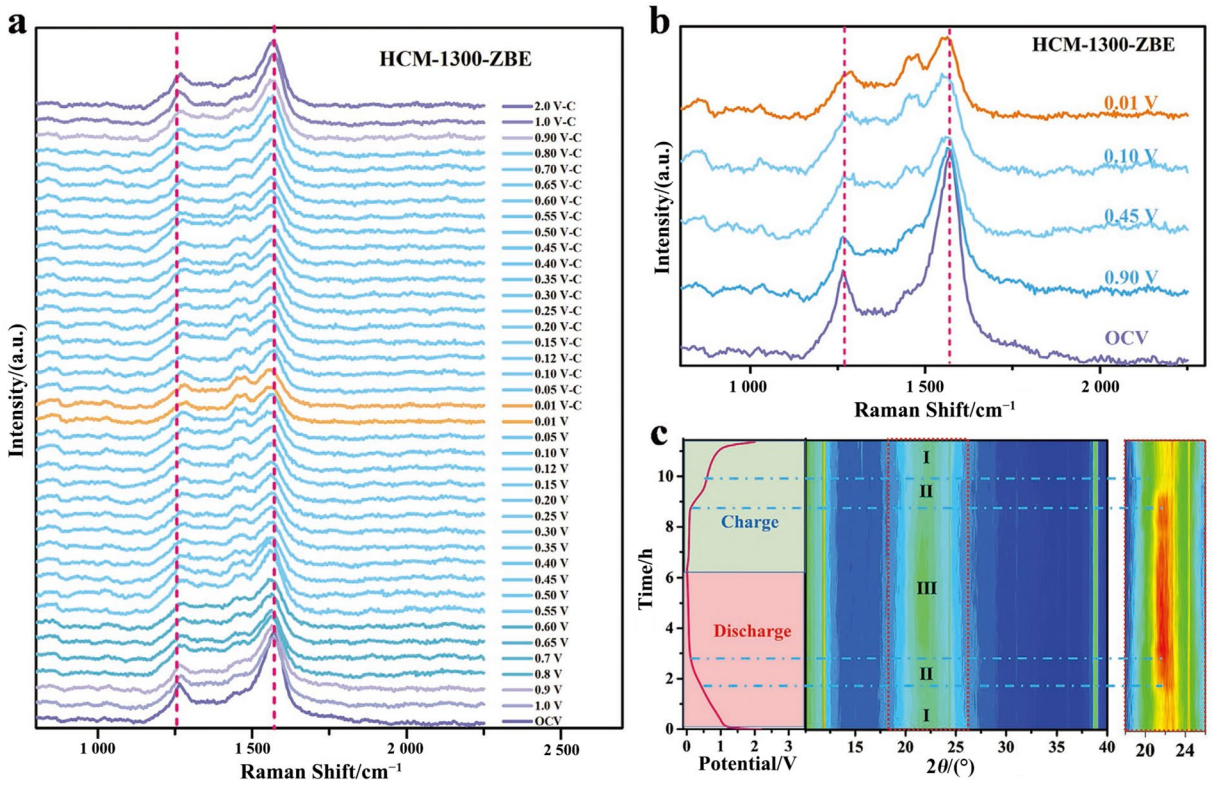

Fig. 18 In/ex situ measurement. **a**, **b** In situ Raman spectra of HCM-1300-ZBE. **c** In situ XRD analysis of the first cycle discharge-charge process of HCM-1300-ZBE at 0.1 A g^{-1} and 293 K. Adapted with permission from Ref. [91]. Copyright©2022, Wiley–VCH

of Na^+ and improve the alloying reaction of Ge [101]. The Cu_3Ge/GE@N–C possessed the pod-shaped structure, which could expose a huge number of active sites to reduce the ion transport pathway, while the outer carbon encapsulation could make the electrode material more stable. This material exhibited excellent rate properties (178 mAh g^{-1} at 2 A g^{-1}, 385 mAh g^{-1} at 0.05 A g^{-1}) and extremely long cycle properties (178 mAh g^{-1} at 4 A g^{-1} after 4 000 cycles). Lead's weight and toxicity have led to its limited use in SIBs, and it is not considered as a possible anode for SIBs [102]. Bi has a lower theoretical capacity, but its volume effect is smaller. And tin, phosphorus, antimony are commonly employed as alloy anode materials for SIBs [103], which have excellent theoretical specific capacity, but their large volume effect will hinder their further application in SIBs.

Designing active materials in combination with carbon composite materials is a common method to solve the aforementioned problems. Combining alloy-type material with carbon material can enhance electronic conductivity, cushion volume variation and impede the agglomeration of metal nanoparticles upon the cycling process. Taking into account the overall structure and composition factors, it is usually combined with reduced graphene oxide (rGO), MXene, carbon nanofibers (CNFs), nitrogen-doped carbon composites, etc. [104, 105]. Wu et al. synthesized Sb-@N,S-CNFs with longitudinal channels through a four-function template-assisted strategy, which greatly improved the diffusion dynamics of redox reactions, and greatly improved the cyclic stability and rate capability (219 mAh g^{-1} at 4 A g^{-1}) [106]. The synergistic effect between the heterogeneous interfaces and individual materials also made the construction of heterogeneous structures in electrode materials attract extensive attention. Xiong et al. prepared red phosphorus/black phosphorus heterostructures anchored on 3D nitrogenous graphene by solvothermal strategy, which showed high electronic conductivity and low diffusion barrier at the heterogenous interface of Na^+ [107].

Alloying is also a good approach for promoting the performance of alloy-type anodes. Alloying is used to change the morphology and active phase, improve the cycle stability of alloy anodes while maintaining high capacity. Jillian et al. studied the Sn, Bi, Sb ternary system and found that all elements were active against sodium [108]. The results displayed that the ternary alloy had a better capacity retention rate than any of the above single elemental anodes (Sn, Bi, Sb) [108]. Gao et al. proposed an alloying approach to synthesize nanoporous bismuth-antimony alloys via dealloying ternary Mg-based raw materials [109]. Sb has a high theoretical capacity, and Bi has a low theoretical capacity, but its volume effect is small. The appropriate Bi/Sb ratio, porous structure and alloying effect can effectively solve the problems existing in the alloy materials. Nanoporous structures and alloying effects facilitate electrolyte penetration and rapid electron and ion transport/diffuser and synergistic mitigation of volume expansion/contraction. Since then, Wang et al. have investigated the special crystal structure correlations and synergies of the Bi–Sb alloys, further explored the reasons for the capacity decay of the alloys [110]. They successfully synthesized the 3D Bi_3Sb_1/N-PC as a SIBs anode with an excellent rate capability (reversible capacity 318.3 mAh g^{-1} under 30 A g^{-1}), and a fair cycle stability (capacity decay is only 0.005 4% per cycle at 10 A g^{-1} after 6 000 cycles).

3.3.3 Reaction Mechanism

The charging and discharging mechanism of alloy-type anodes in SIBs is similar. An alloying reaction occurs between sodium and the active material during the charging process and a dealloying reaction occurs during the discharge process. Gao et al. used operando XRD technology combined with DFT calculation (Fig. 19) to explain the mechanism of the np-Bi_4Sb_4 alloys [(Bi, Sb) ↔ Na(Bi, Sb) ↔ Na_3(Bi, Sb)] [109]. The peak corresponding to (Bi, Sb) began to weaken at the first stage of continuous discharge [2.40–0.50 V (vs. Na^+/Na)]. Meanwhile, peaks associated with Na(Bi, Sb) (18.9°, 26.4°, 32.5°, 37.8°, and 42.1°) were observed and gradually increased, indicating that Na(Bi, Sb) was formed by the reaction between Na and (Bi, Sb). This conclusion provides much effective information for the study of alloy-type anode materials of SIBs.

Li et al. used ex situ XRD (Fig. 20a) to deeply investigate the electrochemical mechanism of the Sb@PC anode [95]. As the discharge continued, the peak strength associated with Sb gradually weakened, indicating an alloying reaction mechanism at the time of sodium insertion. The reflection of Na_xSb was reduced, eventually transforming into a hexagonal phase Na_3Sb at 26.7°. A series of diffraction peaks of Na_xSb and Sb disappeared completely when the voltage reached 0.01 V, indicating that Sb was completely transformed into Na_3Sb. The phase of Sb reappeared along with the disappearance of Na_3Sb when recharged to 0.4 V, indicating a reversible dealloying process from Na_3Sb to Sb. The corresponding diagram of sodification/desodification process is shown in Fig. 20c. The local structure evolution of Sb@PC was further discovered by the in situ Raman analysis (Fig. 20b). It was further proved that the alloying reaction of Na and Sb occurred during the discharge process and the Na_3Sb dealloying reaction occurred during the charging process.

3.4 Conversion-Type Materials

Unlike intercalation-type and alloy-type materials, conversion materials form a new compound along with the breach of old bonds and the generation of new bonds

during the process of adopting and releasing Na^+ ions. Similar to LIBs, the conversion processes in SIBs can be summarized as follows: $M_aX_b + bzNa \rightarrow aM + bNa_zX$, where X represents a nonmetal, M represents a metal, and z represents the formal oxidation state of X. The conversion anode materials are extensively regarded as perfect anode materials for SIBs owing to the extraordinary theoretical specific capacities. However, there are also some problems such as the volume effect and the easy agglomerate in the cycle process, which bring about poor cycle performance and capacity decay. In this part, the application of transition metal sulfides (TMSs) and transition metal oxides (TMOs) in SIBs is mainly introduced and discussed.

3.4.1 Design Strategies and Synthesis Method

A sequence of reliable synthesis strategies along with the research of conversion materials for SIBs has been reported. Here, we focus on the hydrothermal/solvothermal method, microwave method and electrospinning method. Hydrothermal and solvothermal methods are economical, environmentally friendly and effective in controlling the shape and size of the product. Therefore, they have been widely used in the synthesis of converted anode materials [111]. The solvothermal and hydrothermal methods differ in the reacted solvent. For example, in the synthesis of sulfides, metallic salts and sulfur sources are dissolved in specific solvents, poured into Teflon-lined sealed steel containers and reacted at the right temperature. The reaction process is facile and can be completed in one step. The microwave method is a kind of fast reaction speed, short time, high yield and economical method, which has been extensively used in the preparation of conversion-type materials. Thangavel et al. reported a microwave synthesis of SnS_2/G [112]. Metal source $SnCl_2$ and sulfur source thioureone were evenly dispersed in the GO solution and placed in a microwave oven at 700 W for 20 min. The results showed that the microwave method not only effectively reduced the reaction time, but also increased the yield and made it possible for large-scale production. Electrospinning is a simple and controllable method that has been extensively used to fabricate one-dimensional materials. By adjusting the parameters of the electrospinning process, the size and morphology of the acquired fibers can be changed. In recent years, electrospinning has also gained popularity in sodium storage. The reasons are as follows: first of all, electrospinning has the advantage of mass production, which lays a solid foundation for the industrial preparation of electrode materials; secondly, electrode materials prepared by the electrospinning method possess the advantages of low cost, short ion diffusion distance and enhanced cycle life and high energy density [113].

3.4.2 Active Sites and Surrounding Environments of Active Sites

Transition metal oxides. There are plenty of metal oxides possessing high theoretical specific capacities used in SIBs, for example, Fe, Co, Cu and Sn-based TMOs. Based on the disadvantages and advantages of transformational anode materials, many research teams have modified the materials.

Fe-based TMOs. Iron oxide materials (Fe_2O_3 or Fe_3O_4) have been extensively investigated owing to low price, abundant

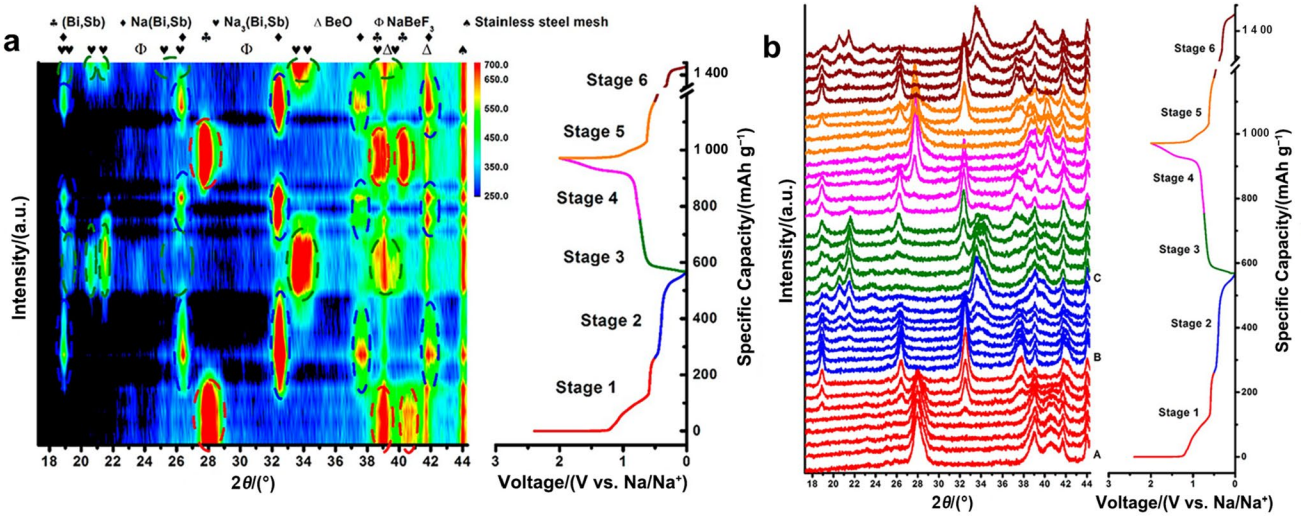

Fig. 19 **a** Contour plot and **b** line plot of the operando XRD patterns of the np-Bi_4Sb_4 anode material during the discharge/charge processes. Adapted with permission from Ref. [109]. Copyright©2018, American Chemical Society

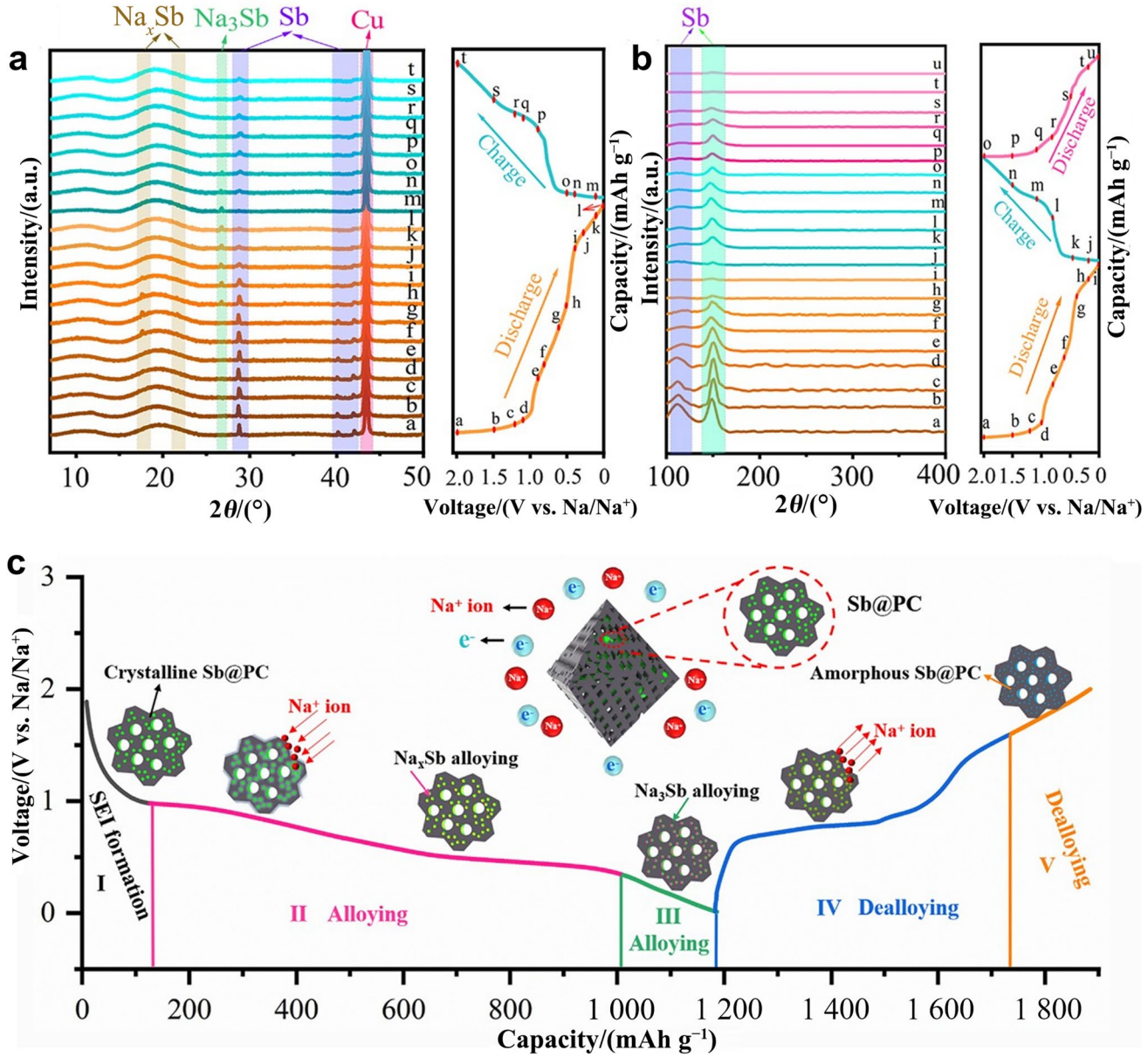

Fig. 20 **a** Ex situ XRD patterns and **b** in situ Raman spectra of Sb@PC anode material at 0.03 A g^{-1}. **c** Simulation diagram of sodification/desodification process. Adapted with permission from Ref. [95]. Copyright©2021, American Chemical Society

resources and environmental friendliness. However, like most transition metal oxides, iron oxide has poor rate performance and cycle stability. Many groups are working to promote the capacity and cycling life of iron oxide-based electrodes [114]. Designing various nanomaterials in combination with carbonaceous materials is a good approach. Hou et al. synthesized a nanocomposite in which the mesoporous graphitic carbon was encapsulated on Fe_2O_3 (Fe_2O_3@mGC) [115]. Fe_2O_3@mGC showed superb cycling stability, providing a specific capacity of 377 mAh g^{-1} and extraordinary Coulomb efficiency (98%) under 100 mA g^{-1} for 100 cycles. Firstly, large pore volume and high specific surface area were conducive to ion transfer and adapted to large volume changes. Secondly, ultrafine Fe_2O_3 nanocrystals effectively reduced the diffusion length of Na^+. Finally, graphite-carbon encapsulation improved the electronic conductivity. Zhong et al. reported an N-doped carbon covering porous spindle-shaped Fe_3O_4 distributed on graphene (Fe_3O_4@NCm/rGO) composite [116]. Fe_3O_4@NCm/rGO delivered a superior specific capacity of 237 mAh g^{-1} at 1.0 A g^{-1} for 2 500 cycles. The effective role of carbon and rGO as a buffer region could prevent the Fe_3O_4 volume variation in the cycle. Both Fe_2O_3 and Fe_3O_4, the active site of the reaction is the metal center, that is, the one-step conversion reaction between iron oxide and sodium.

Co-based TMOs. Co_3O_4 is an ideal alternative because of the high theoretical capacity of 890 mAh g^{-1}. However, during Na^+ ion insertion/extraction, its poor conductivity, severe volume expansion led to poor cycling stability, which limit the application of this material. The researchers propose two methods to address these drawbacks. One improved method is to design a variety of nanostructured electrode materials (such as nanotubes, nanosheets, hollow spheres, etc.) to enhance the structural stability, but this method is difficult to improve the conductivity [117]. Another approach is to combine Co_3O_4 with a carbon matrix to improve electrical conductivity [118]. Based on the above analysis, it is an effective strategy to design a variety of nanostructured electrode materials and combine them with carbonaceous materials. Jiang et al. synthesized Co_3O_4 microflowers and porous cubes with controllable dimensions [119]. The porous structure of the Co_3O_4 cube could offer plentiful diffusion paths for sodium ions and effectively alleviate volume expansion. Moreover, uniform carbon doping efficiently improved the electrical conductivity of the nanocomposites. Therefore, there was excellent cyclic stability in the field of SIBs. The rambutan-like hybrid hollow spheres of carbon-constrained Co_3O_4 nanoparticles (R-Co_3O_4/C) have been prepared via a facile one-pot heat treatment and post-annealing [120]. The active site of the reaction in Co_3O_4 was the metal center, which was the one-step conversion reaction between Co_3O_4 and sodium. The hierarchical hollow structure could greatly enhance the structural stability and rapid electrode kinetics, which would provide a way to solve the problems of slow oxidation/dehydrogenation kinetics and poor structural stability of TMOs. The capacity of R-Co_3O_4/C maintained 223 mAh g^{-1} at a current density of 5 A g^{-1} when utilized as anode materials in SIBs (Fig. 21a). As indicated in Fig. 21b, the excellent rate performance of R-Co_3O_4/C electrode was mainly because of the special hollow structure. What is more, the electrode showed 74.5% capacity retention for 500 cycles under a current density of 0.5 A g^{-1} (Fig. 21c).

Cu-based TMOs. Copper oxide (CuO) is an ideal candidate because of the abundant resources and its extraordinary theoretical capacity (674 mAh g^{-1}) [121]. The active site of the conversion reaction in CuO is the metal center. Jiang's group reported a structural design to achieve a durable sodium anode consisting of a TiO_2-mediated CuO (denoted as R-CuO) nanowire array on Cu foams [122]. The R-CuO provided the capacity of 592 mAh g^{-1} and outstanding cyclability (82% over 1 000 cycles), which was mainly because of the mechanical stability of the electrode material guaranteed by TiO_2 during the embedding and de-embedding of sodium ions. Zhao et al. showed a simple technique to fabricate hollow CuO nanocubes that helped slow volume change in the charging/discharging procedure [123]. The hollow CuO nanocubes showed a capacity of 865 mAh g^{-1} under 0.1 A g^{-1} for 100 cycles. According to CV curves, two peaks appeared at 1.02 V and 0.48 V during the first cycle, attributing to CuO reduction and SEI layer formation. The oxidation peak occurred at 2.13 V, corresponding to CuO formation. The reduction peaks at 0.52 and 0.48 V were related to the conversion of the CuO phase to Cu and Na_2O in the subsequent cycles.

Sn-based TMOs. The metal center as the active site can undergo both the conversion reaction and the alloying reaction with Na^+ ion. SnO_2 has a low potential and a high capacity, however, its low conductivity and large volume expansion significantly impede its applications. The combination with carbonaceous materials and nanostructured materials has been considered as a rational approach to improve the cycle stability and enhance the electrical conductivity. Wang's group reported a method derived from organic compounds containing heteroatoms to synthesize sulfur/nitrogen Co-doped graphene/SnO_2 composites (denoted as SNGS) [124]. Due to the improvement in the conductivity of ultrafine SnO_2 nanocrystals, doped heteroatoms limiting the agglomeration of SnO_2, the SNGS sample exhibited outstanding performance with satisfied reversible capacity and excellent cycling stability. Zhang et al. reported a method for producing carbon nanofibers encapsulated with oxygen vacancy SnO_{2-x} nanoparticles, while the use of oxygen vacancies effectively controlled the electronic structure of semiconductor oxides, enhancing the reversible capacity and the rate capability [125]. The SnO_{2-x}/C electrode showed an outstanding specific capacity of 340 mAh g^{-1} under the current density of 5.0 A g^{-1} and an excellent cycle stability of 447 mAh g^{-1} at 1.0 A g^{-1} after 2 500 cycles.

In conclusion, when TMOs are hybridized with carbon-based matrix or size of the electrode materials is reduced, it can effectively solve the shortcomings of low conductivity, poor cycle stability and poor rate performance and offer new understandings for the design of current SIBs anode materials. Additionally, the properties of these electrode materials can be significantly improved through rational structural selection and the combination of hybrid nanostructures, which lays a foundation for future commercial development.

Transition metal sulfides. TMSs as sodium storage materials with a higher theoretical capacity have attracted extensive attention in comparison with TMOs. Moreover, M–S bonds in TMSs are weaker than M–O bonds in TMOs, which is conducive to the conversion process with Na^+ ions, so that TMSs have an obvious advantage in the course of sodiation/desodiation. In addition, Na_2S produced by TMSs during the discharging process have better reversibility than Na_2O produced by TMOs [126], which exhibits better mechanical stability. Therefore, various TMSs have been widely studied as SIBs high-capacity anode materials,

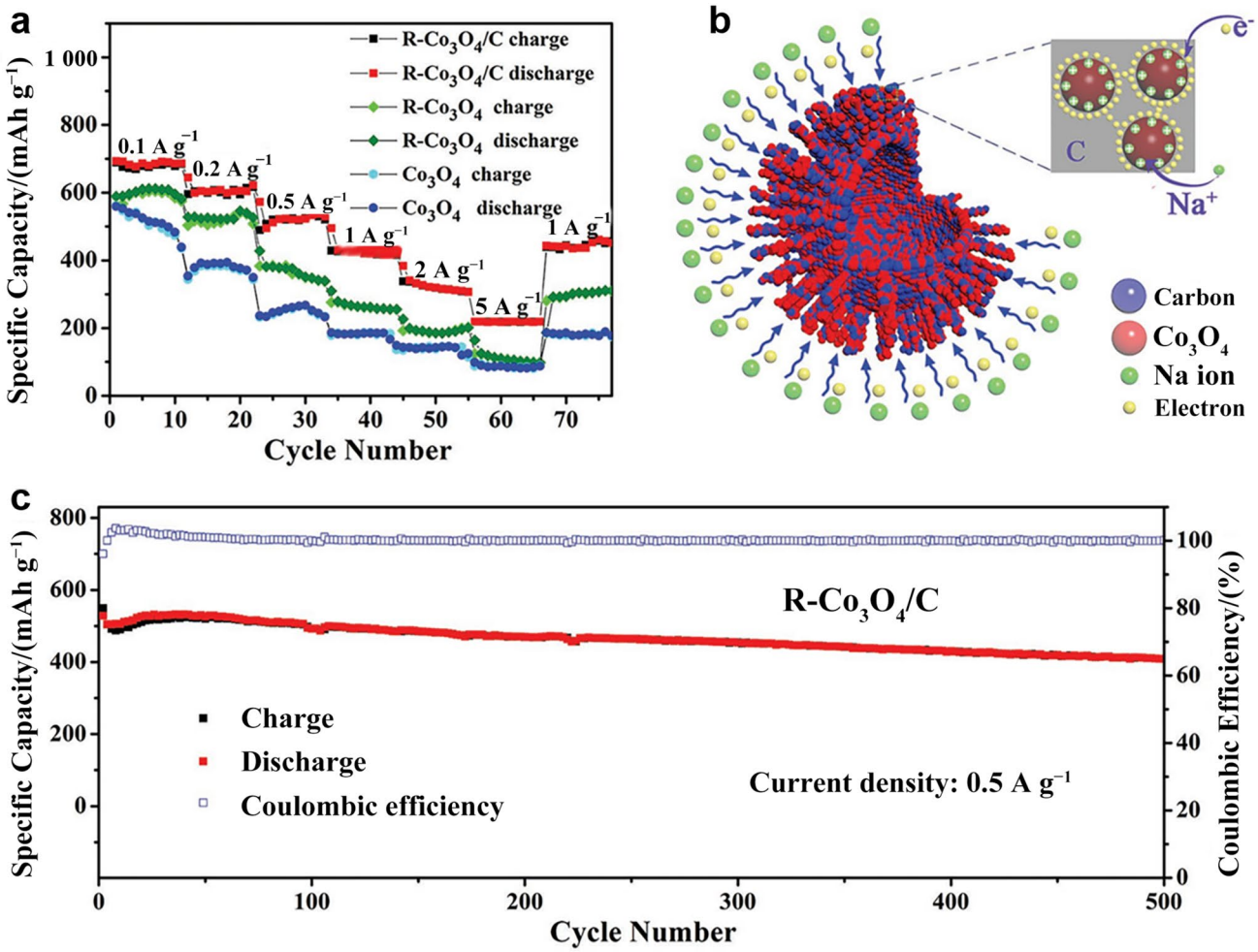

Fig. 21 **a** Rate performances of the R-Co_3O_4/C hybrid hollow sphere, R-Co_3O_4 hollow sphere, and Co_3O_4 solid sphere electrodes. **b** Schematic diagram of the advantages of the R-Co_3O_4/C hybrid hollow sphere in sodiation and desodiation. **c** Cycle performance of the R-Co_3O_4/C hybrid hollow sphere electrode at a high current density of 0.5 A g^{-1}. Adapted with permission from Ref. [120]. Copyright©2018, Wiley–VCH

such as Mo, Co, Fe, Cu and Sn-based TMSs. But the inadequate conductivity of TMSs and large volume change in the cycling course have hindered their application.

Mo-based TMSs. Molybdenum disulfide (MoS_2) is one kind of typical two-dimensional layered metal sulfide. The layers are associated by van der Waals gravity, leading to a large intercalation interval (0.62 nm) and a high specific surface area, which sufficiently provides convenience for the intercalation of basic ions such as Li^+, Na^+ and Mg^{2+} [127, 128]. MoS_2 has a high theoretical capacity, but its inherent conductivity is poor, and its volume changes during electrochemical cycling are serious, limiting its further application [129, 130]. Zhang et al. successfully fabricated the flower ball composites named CNT/MoS_2/NC [131], carbon nanotubes could promote the conductivity of anode materials and effectively slow the agglomeration of electrode materials during the electrochemical cycle. In addition, the nitrogen-doped carbon derived from cetyltrimethyl ammonium bromide (CTAB) was inserted into MoS_2 crystal interlayer at the level of molecular to protect MoS_2 layer by layer and further improve the conductivity of MoS_2. Due to the synergistic action of two carbonaceous materials, the prepared CNT/MoS_2/NC composite showed excellent sodium storage performance. In addition to composite carbon materials, the construction of heterogeneous materials is another useful strategy toward solving the shortcomings of MoS_2 [132–135]. The abundant phase interface provides a large number of defects and plentiful active sites for speedy electron/ion transport, which significantly enhances the electrochemical performance of the materials [136–139]. Chen's team synthesized a novel MnS-MoS_2 heterogeneous complex (MnS-MoS_2) by hydrothermal method [140]. MnS nanoparticles were dispersed on MoS_2 nanosheets uniformly. The phase transition generated by the heterogeneous structure

and the internal electric field improved the stability and the electrochemical reaction kinetics of the electrode materials. MnS-MoS_2 exhibited excellent sodium storage properties. This study provides a novel way to understand the role of heterogeneous structures in energy storage. Chen et al. successfully constructed $CoSe_2$CNC@NC/MoS_2 (denoted as CMC-1) heterostructure by a multistep reaction strategy [141]. Due to the construction of heterogeneous structures, interfaces were formed between different components, and abundant phase interfaces provided a large number of active sites and defects for the speedy transport of electrons/ions. The nitrogen-doped carbon skeleton was applied to anchor $CoSe_2$ nanoparticles, which could efficiently alleviate volume expansion in the reactions. The active sites were the metal centers cobalt and molybdenum, while the intercalation and conversion reaction occurred in a two-step reaction mechanism. HRTEM images (Fig. 22a) and XRD patterns (Fig. 22b) proved that a heterogeneous interface was formed between $CoSe_2$ and MoS_2. As an SIB anode, the heterostructure provided an excellent reversible capacity of 481.6 mAh g^{-1} at 0.5 A g^{-1} for 100 cycles (Fig. 22c), favorable rate performance (174.5 mAh g^{-1} at 20.0 A g^{-1}, Fig. 22d) and outstanding cycle stability (333.4 mAh g^{-1} after 2 000 cycles at 5.0 A g^{-1}, Fig. 22e).

Fe-based TMSs. Pyrite (FeS_2) is considered as a kind of potential anode material for SIBs because of its abundant reserves, environmental friendliness and low cost [142, 143]. In addition, FeS_2 possesses a high theoretical capacity of 894 mAh g^{-1}. Nevertheless, FeS_2 has a low conductivity and a severe volume change problem in the charging and discharging procedure, which brings about poor electrochemical performance [144, 145]. To address the aforementioned issues, researchers have done a lot of work to adjust the voltage range, composite conductive materials, and design a variety of electrode nanostructures. Chen et al. found that controlling part of the conversion reaction can promote the cyclic stability of the reaction, resulting in the long-term cycle of FeS@C with high capacity [146]. Chen et al. came up with a way to adjust cutoff voltage to 0.8 V, allowing FeS_2 to achieve superior cycle stability (90% capacity retention over 20 000 cycles) and surprisingly high rate performance (170 mAh g^{-1} at the current density of 20.0 A g^{-1}) [147]. Zhang et al. designed and prepared a core–shell structure FeS_2@rGO nanocomposite material. The rGO sheets could improve electrical conductivity while buffering volume changes in the charging and discharging procedure. Additionally, the special core–shell configuration and the control of voltage range could further improve the electrochemical performance. FeS_2@rGO showed good cyclic stability and excellent rate performance [148]. Mi et al. reported a novel FeS_2/rGO-A composite [149]. The introduction of a three-dimensional conductive network rGO-A as FeS_2 improved the conductivity of the entire electrode. It greatly slowed the loss of active substances. The FeS_2/rGO-A electrode showed excellent cycling and rate performance. The N, S co-doped carbon fiber covered with FeS_2 nanoparticles was synthesized and anchored on FeS_2 nanosheets (denoted as FeS_2@CF-NS) [150]. The active site was the metal center, consisting of the insertion and conversion reaction, which was a two-step operation mechanism. FeS_2 nanosheets and FeS_2 nanoparticles not only expanded the accessibility between the electrode and the electrolyte, but also reduced the diffusion distance of ions. N and S co-doping enhanced the transport of charge carriers, and alleviated the volume change in the conversion reaction. Therefore, FeS_2@CF-NS showed significant sodium storage properties. FeS_2@CF-NS showed a good rate performance (144.4 mAh g^{-1} at 20.0 A g^{-1}) and an excellent capacity of 637.1 mAh g^{-1} (at 1.0 A g^{-1} after 400 cycles). When $Na_3V_2(PO4)_3$-C was used as the cathode, FeS_2@CF-NS also achieved outstanding rate performance (297.4 mAh g^{-1} at 10.0 A g^{-1}) and a very high specific capacity of 561.1 mAh g^{-1} (at 1.0 A g^{-1} after 500 cycles) in the full battery.

Cu-based TMSs. Copper sulfide possesses abundant resources, moderate cost and high theoretical capacity, which has been the focus of the application of anode materials for SIBs. However, its rapid capacity decay and poor rate performance hinder practical application in SIBs. The batteries behaviors of copper sulfide are improved through the combination of copper sulfide with carbon material and the design of a nanometer electrode material with special structure. In the process of Na^+ storage, the active site is the metal center copper. Li et al. prepared a graphdiyne (GDY) nanomembrane-filled array of CuS nanotubes (named as CuS-NTAs@GDY) [151]. The in situ protection of GDY nanomembranes not only improved the structural stability of the electrode materials, but also enhanced the conductivity. CuS-NTAs@GDY exhibited excellent electrochemical sodium storage capabilities. Wang et al. synthesized an octahedral composite assembled from carbon-coated copper sulfide nanorods (CuS_x@C) [152]. Carbon cladding and nanostructures enhanced electrical conductivity and buffered volume expansion. In addition, nanostructures also shortened ion and electron transport paths. Our group designed and synthesized Cu_9S_5, which was covered with the N-doped carbon shell and assembled into a flower shape composed of nanorods (labeled as Cu_9S_5@NC) [153]. It exhibited a high capacity (263.5 mAh g^{-1} under 200 mA g^{-1} over 200 cycles), outstanding cyclability (199.8 mAh g^{-1} after 10 000 cycles at 5 A g^{-1}) and outstanding rate performance (297.8 mAh g^{-1} at 8 A g^{-1}) in SIBs, which could be attributed to the shortened ionic diffusion length by nano-Cu_9S_5 particles, the slowing of volume change by hierarchical structure. In addition, the short nanorod was beneficial to the penetration of the electrolyte, while the N-doped carbon shell could improve electronic conductivity.

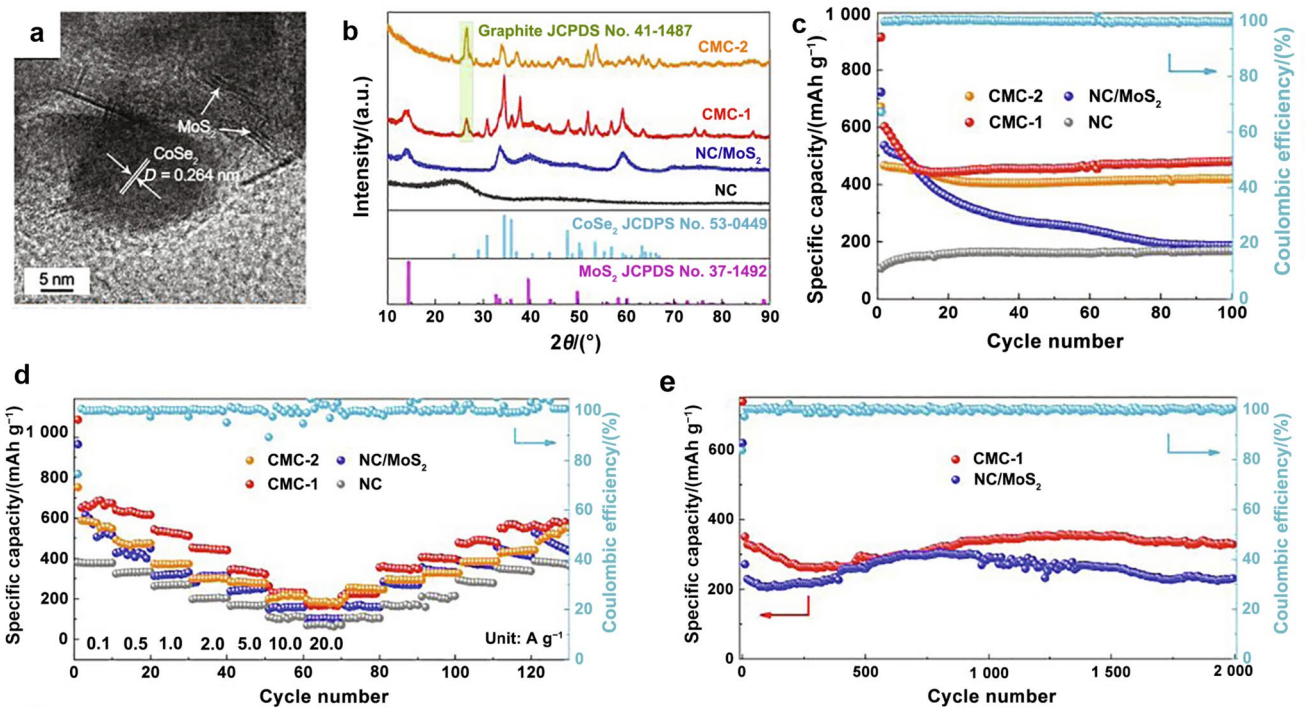

Fig. 22 **a** HRTEM image of CMC-1. **b** XRD patterns of CMC-1 and other composites. **c** Cycle performance at 0.5 A g^{-1} for 100 cycles. **d** Rate performance of CMC-1 and other composites. **e** The long-term cycle performance at 5.0 A g^{-1} for 2 000 cycles of CMC-1 and other composites. Adapted with permission from Ref. [141]. Copyright©2022, Elsevier

Sn-Based TMS: Owing to the high theoretical capacity, the combination of alloying and conversion electrochemical reactions, tin sulfides (SnS_2, SnS) have attracted extensive attention [154, 155]. Nevertheless, the huge volume change during electrochemical reactions and poor electrical conductivity bring about poor cyclic stability. For the purpose of effectively solving the aforementioned problems, several effective strategies have been used, such as the design of nanostructures [156–158], heteroatomic doping [159–161] and binding to carbonaceous materials [162–164]. Wang et al. reported a superlattice-like SnS/ N-doped graphene (NG) mixture consisting of SnS and NG nanosheets that were alternately stacked [165]. First, the SnS was located between the NG nanosheet layers in the SnS/NG mixture, thus widening the spacing of the SnS layers and exposing more SnS active sites, which facilitated rapid ion diffusion. In addition, the NG layer improved the electrical conductivity and provided space to cushion the volume alteration of SnS in the composite. Therefore, the superlattice-like SnS/NG anode showed good rate performance (550 mAh g^{-1} at 14.58 A g^{-1}) and cyclability (600 mAh g^{-1} at 1.6 A g^{-1} after 1 200 cycles). Cui et al. proposed an innovative approach to restrict SnS nanomaterials to Co, N modified porous carbon fibers and vertical graphene-like carbon films (CCF@SnS@G) to improve energy storage performance [166]. Initially, the Co, N modified carbon fiber supported the SnS nanosheet array while enhancing electrical conductivity. Furthermore, the graphene-like carbon film formed in situ acted as a protective skeleton for the SnS to prevent structural damage and enhance electronic conductivity. The conversion reaction of SnS to Na_2S and Sn occurred in the discharge process, which was accompanied by the alloying reaction of Na_xSn. The dealloying reaction of Na_xSn and the reversible conversion of Na_2S and Sn into the SnS phase occurred during the charging process. Lu et al. synthesized a nanocellular SnS/SnS_2 heterostructure (denoted as SnS/SnS_2@CC) grown on a carbon cloth substrate [167]. Because the heterogeneous structure could enhance the dynamic process, SnS/SnS_2@CC showed a high capacity and superior cycling performance. Improving electrochemical properties by forming heterogeneous structures may uncover new ways toward the engineering and construction of electrode materials.

In summary, the optimization strategies of TMSs are mainly divided into three methods: (1) nanomaterials, (2) composite with carbon materials, and (3) heterogeneous structure construction. Nanomaterials can effectively buffer volume changes. The TMSs are combined with the carbonaceous material to improve the conductivity

to a greater extent while alleviating the volume change. The formation of heterogeneous structures accelerates the interfacial charge transfer and increases the electrochemical kinetics rate. The combination of one or more strategies can significantly promote the electrochemical properties of TMSs.

3.4.3 Reaction Mechanism

For TMOs, XRD, XPS combined with CV curves are common methods to study the conversion mechanism. According to ex situ XRD and XPS of Co 2p in R-Co_3O_4/C (Fig. 23a and b), when discharged to 0.01 V, the peak of Na_2O was observed and the peak of Co_3O_4 disappeared, and the peaks of Co^{2+} and Co^{3+} disappeared after fully discharged. The results indicated that Co_3O_4 was converted to Na_2O and Co metal during the discharging process. Subsequently, these phases change backed to Co_3O_4 and Na after the charging process [120]. The first three CV curves (Fig. 23c) examined the Na^+ storage performance of the SnO_{2-x}/C. In the initial discharge process of 0.75–1.3 V, the obvious peaks indicated that the SnO_2 phase was converted to Sn and Na_2O. The equations are described as follows:

$$SnO_2 + 2Na^+ + 2e^- \leftrightarrow SnO + Na_2O$$

$$SnO + 2Na^+ + 2e^- \leftrightarrow Sn + Na_2O$$

As shown in the equation below, the reduction peak at 0.23 V was the result of the alloy reaction:

$$Sn + xNa^+ + xe^- \leftrightarrow Na_xSn\ (0 \leqslant x \leqslant 3.75)$$

The three oxidation peaks at 0.5, 1.05 and 1.25 V were from the dealloying of Na_xSn to Sn, the subsequent oxidation of Sn to SnO and the further oxidation of SnO to SnO_2. The XRD results of the SnO_{2-x}/C electrode at different charge/discharge states of the 20th cycle also showed the same reaction mechanism (Fig. 23d). During the discharge process, new peaks were indexed to SnO and Sn phases appeared at 2θ of 50.7° and 43.8° indicating the gradual conversion reaction of SnO_2. The peaks of SnO_2, SnO and Sn almost disappeared at 0.01 V, and the peaks located at 2θ of 29.4°, 47.5° and 48.6° might belong to the Na_xSn alloy phase, showing a sufficient alloying reaction between Na^+ ion and Sn. On the contrary, the peaks of the alloy phase of Na_xSn gradually disappeared during the charging process, which was related to the rebuild of the Sn, SnO and SnO_2 phases. As shown in Fig. 23e, the reasons for the excellent sodium storage electrochemical performance of the SnO_{2-x}/C electrodes are as follows: Firstly, SnO_{2-x}/C electrode could effectively inhibit the aggregation and separation of Sn and Na_2O phase and also reduce the large volume variation during the charge/discharge process. Secondly, SnO_{2-x}/C electrodes not only provided a favorable way for ion transport, but also could form a stable SEI film [125].

The mechanism of sodium ions storage for TMSs was studied by ex situ XRD and XPS. The following reaction mechanism was proposed [141]:

$$CoSe_2 + Na^+ + e^- \leftrightarrow Co^{2+} + Co + Na_2Se$$

$$MoS_2 + Na^+ + e^- \leftrightarrow Na_2Mo_3S_4 + Na_2S + e^- \leftrightarrow Mo + Na_2S$$

The investigation of the conversion of Cu_9S_5@NC anode in the electrochemical reaction process was also used ex situ XRD and HRTEM tests. During the discharging process, Na^+ ions were inserted into the lattice of Cu_9S_5, and a peak of 26.65° appeared corresponding to $NaCu_2S_2$. During the charging process, Cu_2S peak at 39.71° appeared, indicating that Na^+ ions generated Cu_2S from the unplugged part of the $NaCu_2S_2$, and a Cu_9S_5 peak also appeared. At discharge to 1.18 V, the (353) plane of Na_2S and the (1, 0, 10) plane of Cu_9S_5 could be observed. When charged to 1.84 V, the (111) plane of Cu and the (004) plane of Cu_2S could be observed. HRTEM also confirmed the above results [153].

3.5 MOFs-Based Materials

MOFs are constructed by the self-assembly of inorganic metal centers and organic ligands through coordination bonds, which is a kind of very promising porous materials. MOFs are extensively applied in gas storage and separation [168], catalysis [169], energy storage and conversion [170] thanks to their merits of large surface area, regular porous structure and modifiable pore size. At present, MOFs are often used as precursors to produce various derived materials in the field of SIBs [171, 172]. Nevertheless, during the synthesis of MOFs derivatives, the crystal structure, morphology and pore size of pristine MOFs are damaged to some extent, which affects their electrochemical performance. Therefore, pristine MOFs directly used as electrode materials will avoid the above problems. In this section, MOF-based anode materials for SIBs are discussed mainly from the active sites, the environment around the active sites and the reaction mechanism. Pristine MOFs as active materials are introduced emphatically.

3.5.1 Design Strategies and Synthesis Method

Due to the controllability of MOFs, their physical and chemical properties can be regulated in the synthesis process [173]. MOFs can be constructed by a variety of methods, some of which are widely used as described below. For example, diffusion method, solvothermal method, ultrasonic

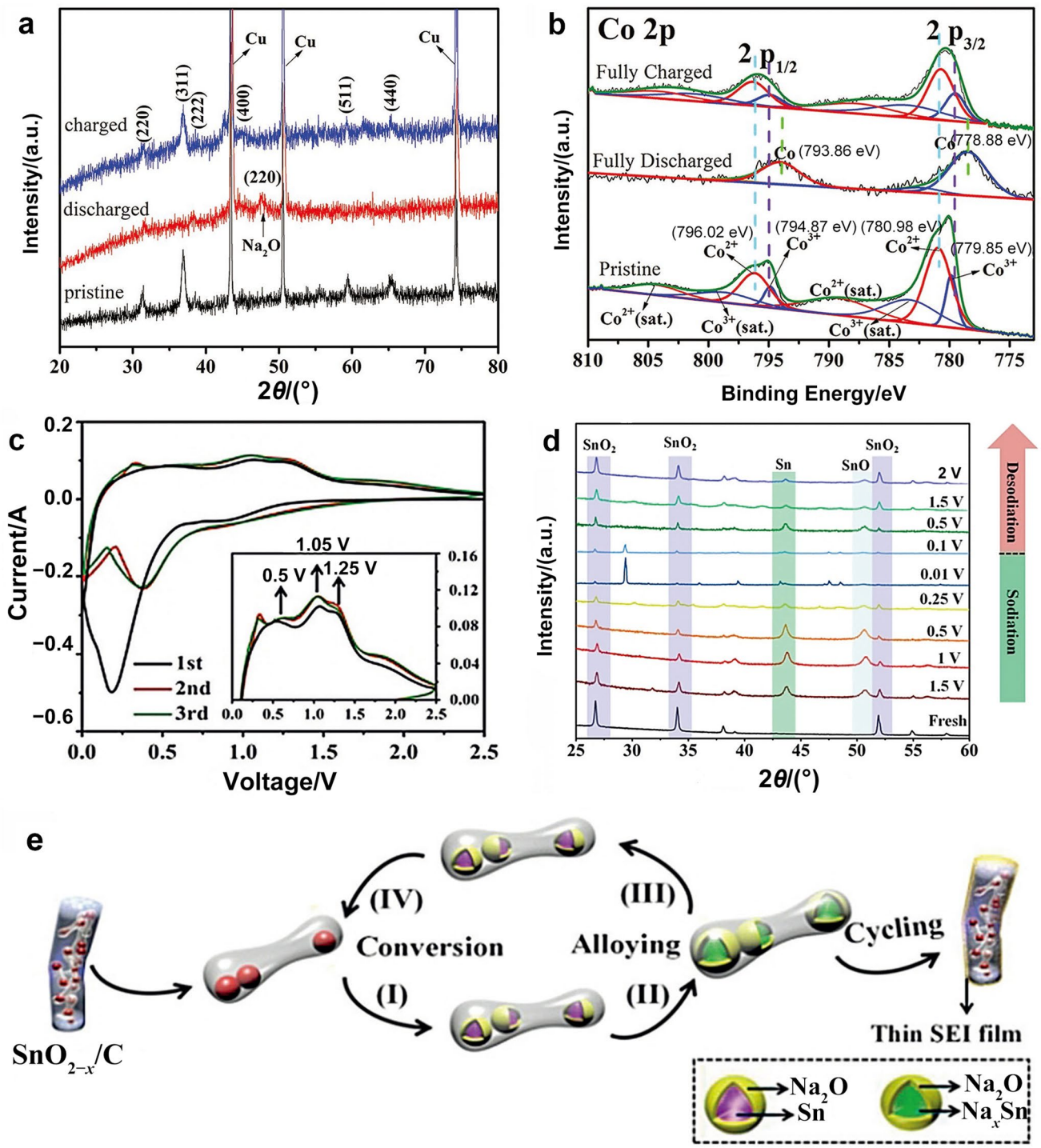

Fig. 23 **a** Ex situ XRD patterns, and **b** Co 2p XPS spectra of the R-Co_3O_4/C hybrid hollow sphere anode material at pristine, charged and discharged states. Adapted with permission from Ref. [120]. Copyright 2018 Wiley–VCH. **c** CV curves of the first three cycles for the SnO_{2-x}/C anode material. **d** Ex situ XRD patterns of the SnO_{2-x}/C anode material at the 20th cycle at different states. **e** Diagram of the SnO_{2-x}/C anode material charges during the charge/discharge process. Adapted with permission from Ref. [125]. Copyright©2018, Wiley–VCH

method and microwave method. In the diffusion method, the reactive substances are transported in a solvent or gel, whereas crystal growth and nucleation occur at interfacial points. There are two modes of diffusion. First, the diffusion of the solvent liquid occurs where the densities of the two solvents are different, accompanied by crystal growth at the interface. Second, the reactive substances gradually diffuse past the physical barrier [174]. In the solvothermal synthesis of MOFs, metal salts and organic ligands are dissolved in a solvent and react at specific temperatures. This method will result in rapid crystallization, thus resulting in crystals with higher purity and surface area. Up to now, the synthesis of MOFs by the solvothermal method has been extensively reported in previous works. The mixture of $Zn(NO_3)_2{\cdot}6H_2O$ and 1,4-phenyl dicarboxylic acid (H_2BDC) was dissolved in dimethylformamide (DMF) and then transferred to a reaction reactor at 373 K for 24 h to synthesize MOF-5. The synthesized MOF-5 had a high crystallinity and the crystallinity of MOF-5 can be changed by adjusting the ratio of DMF/H_2BDC [175]. Compared with the diffusion method and the solvothermal method, the ultrasonic method is a method with mild synthesis conditions, easy control, environmental protection and high yield [176]. What's more, the crystallinity and size of MOFs were controlled by varying the ultrasonic time and power. MOFs synthesized by the microwave method produce uniform, clean crystals with high yield under homogenous reaction conditions [177]. In addition, nucleation of crystals can be accelerated with reduced reaction time.

3.5.2 Active Sites and Surrounding Environments of Active Sites

Active sites in MOFs consist of organic functional group sites and metal sites, which are the key factors to determine specific capacity in SIBs. Xu et al. prepared a Cd(L) MOF and Co(L) MOF (L = 5-aminoisophthalic acid) possessing the identical coordination pattern [178]. The relationship between metal ions and electrochemical properties was studied for the first time. The performance of Cd(L) MOF and Co(L) MOF were compared as anodes in SIB, Co(L) MOF delivered higher performance than Cd(L) MOF, which might be caused by the different metal ion radius. Besides, the introduction of organic functional groups as active sites (C=C, C=N, C=O, and so on) into MOFs can also further improve the specific capacity. Huang et al. designed a wave-layer 3D MOF Zn-PTCA (zinc perylene-tetracarboxylates) [179], aromatic rings activated as storage active sites for Na^+ ion because of the stretching of adjacent perylene planes, in addition, C=O groups were involved in the insertion process of Na^+. Therefore, Zn-PTCA showed a high specific capacity of 357 mAh g^{-1} at the current density of 50 mA g^{-1}. Chen and co-workers obtained an Ni-TABQ MOF (TABQ = tetraminobenzoquinone) [180]. The MOF chains were connected by hydrogen bonds to form a 2D layered structure, which provided pathways for Na^+ diffusion and electron conduction. Experiments and DFT indicated that the redox active centers were conjugated benzoid carbonyls and imines during Na^+ ion insertion and extraction process. High rate capacities of about 469.5 mAh g^{-1} at 100 mA g^{-1}, and 345.4 mAh g^{-1} at 8 A g^{-1} were achieved. What is more, if dual-active sites (both metal sites and organic functional groups sites) are involved in the Na^+ ion storage process, the specific capacity will be further increased. Wang et al. fabricated a 1D π-d conjugated coordination polymer Ni-BTA (BTA = 1,2,4,5-benzenetetramine) as anodes for SIBs [181]. The synthesized Ni-BTA showed an outstanding reversible capacity of about 500 mAh g^{-1} under 0.1 A g^{-1} with good rate performance (330 mAh g^{-1} at 10 A g^{-1}). The electrochemical performances of obtained Ni-BTA are better than most of the reported MOFs in SIBs. Our group obtained the Ni-HHT-250 electrode materials with high exposure of active sites. The Ni-HHTP-250 electrode delivered a reversible discharge capacity of 420 mAh g^{-1} at 0.1 A g^{-1} and a decent rate capacity of 200 mAh g^{-1} at 2.0 A g^{-1}. Porous structure and high exposure of active sites benefit rapid kinetics and high conductivity [182].

In addition to active sites, the surrounding environments of active sites also affect the performance of SIB anode materials, for example vacancies, specific surface area, morphology and so on. Vacancy is an important factor promoting sodium ions storage. Li and co-worker reported Co-MOF nanosheets (u-CoOHtp) with oxygen vacancies [183]. Because of the existence of unsaturated metal sites on the surface of u-CoOHtp, oxygen vacancies were generated, resulting in an unbalanced charge distribution, which can induce the formation of a local electric field, thus speeding up the diffusion rate of Na^+ ion and improving sodium ions storage performance. The obtained u-CoOHtp anode material exhibited an excellent capacity of 555 mAh g^{-1} and maintained remarkable cycling performance (371 mAh g^{-1} after 50 cycles) at the current density of 50 mA g^{-1}. Yin et al. prepared a series of Co-MA MOFs (MA = maleic acid) to study the effect of morphology on electrochemical property [184]. Compared with spherical Co-MA-2, the porous flower-like Co-MA-3 has the virtues of a more porous structure and a large specific surface area to ensure a large number of active sites and the cycling stability. At the current density of 100 mA g^{-1}, the Co-MA-3 could provide an outstanding reversible capacity of 554 mAh g^{-1} and maintain a remarkable cycling performance (460 mAh g^{-1} over 300 cycles).

In addition to the factors mentioned above, the electrical conductivity and the length of organic ligands also affect the electrochemical performance. To introduce conductive

MOFs could effectively solve the problem of poor conductivity. Bao et al. designed a 2D conductive MOF (Co-HAB) with a high electrical conductivity up to 1.57 S cm^{-1} [185]. As the SIBs anode, Co-HAB presented a high capacity of 291 mAh g^{-1} at 50 mA g^{-1} and an exceptional rate capability (152 mAh g^{-1} at 12 A g^{-1}). Zhang et al. reported a Co-bpdc MOF (H_2bpdc = 4,4-biphenyldicarboxylic acid) with a long linear ligand and investigated the Na^+ ion storage performance [186]. In comparison to the regular linear ligand H_2bdc, Co-bpdc MOF could accelerate the insertion/extraction of Na^+ ion due to the expanded molecular length of the H_2bpdc ligand. The Co-bpdc MOF provided a high capacity of 269 mAh g^{-1} at 20 mA g^{-1}.

3.5.3 Reaction Mechanism

Both organic ligands and metal ions can be potential active sites. For MOFs, there are multiple reaction mechanisms, such as conversion reaction, alloy reaction and embedding reaction in the charge–discharge process. For organic functional groups as active sites, according to ex situ XPS and Raman spectra of Ni-TABQ, the mechanism was investigated [180]. In the C 1s XPS spectrum (Fig. 24b), the peak of C=O bond disappeared after discharge to 1.0 V, and C–O bond appeared. Additionally, the obvious C=O bond signal in the O 1s spectrum was transformed into C–O–Na bond during the initial discharge state and recovered under full charge state (Fig. 24c), indicating that the redox reaction of C=O bond led to the first Na^+ ion insertion. In the N 1s spectrum (Fig. 24d), the peak intensities of the C–N bond and C=N bond barely changed from their original state when discharged to 1.0 V, and the C=N signal disappeared when discharged to 0.2 V. This indicated that C=O and C=N inserted $4Na^+$ through two continuous reduction processes during discharge. During the charging process, they were reversibly oxidized. The Raman diagram of Fig. 24e showed that the Ni–N bond was stable and the valence state of Ni did not change during the discharge and charge cycles (Fig. 24f).

For metal organic functional groups as active sites, Ni-BTA experienced a three-electron reaction during the electrochemical process [181]. FTIR, XPS and Raman spectra during the discharge/charge states confirmed the mechanism. It clearly showed from the C 1s spectrogram (Fig. 25a) that in the discharge process, the signal peak of C=N bond decreased while that of C–N increased. In the subsequent charging process, the opposite phenomenon occurred, which indicated the interconversion between the C=N and C–N groups. The ex situ XPS spectrum of N 1s (Fig. 25b) and FTIR spectra (Fig. 25c) also proved the above phenomenon. Figure 25d shows that the C=C/C–C bond did not change during the charging and discharging process (XPS and FTIR results can also prove). XANES further confirmed the presence of Ni^+ (Fig. 25e), which was manifested a transition from Ni^{2+} to Ni^+. Figure 25f shows that the Ni–N coordination bond still existed stably even if the valence state of Ni changed.

4 Influences of Electrolytes, Conductive Agents, Binders and Separators

4.1 Electrolytes

Electrolyte of SIBs can be divided into a solid electrolyte and a liquid electrolyte. The liquid electrolyte solvent mostly carbon-based electrolyte, including ethyl carbonate (EC), Propylene carbonat (PC), dimethyl carbonate (DMC), ethyl carbonate(DEC) and their mixtures, show poor rate performance and low initial CE. The solute is mainly sodium salt with a large radius anion, which is divided into inorganic sodium salt and organic sodium salt. The former includes sodium hexafluorophosphate, sodium perchlorate, etc., and the latter mainly includes sodium fluorosulfonic acid salts, sodium fluoride sulfonimide salts and so on. Solid electrolyte materials are mainly three types: inorganic solid electrolyte, polymer solid electrolyte, and composite solid electrolyte. These materials are currently faced with problems such as low room temperature conductivity and large interface impedance. So, their industrialization still needs some time.

Electrolytes have a great impact on the battery capacity. Electrolytes affect the formation of SEI films, active site, charge and discharge products, transfer resistance and so on. The influence of the electrolyte on the SEI film will directly affect the capacity of the battery. Yi et al. took hard carbon as an example to explore the influence of electrolytes [187]. The ether electrolyte showed better rate kinetics than that of the carbonate electrolyte. By distinguishing the effects of the SEI layer and the desolvation behavior, it could be concluded that the desolvation process was the rate control step of the electrode reaction process and was the main factor leading to the kinetic difference between the two electrolytes. This study provides a clear mechanism for the rapid kinetics of ether electrolytes, which will facilitate their application in SIBs. From the data in most references, sulfides and alloy materials in etheric electrolytes show superior electrochemical performance. The alloying/converting Sn-MnO@C material achieves unprecedented rate performance and cycle stability through the design of electrolytes. The interface model shows that the compatibility of electrolytes is necessary [188].

Electrolytes also have great influences on the roles of active sites. For transition metal sulfides, the electrolyte anion (ClO_4^-) will parasitically react with it to produce a poorly conductive and unstable SEI film, which

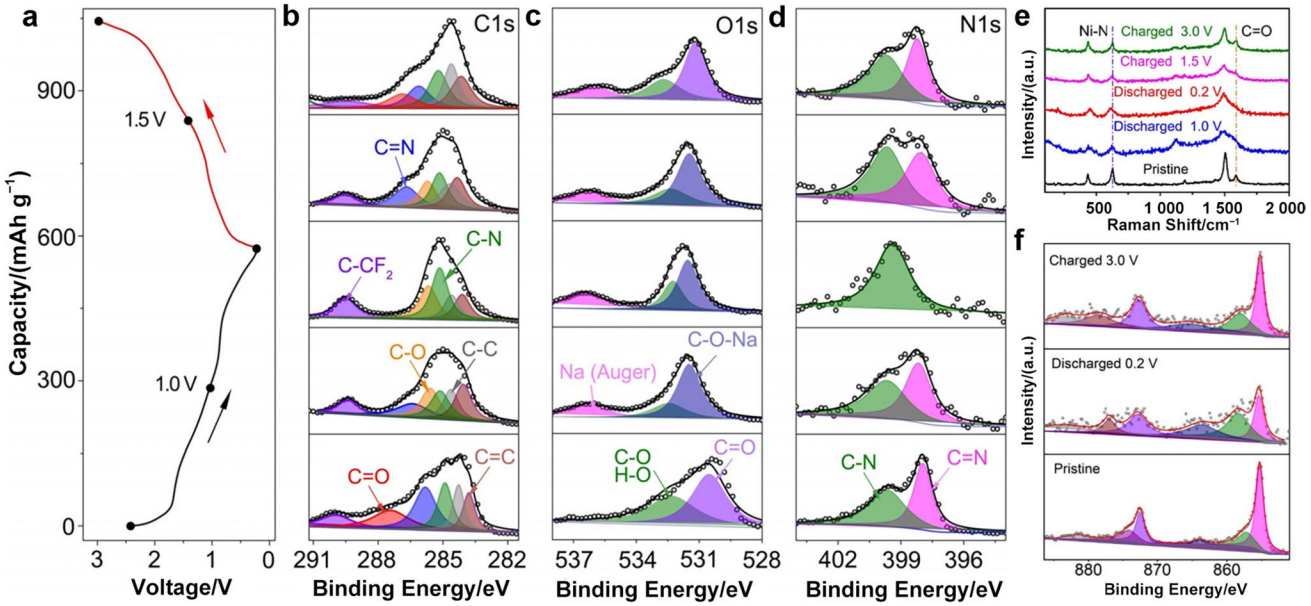

Fig. 24 **a** Discharge/charge curve of the Ni-TABQ anode at 100 mA g^{-1}. **b**–**d** Ex situ C 1s, N 1s and O 1s XPS spectra, **e** ex situ Raman spectra and **f** ex situ Ni 2p XPS spectra of the Ni-TABQ anode in the discharge and charge processes. Adapted with permission from Ref. [180]. Copyright©2020, Wiley–VCH

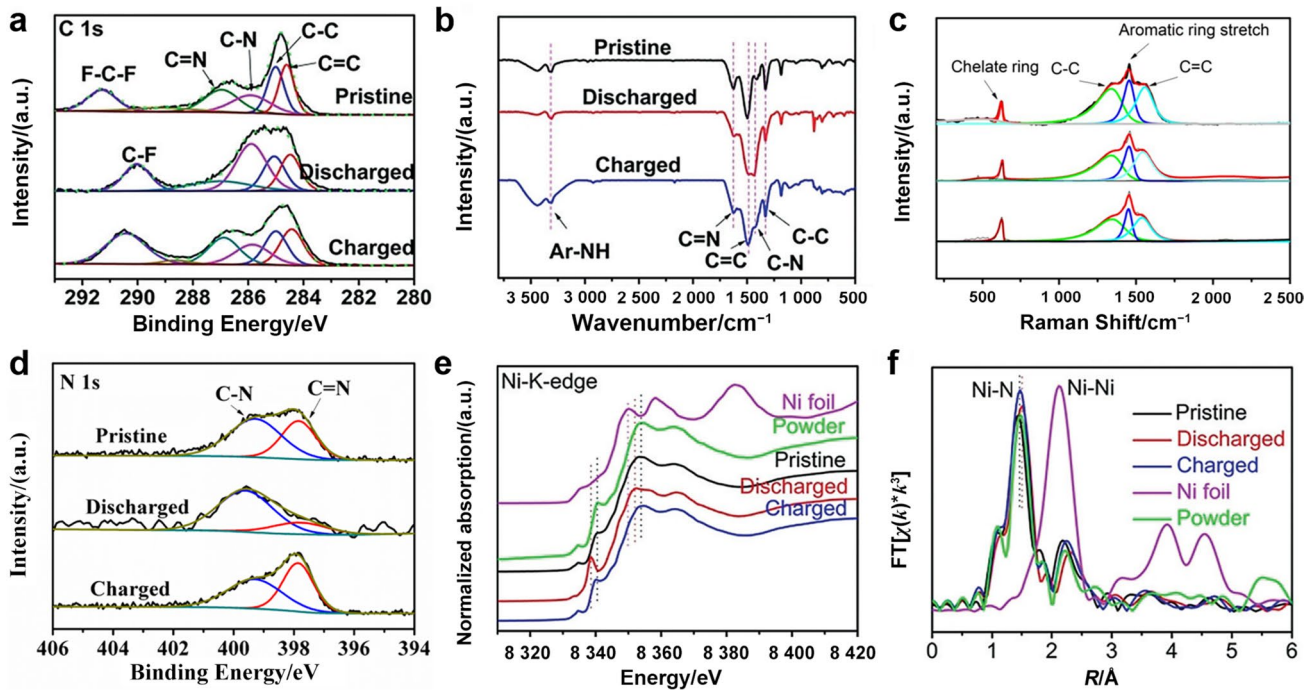

Fig. 25 **a** XPS C 1s spectra, **b** FTIR spectra, **c** ex situ Raman spectra, **d** ex situ XPS N 1s spectra, **e** Ni K-edge XANES and **f** EXAFS of the Ni-BTA anode at different states. Adapted with permission from Ref. [181]. Copyright©2019, Wiley–VCH

will corrosively convert metal sulfides into less active oxides, and the number of active sites will be greatly reduced. Yang et al. took FeS as an example to test its charge and discharge products. When the electrolyte was $NaClO_4$, the capacity of FeS rapidly attenuated after 80 cycles. Through XPS analysis, it was found that the electrode material was transformed into Fe_2O_3 with lower activity. Researchers cleverly added sodium nitrate to the electrolyte, and the charge and discharge products of FeS were detected and found that they would not be converted into Fe_2O_3, and the electrode surface would generate stable and conductive NaF and NaN_3 SEI films [189]. The type of electrolyte has a great influence on the transfer resistance, and the resistance of the ether electrolyte will be much smaller than that of the ester electrolyte. The dissolution of SEI depends on the chemical properties of the electrolyte, including solvents, salts, and additives. Jin et al. developed an advanced low solvation electrolyte (NaFSI/DMC:TFP) that inhibits SEI dissolution through a low polarity TFP solvent, a solvation structure of a small amount of free solvent, and regulation of SEI components through salt decomposition with low solubility in the electrolyte. The high ionic conductivity of the NaFSI/DMC:TFP electrolyte and the low impedance SEI layer formed by the electrode material in the electrolyte make the battery have good rate performance and long cycle performance. In addition, NaFSI/DMC:TFP electrolytes are non-flammable, enabling high safety [190].

4.2 Conductive Agents

The role of conductive agent is to reduce the contact resistance between the electrodes and current collector, thus decreasing the internal resistance of the SIBs. The conductive agent can form a conductive network between the active substances, increase electron mobility and collect microcurrent, and meanwhile, help enhance charge–discharge performance and cycling performance [191]. The conductive agent is usually conductive carbon black material. The large specific surface area, small particle size distribution and close packing of carbon black particles are helpful to the tight contact between the particles, forming the highly conductive framework in the electrode. Carbon black not only has point-to-point contact with active substances, but also can function as liquid absorption and liquid retention in the battery. Common conductive conductors include Super-P, AB and KB. Among them, KB has the best conductivity, but its dispersion is poor, which makes it easy to for the copper foil material to fall off. SP is a kind of conductive carbon black obtained via furnace method. It is composed of primary particles (primary structure) with a diameter of about 40 nm and aggregated into primary aggregates (secondary structure) with a diameter of 150–200 nm, and then through soft agglomeration and artificial compression and other subsequent processing. The overall shape is a grape ball chain. AB is prepared by the calcium carbide method. First, the acetylene gas is made of calcium carbide. After purification, the acetylene gas is separated from the air at ~ 1 400 °C for cracking, and then cooled and collected. In order to obtain a stable mass, the reaction temperature should be kept at about 1 800 °C. The temperature in the furnace can be controlled by the water cooling jacket of the outer cylinder of the reactor. Compared with furnace carbon black, acetylene black has a more developed crystal and secondary structure, so it has better conductivity and liquid absorption, but the power cost is very high. KB is a kind of high purity branched chain conductive carbon black prepared by a special production process. Compared with ordinary conductive carbon black, KB can achieve high conductivity with very low addition amount. Compared with other conductive carbon black, KB has a unique branched chain shape, with a more conductive contact points and more conductive pathways formed by branched chains. So, KB can acquire very high conductivity with very little addition. Owing to the ultra-high conductivity of KB, its amount of addition is much less than that of other conductive carbon black, so it can be filled with more active substances, which greatly improve the capacity and current density of the battery and extend the service time of the battery with high stability. The branched chain form of KB has sufficient contact with the active substance and does not lose contact due to a change of clearance. The resistance of the battery does not increase because of volume expansion and contraction during charging and discharging. The conductive agent also has a great effect on the resistance, of which the resistance of KB is the smallest. When KB is used as a conductive agent, it helps to improve the conductivity of the electrode material, so that the electrode material can play a full role in improving its reversible capacity and CE.

4.3 Binders

The strong interaction between the binder and the active material also plays a crucial role in the electrochemical performance. Good affinity between the binder and the active material can improve the mechanical stability of the active material and help maintain the electrode structure during its cycle so as to retain more active sites. At present, PVDF, CMC, PAA, and PVA are widely used as SIB binders. Polymeric binders with specific carboxyl groups can inhibit the reduction reaction of electrolytes, such as PAA and CMC. They have electrochemical properties better than those of PVDF binders. PVDF is one kind of semi-crystalline polymer with relatively high crystallinity

and high crystallization melting temperature. Therefore, at the usual battery temperature, it is difficult for molecules with an electrolytic liquid to flow due to the crystallinity of PVDF; thereby, the charge and discharge load increases. The shrinkage rate of PVDF is relatively different from that of the collector, and the film containing active substances will be separated from the collector when the drying rate of the battery is not appropriate. The introduction of the polar groups of PVDF copolymer can remarkably enhance the bonding ability of the binder, avoid electrode shedding, significantly reduce the composition of the binder, grant the battery higher energy density, smaller internal resistance, and provide better power performance, higher energy density and longer cycle time. However, PVDF lacks the chemical bond to bond with the electroactive material, resulting in limited bond strength and insufficient mechanical stability. CMCs are cellulose carboxymethylated derivatives, usually by natural cellulose and caustic soda and a chloroacetic acid reaction. The molecular weight of CMC is from thousands to millions. Adding CMC in the preparation of electrode paste can improve slurry viscosity and prevent precipitation of the slurry. CMC in an aqueous solution will decompose sodium ions and anions, the viscosity of the CMC glue will decrease with the increase in temperature, easy moisture absorption and poor elasticity. PAA is a linear long chain structure with plenty of carboxyl groups. Carboxyl groups enable the formation of hydrogen bonds between molecular chains of PAA itself, resulting in a certain degree of crosslinking. Therefore, the bonding performance is good. PVA is a common water-soluble polymer compound. Its molecular chain holds plenty of hydroxyl groups, which can produce hydrogen bonds on the surface of carbon anode materials and has good bonding property. SA is rich in carboxyl and hydroxyl groups, which can promote the formation of hydrogen bonds under protonation and play an important role in maintaining electrode stability. SA not only makes the active particles and conductive agents evenly distributed, effectively alleviates the agglomeration of the active materials, but also facilitates the penetration of electrolytes [192].

Gu et al. compared the effects of four different binders (SA, CMC, PVDF and LA133) on the electrochemical properties of $Na_3V_2(PO_4)_2O_2F$ as a cathode electrode material for SIBs. SA has high water solubility, abundant carboxyl and hydroxyl groups, and high adhesion and cohesion, so the active material and carbon black are evenly distributed in the electrode and have good integrity, so the electrode material shows the best electrochemical performance with SA binder. Luo et al. found that the SA binder could fill the cracks of the electrode during the volume expansion of the electrode material, confirming that self-healing can occur between the hydroxy-rich binder and the oxygen-rich active material [193]. Cross-linking binders are expected to have a variety of functions, including a superb binding affinity for collectors and active particles, adequate mechanical properties to withstand particle deformation, outstanding electrochemical stability within the operating voltage window, and good wetting ability for electrolytes [194]. Although the binder has excellent electrochemical stability and close interaction with the active particles, it has interchain interaction and insufficient linear structure to withstand the volume expansion and contraction of the active material upon the continuous cycling. For SIBs, the large mass and size of Na^+ always lead to poor electrochemical stability and large volume changes, particularly in alloy-type anode materials. Yao et al. significantly improved electrochemical performance through the cross-linking of polyacrylic acid with glycerol (PAA-Gly), the molecular engineering of polymer binders, which eliminated active protons from PAA, enhanced mechanical properties, and facilitated electrolyte diffusion. The advantages of PAAs are molecular weight control and single functional groups, namely carboxyl; glycerol (GLY) are used to bind PAAs through cross-linking, improving mechanical properties, increasing electrolyte compatibility, and decreasing side reactions produced by protons in PAAs [191]. Xia et al. designed a sodium alginate/polyethylene (SA/PEO) oxide binder with a large number of hydrophilic functional groups by esterification reaction. It forms a uniform passivation film on the electrode surface through hydrogen bonding, further inhibits the decomposition of the electrolyte and the continuous formation of the SEI film, and can accelerate the migration rate of Na^+ [195]. As a result, electrochemical performance is effectively enhanced, particularly in terms of cycle life and CE.

4.4 Separators

Separators can separate the cathodes and anodes, avoid short circuits and allow the transport of ion. Although the separator is not the electrochemical active site to provide specific capacity, it has an important impact on the specific capacity and cycle stability of SIBs. Glass fiber filter paper, polyolefin separators are usually used. Glass fiber filter paper has superior thermal stability, high porosity and ionic conductivity. However, its large thickness and poor mechanical limit its further industrial application. For polyolefin separators [mainly including polyethylene (PE), polypropylene (PP) and their analogues], they have excellent mechanical strength and chemical stability, but their wettability in the SIBs electrolytes are poor. So, the polyolefin separators are not been directly used in SIBs. The eligible separator must possess the following properties: (1) superior thermostability at high temperature and electrochemical stability; (2) the ability to avoid the formation and growth of dendrites; (3) excellent mechanical stability; (4) decent wettability in liquid electrolytes; (5) suitable thickness and pores.

In addition to traditional separators, more and more new types of separators have been developed. Cellulose-based separators have the advantages of environmental friendliness, superior thermal stability and degradability, which make them attractive for SIB separators. Abundant hydroxyl functional groups of natural cellulose result in a strong intermolecular force, which reduces the pore sizes of separator and further influences the transport of Na^+ ion. In order to accelerate the transport of Na^+ ion, Wu's group reported a "pore-hopping" ion transport in cellulose-based separators with excellent electrochemical performance for SIBs [196]. Solid polymer electrolyte (SPE) poly(propylene carbonate) (PPC) was used to modify the cellulose paper (CP). DFT results indicated that the PPC could faciliate the transport of Na^+ ion because of the occurrence of carbonyl group. The Na^+ ion could pass through the large and medium pores of CP, but it couldn't pass through small pores of CP. When THE Na^+ ion encountered small pore, the Na^+ ion would first move along the PPC chain until it encountered large and medium pore. The "pore-hopping" mechanism made the CP@PPC separator have high ionic conductivity and high ionic transport numbers, which resulted in superior cycle stability and fast charging in half and full cells.

Developing separators to avoid dendrite penetration is also very important. Chen's group reported an ultrathin honeycomb-structure exterior-nonporous separator with superior thermostability and mechanical robustness [197]. It was constructed by polyethersulfone (PES) and polyvinylidene fluoride-hexafluoropropylene (PVDF-HFP). The polar separator could immobilize free solvent molecules to form highly aggregated solvation structure and robust inorganic-rich interphase. Thus, the nonporous could suppress Na dendrite and prevent dendrite penetration. There are also other strategies to optimize separators, such as coating, doping, etc.

5 Conclusions and Perspectives

5.1 Summary

In conclusion, the review summarized the research progress of SIBs including the electrodes, electrolytes, conductive agents, binders and separators in the last five years. For the cathode materials and anode materials, their design strategies and synthesis, reactive active site and reaction mechanism at molecular and atomic scales, and the latest characterization methods are reviewed. In this review, the problems faced by cathode materials and anode materials as well as optimization strategies are reviewed. In addition, the common kinds of electrolytes, conductive agents, binders and separators, the conditions of their use and their influences on the electrochemical performance are summarized.

The electrochemical performance of SIBs is primarily influenced by the electrode materials and electrolytes. In order to meet the requirement of development, some new electrode materials and electrolytes have been raised (e.g., high-entropy electrode materials, MOFs electrode materials, solid polymer electrolytes and ionic liquid electrolytes). Meanwhile, many optimized and improved strategies (ion doping, coating, micro-nanoengineering, structural design, etc.) are effective to enhance the electrochemical performance. In addition, more and more advanced in situ characterization methods are applied to investigate the reaction mechanism.

5.2 Challenges

SIBs have attracted increasingly attention in the new secondary batteries field due to the low cost and abundant sodium resources. However, low energy/power density, rate performance and cyclic stability are still the main obstacles for further development of SIBs. There are some challenges for further developing SIBs.

1. The low energy/power density, phase transition, volume change and low electronic conductivity of electrode materials restrict their further development [198–203]. The layer transition oxides usually occur in phase transition during the charge/discharge process, leading to the structural collapse [198–200]. The polyanionic compounds have the problem of low electron conductivity and volume energy [201]. The organic compounds possess low electronic conductivity and easy dissolution in organic electrolytes [202]. Sodium metal anode possesses high capacity and low redox potential. However, uneven sodium ion movement in bulk sodium anodes results in local deposition/dissolution of sodium through high speed plating/stripping behavior, followed by serious dendrite growth and loose accumulation.
2. The narrow voltage window, the high flammability and volatility and the low thermal stability are the main problems for the organic electrolytes. Presently, the organic electrolytes are one of the most commonly used electrolytes. The narrow voltage window can result in the low energy/power density. The high flammability and volatility, and the low thermal stability can cause safety problems.
3. There is also a lack of in-depth study of reaction mechanism and failure mechanism analysis. The mechanism study usually needs advanced in situ characterization method. At present, the advanced in situ characterization techniques are still inadequate. The unclear mechanism and failure mechanism can hinder the development of SIBs.

5.3 Future Research Directions

The large specific energy, long cyclic life, good rate performance, fast charging capacity, high safety and low cost SIBs are the goals of people to pursue. In order to develop SIBs with high performance, the optimize strategies and development directions are as follows.

(i) For cathode materials, it is necessary to develop materials with high specific capacity, high redox potential, decent structural stability, fair electron and ionic conductivity. Cheap and rich resources, and environmental-friendliness for cathode materials are also necessary. It is an effective way to improve the specific energy with stable structure by doping and surface modification. In addition, in order to reduce costs and environmental pollution, the development of cobalt-free cathode is becoming a trend.

(ii) For anode materials, it is necessary to develop high energy density and high first CE anode materials without serious voltage lag. The first CE can be improved by the artificial SEI film or the presodiation to inhibit the occurrence of the side reactions. By adopting the strategies of constructing carbon-based nanocomposites [204], coating, micro-/nanoengineering and structural design, the reaction kinetics, and the reversibility of the materials can be improved, so as to alleviate the problem of voltage lag.

(iii) For the electrolytes, it is necessary to develop wide voltage windows and wide temperature ranges electrolytes. By optimizing electrolyte components and designing additive functional molecules, the electrochemical window and temperature ranges of electrolyte can be widened to construct high-voltage SIBs.

(iv) The in-depth study of reaction mechanisms combined with theoretical calculation and advanced in situ characterization method. A clear reaction mechanism at atomic or molecular level is of great help to promote the overall performance of SIBs. With the development of modern in situ characterization techniques, it has become a trend to study the charge and discharge mechanism with advanced in situ characterization methods. In addition, the theoretical calculation is also a powerful tool to study reaction mechanism. The binding energy, adsorption energy and migration energy barrier, etc. can be obtained from the theoretical calculation, which are very helpful to explain the reaction mechanism.

(v) Developing new electrode materials and electrolytes. In order to meet the demands of high safety and high energy density and achieve diversity of materials, developing new electrode materials and electrolytes is necessary. Recently, the high-entropy compounds have become a research hotspot. The high-entropy compounds show some specific properties. The increased entropy enhances structural stability, heat/air stability and electronic conductivity. Additionally, the inorganic–organic hybrid materials are hopeful electrode materials for SIBs. They can provide multiple active sites. For electrolytes, solid polymer electrolytes and ionic liquid electrolytes have gained close attention. Ionic liquid electrolytes are regarded as the next generation of sodium ionic electrolytes.

Acknowledgements This work was financially supported by the National Natural Science Foundation of China (Grant Nos. 22305071, 52072114 and 52271176), the 111 Project (Grant No. D17007), Henan Center for Outstanding Overseas Scientists (Grant No. GZS2022017), Henan Province Key Research and Development Project (Grant No. 231111520500), the Natural Science Foundation of Henan Province (Grant No. 222300420206), China Postdoctoral Science Foudation (Grant No. 2022M721049).

Declarations

Conflicts of interest Jiujun Zhang is an editor-in-chief for *Electrochemical Energy Reviews* and was not involved in the editorial review or the decision to publish this article. All authors declare that there are no competing interests.

References

1. Pomerantseva, E., Bonaccorso, F., Feng, X.L., et al.: Energy storage: the future enabled by nanomaterials. Science **366**, 969 (2019). https://doi.org/10.1126/science.aan8285
2. Li, W.X., Guo, Z.H., Yang, J., et al.: Advanced strategies for stabilizing single-atom catalysts for energy storage and conversion. Electrochem. Energy Rev. **5**, 9 (2022). https://doi.org/10.1007/s41918-022-00169-z
3. Chen, Y.Q., Zhang, J.R., Yang, L.J., et al.: Recent advances in non-precious metal–nitrogen–carbon single-site catalysts for CO_2 electroreduction reaction to CO. Electrochem. Energy Rev. **5**, 11 (2022). https://doi.org/10.1007/s41918-022-00156-4
4. Liang, Y.L., Dong, H., Aurbach, D., et al.: Current status and future directions of multivalent metal-ion batteries. Nat. Energy **5**, 646–656 (2020). https://doi.org/10.1038/s41560-020-0655-0
5. Wu, F., Liu, M.Q., Li, Y., et al.: High-mass-loading electrodes for advanced secondary batteries and supercapacitors. Electrochem. Energy Rev. **4**, 382–446 (2021). https://doi.org/10.1007/s41918-020-00093-0

6. Nayak, P.K., Yang, L.T., Brehm, W., et al.: From lithium-ion to sodium-ion batteries: advantages, challenges, and surprises. Angew. Chem. Int. Ed. **57**, 102–120 (2018). https://doi.org/10.1002/anie.201703772
7. Zhou, Q.B., Wang, L.L., Li, W.Y., et al.: Sodium superionic conductors (NASICONs) as cathode materials for sodium-ion batteries. Electrochem. Energy Rev. **4**, 793–823 (2021). https://doi.org/10.1007/s41918-021-00120-8
8. Vaalma, C., Buchholz, D., Weil, M., et al.: A cost and resource analysis of sodium-ion batteries. Nat. Rev. Mater. **3**, 1–11 (2018). https://doi.org/10.1038/natrevmats.2018.13
9. Fang, Y.J., Chen, Z.X., Ai, X.P., et al.: Recent developments in cathode materials for Na ion batteries. Acta Phys. Chim. Sin. **33**, 211–241 (2017). https://doi.org/10.3866/pku.whxb201610111
10. Yang, X.M., Rogach, A.L.: Anodes and sodium-free cathodes in sodium ion batteries. Adv. Energy Mater. **10**, 2000288 (2020). https://doi.org/10.1002/aenm.202000288
11. Lee, J.M., Singh, G., Cha, W., et al.: Recent advances in developing hybrid materials for sodium-ion battery anodes. ACS Energy Lett. **5**, 1939–1966 (2020). https://doi.org/10.1021/acsenergylett.0c00973
12. Liu, Y., Li, W., Xia, Y.Y.: Recent progress in polyanionic anode materials for Li (Na)-ion batteries. Electrochem. Energy Rev. **4**, 447–472 (2021). https://doi.org/10.1007/s41918-021-00095-6
13. Braconnier, J.J., Delmas, C., Fouassier, C., et al.: Comportement electrochimique des phases Na_xCoO_2. Mater. Res. Bull. **15**, 1797–1804 (1980). https://doi.org/10.1016/0025-5408(80)90199-3
14. Delmas, C., Fouassier, C., Hagenmuller, P.: Structural classification and properties of the layered oxides. Phys. B + C **99**, 81–85 (1980). https://doi.org/10.1016/0378-4363(80)90214-4
15. Or, T., Gourley, S.W.D., Kaliyappan, K., et al.: Recent progress in surface coatings for sodium-ion battery electrode materials. Electrochem. Energy Rev. **5**, 1–54 (2022). https://doi.org/10.1007/s41918-022-00137-7
16. Yang, L.F., Li, X., Liu, J., et al.: Lithium-doping stabilized high-performance P2-$Na_{0.66}Li_{0.18}Fe_{0.12}Mn_{0.7}O_2$ cathode for sodium ion batteries. J. Am. Chem. Soc. **141**, 6680–6689 (2019). https://doi.org/10.1021/jacs.9b01855
17. Sun, C.C., Li, S.W., Bai, M., et al.: Construction of the $Na_{0.92}Li_{0.40}Ni_{0.73}Mn_{0.24}Co_{0.12}O_2$ sodium-ion cathode with balanced high-power/energy-densities. Energy Storage Mater. **27**, 252–260 (2020). https://doi.org/10.1016/j.ensm.2020.02.007
18. Yang, L.T., del Amo, J.M.L., Shadike, Z., et al.: A Co- and Ni-free P2/O3 biphasic lithium stabilized layered oxide for sodium-ion batteries and its cycling behavior. Adv. Funct. Mater. **30**, 2003364 (2020). https://doi.org/10.1002/adfm.202003364
19. Peng, B., Sun, Z.H., Zhao, L.P., et al.: Dual-manipulation on P2-$Na_{0.67}Ni_{0.33}Mn_{0.67}O_2$ layered cathode toward sodium-ion full cell with record operating voltage beyond 35 V. Energy Storage Mater. **35**, 620–629 (2021). https://doi.org/10.1016/j.ensm.2020.11.037
20. Shen, Q.Y., Zhao, X.D., Liu, Y.C., et al.: Dual-strategy of cation-doping and nanoengineering enables fast and stable sodium-ion storage in a novel Fe/Mn-based layered oxide cathode. Adv. Sci. **7**, 2002199 (2020). https://doi.org/10.1002/advs.202002199
21. Xiao, Y., Zhu, Y.F., Xiang, W., et al.: Deciphering an abnormal layered-tunnel heterostructure induced by chemical substitution for the sodium oxide cathode. Angew. Chem. Int. Ed. **59**, 1491–1495 (2020). https://doi.org/10.1002/anie.201912101
22. Xiao, Y., Wang, P.F., Yin, Y.X., et al.: Exposing{010}active facets by multiple-layer oriented stacking nanosheets for high-performance capacitive sodium-ion oxide cathode. Adv. Mater. **30**, 1803765 (2018). https://doi.org/10.1002/adma.201803765
23. Yu, Y., Ning, D., Li, Q.Y., et al.: Revealing the anionic redox chemistry in O_3^- type layered oxide cathode for sodium-ion batteries. Energy Storage Mater. **38**, 130–140 (2021). https://doi.org/10.1016/j.ensm.2021.03.004
24. You, Y., Xin, S., Asl, H.Y., et al.: Insights into the improved high-voltage performance of Li-incorporated layered oxide cathodes for sodium-ion batteries. Chem **4**, 2124–2139 (2018). https://doi.org/10.1016/j.chempr.2018.05.018
25. Lin, C.C., Liu, H.Y., Kang, J.W., et al.: In-situ X-ray studies of high-entropy layered oxide cathode for sodium-ion batteries. Energy Storage Mater. **51**, 159–171 (2022). https://doi.org/10.1016/j.ensm.2022.06.035
26. Park, S.J., Lee, J., Ko, I.H., et al.: Thermodynamics and Na kinetics in P2-type oxygen redox Mn–Ni binary layered oxides manipulated via Li substitution. Energy Storage Mater. **42**, 97–108 (2021). https://doi.org/10.1016/j.ensm.2021.07.013
27. Xiao, J., Gao, H., Tang, K.K., et al.: Manipulating stable layered P2-type cathode via a Co-substitution strategy for high performance sodium ion batteries. Small Methods **6**, 2101292 (2022). https://doi.org/10.1002/smtd.202101292
28. Wang, Y., Zhao, X.D., Jin, J.T., et al.: Low-cost layered oxide cathode involving cationic and anionic redox with a complete solid-solution sodium-storage behavior. Energy Storage Mater. **47**, 44–50 (2022). https://doi.org/10.1016/j.ensm.2022.01.047
29. Xi, K.Y., Chu, S.F., Zhang, X.Y., et al.: A high-performance layered Cr-based cathode for sodium-ion batteries. Nano Energy **67**, 104215 (2020). https://doi.org/10.1016/j.nanoen.2019.104215
30. Wang, J.E., Han, W.H., Chang, K.J., et al.: New insight into Na intercalation with Li substitution on alkali site and high performance of O_3^- type layered cathode material for sodium ion batteries. J. Mater. Chem. A **6**, 22731–22740 (2018). https://doi.org/10.1039/C8TA06159A
31. Ji, H.C., Zhai, J.J., Chen, G.J., et al.: Surface engineering suppresses the failure of biphasic sodium layered cathode for high performance sodium-ion batteries. Adv. Funct. Mater. **32**, 2109319 (2022). https://doi.org/10.1002/adfm.202109319
32. Chen, X.L., Song, J.P., Li, J.S., et al.: A P2/P3 composite-layered cathode material with low-voltage decay for sodium-ion batteries. J. Appl. Electrochem. **51**, 619–627 (2021). https://doi.org/10.1007/s10800-020-01522-0
33. Paidi, A.K., Park, W.B., Ramakrishnan, P., et al.: Unravelling the nature of the intrinsic complex structure of binary-phase Na-layered oxides. Adv. Mater. **34**, 2202137 (2022). https://doi.org/10.1002/adma.202202137
34. Deng, C., Zhang, S., Wang, H.F., et al.: "Bubble-in-nanorod" hierarchical hybrid fiber: a highly-efficient design for pyrophosphate-based freestanding cathodes towards fast sodium/lithium intercalation. Nano Energy **49**, 419–433 (2018). https://doi.org/10.1016/j.nanoen.2018.05.008
35. Wang, J.J., Kang, J.Z., Gu, Z.Y., et al.: Localized electron density redistribution in fluorophosphate cathode: Dangling anion regulation and enhanced Na-ion diffusivity for sodium-ion batteries. Adv. Funct. Mater. **32**, 2109694 (2022). https://doi.org/10.1002/adfm.202109694
36. Zhu, J., Deng, D.: Wet-chemical synthesis of phase-pure FeOF nanorods as high-capacity cathodes for sodium-ion batteries. Angew. Chem. Int. Ed. **54**, 3079–3083 (2015). https://doi.org/10.1002/anie.201410572
37. Zhang, W., Wu, Y.L., Xu, Z.M., et al.: Rationally designed sodium chromium vanadium phosphate cathodes with multi-electron reaction for fast-charging sodium-ion batteries. Adv. Energy Mater. **12**, 2201065 (2022). https://doi.org/10.1002/aenm.202201065
38. Wu, M.G., Ni, W., Hu, J., et al.: NASICON-structured $NaTi_2(PO_4)_3$ for sustainable energy storage. Nano Micro Lett. **11**, 44 (2019). https://doi.org/10.1007/s40820-019-0273-1
39. Geng, Y., Zhang, T., Xu, T.T., et al.: Homogeneous hybridization of NASICON-type cathode for enhanced sodium-ion storage.

Energy Storage Mater. **49**, 67–76 (2022). https://doi.org/10.1016/j.ensm.2022.03.044
40. Chen, R.Y., Butenko, D.S., Li, S.L., et al.: Effects of low doping on the improvement of cathode materials $Na_{3+x}V_{2-x}M_x(PO_4)_3$ ($M = Co^{2+}$, Cu^{2+}; $x = 0.01$–0.05) for SIBs. J. Mater. Chem. A **9**, 17380–17389 (2021). https://doi.org/10.1039/d1ta05000a
41. Drozhzhin, O.A., Tertov, I.V., Alekseeva, A.M., et al.: β-$NaVP_2O_7$ as a superior electrode material for Na-ion batteries. Chem. Mater. **31**, 7463–7469 (2019). https://doi.org/10.1021/acs.chemmater.9b02124
42. Song, T.Y., Yao, W.J., Kiadkhunthod, P., et al.: A low-cost and environmentally friendly mixed polyanionic cathode for sodium-ion storage. Angew. Chem. Int. Ed. **59**, 740–745 (2020). https://doi.org/10.1002/anie.201912272
43. Hadouchi, M., Yaqoob, N., Kaghazchi, P., et al.: Fast sodium intercalation in $Na_{3.41}£_{0.59}FeV(PO_4)_3$: a novel sodium-deficient NASICON cathode for sodium-ion batteries. Energy Storage Mater. **35**, 192–202 (2021). https://doi.org/10.1016/j.ensm.2020.11.010
44. Zhang, Z.Z., Du, Y.C., Wang, Q.C., et al.: A yolk–shell-structured $FePO_4$ cathode for high-rate and long-cycling sodium-ion batteries. Angew. Chem. Int. Ed. **59**, 17504–17510 (2020). https://doi.org/10.1002/anie.202008318
45. Song, W.X., Ji, X.B., Wu, Z.P., et al.: First exploration of Na-ion migration pathways in the NASICON structure $Na_3V_2(PO_4)_3$. J. Mater. Chem. A **2**, 5358–5362 (2014). https://doi.org/10.1039/C4TA00230J
46. Rajagopalan, R., Chen, B., Zhang, Z.C., et al.: Improved reversibility of Fe^{3+}/Fe^{4+} redox couple in sodium super ion conductor type $Na_3Fe_2(PO4)_3$ for sodium-ion batteries. Adv. Mater. **29**, 1605694 (2017). https://doi.org/10.1002/adma.201605694
47. Zhang, J., Liu, Y.C., Zhao, X.D., et al.: A novel NASICON-type $Na_4MnCr(PO4)_3$ demonstrating the energy density record of phosphate cathodes for sodium-ion batteries. Adv. Mater. **32**, 1906348 (2020). https://doi.org/10.1002/adma.201906348
48. Gu, Z.Y., Guo, J.Z., Cao, J.M., et al.: An advanced high-entropy fluorophosphate cathode for sodium-ion batteries with increased working voltage and energy density. Adv. Mater. **34**, 2110108 (2022). https://doi.org/10.1002/adma.202110108
49. Li, H.X., Zhang, Z.A., Xu, M., et al.: Triclinic off-stoichiometric $Na_{3.12}Mn_{2.44}(P_2O_7)_2$/C cathode materials for high-energy/power sodium-ion batteries. ACS Appl. Mater. Interfaces **10**, 24564–24572 (2018). https://doi.org/10.1021/acsami.8b07577
50. Zhan, R.M., Zhang, Y.Q., Chen, H., et al.: High-rate and long-life sodium-ion batteries based on sponge-like three-dimensional porous Na-rich ferric pyrophosphate cathode material. ACS Appl. Mater. Interfaces **11**, 5107–5113 (2019). https://doi.org/10.1021/acsami.8b19874
51. Shen, B.L., Xu, M.W., Niu, Y.B., et al.: Sodium-rich ferric pyrophosphate cathode for stationary room-temperature sodium-ion batteries. ACS Appl. Mater. Interfaces **10**, 502–508 (2018). https://doi.org/10.1021/acsami.7b13516
52. Li, S.Y., Song, X.S., Kuai, X.X., et al.: A nanoarchitectured $Na_6Fe_5(SO_4)_8$/CNTs cathode for building a low-cost 36 V sodium-ion full battery with superior sodium storage. J. Mater. Chem. A **7**, 14656–14669 (2019). https://doi.org/10.1039/c9ta03089a
53. Yao, G., Zhang, X.X., Yan, Y.L., et al.: Facile synthesis of hierarchical $Na_2Fe(SO_4)_2$@rGO/C as high-voltage cathode for energy density-enhanced sodium-ion batteries. J. Energy Chem. **50**, 387–394 (2020). https://doi.org/10.1016/j.jechem.2020.03.047
54. Peng, J., Gao, Y., Zhang, H., et al.: Ball milling solid-state synthesis of highly crystalline Prussian blue analogue $Na_{2-x}MnFe(CN)_6$ cathodes for all-climate sodium-ion batteries. Angew. Chem. Int. Ed. **61**, e202205867 (2022). https://doi.org/10.1002/anie.202205867
55. Wan, P., Xie, H., Zhang, N., et al.: Stepwise hollow Prussian blue nanoframes/carbon nanotubes composite film as ultrahigh rate sodium ion cathode. Adv. Funct. Mater. **30**, 2002624 (2020). https://doi.org/10.1002/adfm.202002624
56. Tang, Y., Li, W., Feng, P.Y., et al.: High-performance Manganese hexacyanoferrate with cubic structure as superior cathode material for sodium-ion batteries. Adv. Funct. Mater. **30**, 1908754 (2020). https://doi.org/10.1002/adfm.201908754
57. Liu, Y.T., Yao, Z.Y., Vanaphuti, P., et al.: Stable fast-charging sodium-ion batteries achieved by a carbomethoxy-modified disodium organic material. Cell Rep. Phys. Sci. **4**, 101240 (2023). https://doi.org/10.1016/j.xcrp.2022.101240
58. Thangavel, R., Moorthy, M., Ganesan, B.K., et al.: Nanoengineered organic electrodes for highly durable and ultrafast cycling of organic sodium-ion batteries. Small **16**, 2003688 (2020). https://doi.org/10.1002/smll.202003688
59. Zhou, G.Y., Miao, Y.E., Wei, Z.X., et al.: Bioinspired micro/nanofluidic ion transport channels for organic cathodes in high-rate and ultrastable lithium/sodium-ion batteries. Adv. Funct. Mater. **28**, 1804629 (2018). https://doi.org/10.1002/adfm.201804629
60. Zheng, S.B., Hu, J.Y., Huang, W.W.: An inorganic–organic nanocomposite calix[4]quinone (C4Q)/CMK-3 as a cathode material for high-capacity sodium batteries. Inorg. Chem. Front. **4**, 1806–1812 (2017). https://doi.org/10.1039/C7QI00453B
61. Pang, Y.R., Li, H., Zhang, S.G., et al.: Conjugated porous polyimide poly(2,6-diaminoanthraquinone) benzamide with good stability and high-performance as a cathode for sodium ion batteries. J. Mater. Chem. A **10**, 1514–1521 (2022). https://doi.org/10.1039/d1ta06384g
62. Huang, Y.S., Li, K., Liu, J.J., et al.: Three-dimensional graphene/polyimide composite-derived flexible high-performance organic cathode for rechargeable lithium and sodium batteries. J. Mater. Chem. A **5**, 2710–2716 (2017). https://doi.org/10.1039/C6TA09754E
63. Peng, J., Ou, M.Y., Yi, H.C., et al.: Defect-free-induced Na+ disordering in electrode materials. Energy Environ. Sci. **14**, 3130–3140 (2021). https://doi.org/10.1039/D1EE00087J
64. Peng, J., Zhang, B., Hua, W.B., et al.: A disordered rubik's cube-inspired framework for sodium-ion batteries with ultralong cycle lifespan. Angew. Chem. Int. Ed. **62**, e202215865 (2023). https://doi.org/10.1002/anie.202215865
65. Zou, J.C., Fan, K., Wang, X.B., et al.: A hexaazatriphenylene-based polymer as high performance anode for Li-/ Na-/ K-ion batteries. Chem. Eng. J. **460**, 141703 (2023). https://doi.org/10.1016/j.cej.2023.141703
66. Luo, C., Xu, G.L., Ji, X., et al.: Reversible redox chemistry of azo compounds for sodium-ion batteries. Angew. Chem. **130**, 2929–2933 (2018). https://doi.org/10.1002/ange.201713417
67. Chen, X., Feng, X., Ren, B., et al.: High rate and long lifespan sodium-organic batteries using pseudocapacitive porphyrin complexes-based cathode. Nano-Micro Lett. **13**, 71 (2021). https://doi.org/10.1007/s40820-021-00593-8
68. Wang, Z.Q., Zheng, X.Y., Liu, X.Y., et al.: Promoting fast Na ion transport at low temperatures for sodium metal batteries. ACS Appl. Mater. Interfaces **14**, 40985–40991 (2022). https://doi.org/10.1021/acsami.2c10915
69. Liu, P., Yi, H.T., Zheng, S.Y., et al.: Regulating deposition behavior of sodium ions for dendrite-free sodium-metal anode. Adv. Energy Mater. **11**, 2101976 (2021). https://doi.org/10.1002/aenm.202101976
70. Zhao, W.Y., Guo, M., Zuo, Z.J., et al.: Engineering sodium metal anode with sodiophilic bismuthide penetration for dendrite-free and high-rate sodium-ion battery. Engineering **11**, 87–94 (2022). https://doi.org/10.1016/j.eng.2021.08.028

71. Ni, D., Sun, W., Wang, Z.H., et al.: Heteroatom-doped mesoporous hollow carbon spheres for fast sodium storage with an ultralong cycle life. Adv. Energy Mater. **9**, 1900036 (2019). https://doi.org/10.1002/aenm.201900036
72. Chen, F.P., Di, Y.J., Su, Q., et al.: Vanadium-modified hard carbon spheres with sufficient pseudographitic domains as high-performance anode for sodium-ion batteries. Carbon Energy **5**, e191 (2023). https://doi.org/10.1002/cey2.191
73. Yu, X., Xin, L., Li, X.W., et al.: Completely crystalline carbon containing graphite-like crystal enables 99.5% initial coulombic efficiency for Na-ion batteries. Mater. Today **59**, 25–35 (2022). https://doi.org/10.1016/j.mattod.2022.07.013
74. Tao, H.W., Wang, R.X., Tang, Y., et al.: Low-valence titanium oxides synthesized by electric field control as novel conversion anodes for high performance sodium-ion batteries. J. Mater. Chem. A **9**, 10458–10465 (2021). https://doi.org/10.1039/D0TA12552K
75. Zhao, S.Q., Guo, Z.Q., Yang, J., et al.: Nanoengineering of advanced carbon materials for sodium-ion batteries. Small **17**, 2007431 (2021). https://doi.org/10.1002/smll.202007431
76. Wang, J.C., Zhao, J.H., He, X.X., et al.: Hard carbon derived from hazelnut shell with facile HCl treatment as high-initial-coulombic-efficiency anode for sodium ion batteries. Sustain. Mater. Technol. **33**, e00446 (2022). https://doi.org/10.1016/j.susmat.2022.e00446
77. Yu, C.X., Li, Y., Ren, H.X., et al.: Engineering homotype heterojunctions in hard carbon to induce stable solid electrolyte interfaces for sodium-ion batteries. Carbon Energy **5**, e220 (2023). https://doi.org/10.1002/cey2.220
78. Zhao, Y., Cong, Y., Ning, H., et al.: N, P co-doped pitch derived soft carbon nanoboxes as high-performance anodes for sodium-ion batteries. J. Alloys Compd. **918**, 165691 (2022). https://doi.org/10.1016/j.jallcom.2022.165691
79. Xu, X.D., Zeng, H.L., Han, D.Z., et al.: Nitrogen and sulfur oc-doped graphene nanosheets to improve anode materials for sodium-ion batteries. ACS Appl. Mater. Interfaces **10**, 37172–37180 (2018). https://doi.org/10.1021/acsami.8b15940
80. Chen, W.H., Chen, X.P., Qiao, R., et al.: Understanding the role of nitrogen and sulfur doping in promoting kinetics of oxygen reduction reaction and sodium ion battery performance of hollow spherical graphene. Carbon **187**, 230–240 (2022). https://doi.org/10.1016/j.carbon.2021.11.020
81. Mahmood, A., Yuan, Z.W., Sui, X., et al.: Foldable and scrollable graphene paper with tuned interlayer spacing as high areal capacity anodes for sodium-ion batteries. Energy Storage Mater. **41**, 395–403 (2021). https://doi.org/10.1016/j.ensm.2021.06.020
82. Liang, S.Z., Wang, X.Y., Qi, R.X., et al.: Bronze-phase TiO_2 as anode materials in lithium and sodium-ion batteries. Adv. Funct. Mater. **32**, 2201675 (2022). https://doi.org/10.1002/adfm.202201675
83. Liu, G.Z., Huang, M., Zhang, Z., et al.: Robust S-doped TiO_2@N, S-codoped carbon nanotube arrays as free-binder anodes for efficient sodium storage. J. Energy Chem. **53**, 175–184 (2021). https://doi.org/10.1016/j.jechem.2020.05.030
84. Lee, G.H., Kang, J.K.: Synthesis of nitrogen-doped mesoporous structures from metal–organic frameworks and their utilization enabling high performances in hybrid sodium-ion energy storages. Adv. Sci. **7**, 1902986 (2020). https://doi.org/10.1002/advs.201902986
85. Gan, Q.M., He, H.N., Zhu, Y.H., et al.: Defect-assisted selective surface phosphorus doping to enhance rate capability of titanium dioxide for sodium ion batteries. ACS Nano **13**, 9247–9258 (2019). https://doi.org/10.1021/acsnano.9b03766
86. Meng, W.J., Dang, Z.Z., Li, D.S., et al.: Interface and defect engineered titanium-base oxide heterostructures synchronizing high-rate and ultrastable sodium storage. Adv. Energy Mater. **12**, 2201531 (2022). https://doi.org/10.1002/aenm.202201531
87. Jian, Z.L., Bommier, C., Luo, L.L., et al.: Insights on the mechanism of Na-ion storage in soft carbon anode. Chem. Mater. **29**, 2314–2320 (2017). https://doi.org/10.1021/acs.chemmater.6b05474
88. Qiao, S., Zhou, Q., Ma, M., et al.: Advanced anode materials for rechargeable sodium-ion batteries. ACS Nano **17**, 11220–11252 (2023). https://doi.org/10.1021/acsnano.3c02892
89. Alvin, S., Yoon, D., Chandra, C., et al.: Revealing sodium ion storage mechanism in hard carbon. Carbon **145**, 67–81 (2019). https://doi.org/10.1016/j.carbon.2018.12.112
90. Qiu, S., Xiao, L.F., Sushko, M.L., et al.: Manipulating adsorption–insertion mechanisms in nanostructured carbon materials for high-efficiency sodium ion storage. Adv. Energy Mater. **7**, 1700403 (2017). https://doi.org/10.1002/aenm.201700403
91. Yin, X.P., Lu, Z.X., Wang, J., et al.: Enabling fast Na^+ transfer kinetics in the whole-voltage-region of hard-carbon anodes for ultrahigh-rate sodium storage. Adv. Mater. **34**, 2109282 (2022). https://doi.org/10.1002/adma.202109282
92. Zheng, S.M., Tian, Y.R., Liu, Y.X., et al.: Alloy anodes for sodium-ion batteries. Rare Met. **40**, 272–289 (2021). https://doi.org/10.1007/s12598-020-01605-z
93. Liu, J.L., Muhammad, S., Wei, Z.X., et al.: Hierarchical N-doping germanium/carbon nanofibers as anode for high-performance lithium-ion and sodium-ion batteries. Nanotechnology **31**, 015402 (2020). https://doi.org/10.1088/1361-6528/ab4404
94. Park, B., Lee, S., Han, D.-Y., et al.: Multiscale hierarchical design of bismuth-carbon anodes for ultrafast-charging sodium-ion full battery. Appl. Surf. Sci. **614**, 156188 (2023). https://doi.org/10.1016/j.apsusc.2022.156188
95. Li, Q.H., Zhang, W., Peng, J., et al.: Metal–organic framework derived ultrafine Sb@porous carbon octahedron via in situ substitution for high-performance sodium-ion batteries. ACS Nano **15**, 15104–15113 (2021). https://doi.org/10.1021/acsnano.1c05458
96. Liang, S.Z., Cheng, Y.J., Zhu, J., et al.: A chronicle review of nonsilicon (Sn, Sb, Ge)-based lithium/sodium-ion battery alloying anodes. Small Methods **4**, 2000218 (2020). https://doi.org/10.1002/smtd.202000218
97. Lao, M.M., Zhang, Y., Luo, W.B., et al.: Alloy-based anode materials toward advanced sodium-ion batteries. Adv. Mater. **29**, 1700622 (2017). https://doi.org/10.1002/adma.201700622
98. Fang, L.B., Bahlawane, N., Sun, W.P., et al.: Conversion-alloying anode materials for sodium ion batteries. Small **17**, 2101137 (2021). https://doi.org/10.1002/smll.202101137
99. Han, Y., Lin, N., Xu, T.J., et al.: An amorphous Si material with a sponge-like structure as an anode for Li-ion and Na-ion batteries. Nanoscale **10**, 3153–3158 (2018). https://doi.org/10.1039/C7NR08886H
100. Shao, L., Duan, X.Y., Li, Y., et al.: Two-dimensional planar BGe monolayer as an anode material for sodium-ion batteries. ACS Appl. Mater. Interfaces **13**, 29764–29769 (2021). https://doi.org/10.1021/acsami.1c08751
101. Shang, C., Hu, L., Luo, D., et al.: Promoting Ge alloying reaction via heterostructure engineering for high efficient and ultrastable sodium-ion storage. Adv. Sci. **7**, 2002358 (2020). https://doi.org/10.1002/advs.202002358
102. Darwiche, A., Dugas, R., Fraisse, B., et al.: Reinstating lead for high-loaded efficient negative electrode for rechargeable sodium-ion battery. J. Power Sources **304**, 1–8 (2016). https://doi.org/10.1016/j.jpowsour.2015.10.087
103. Sayed, S., Kalisvaart, W.P., Luber, E., et al.: (2020) Stabilizing tin anodes in sodium-ion batteries by alloying with silicon. ACS Appl. Energy Mater. **3**, 9950–9962 (2020). https://doi.org/10.1021/acsaem.0c01641
104. Arnold, S., Gentile, A., Li, Y., et al.: Design of high-performance antimony/MXene hybrid electrodes for sodium-ion

batteries. J. Mater. Chem. A **10**, 10569–10585 (2022). https://doi.org/10.1039/d2ta00542e
105. Yang, X.M., Zhu, Y.M., Wu, D.J., et al.: Yolk–shell antimony/carbon: scalable synthesis and structural stability study in sodium ion batteries. Adv. Funct. Mater. **32**, 2111391 (2022). https://doi.org/10.1002/adfm.202111391
106. Liu, Z.M., Sun, H.R., Wang, X.J., et al.: Tetrafunctional template-assisted strategy to preciously construct co-doped Sb@C nanofiber with longitudinal tunnels for ultralong-life and high-rate sodium storage. Energy Storage Mater. **48**, 90–100 (2022). https://doi.org/10.1016/j.ensm.2022.03.010
107. Ma, X.D., Ji, C., Li, X.K., et al.: Red@black phosphorus core–shell heterostructure with superior air stability for high-rate and durable sodium-ion battery. Mater. Today **59**, 36–45 (2022). https://doi.org/10.1016/j.mattod.2022.08.013
108. Xie, H.Z., Kalisvaart, W.P., Olsen, B.C., et al.: Sn–Bi–Sb alloys as anode materials for sodium ion batteries. J. Mater. Chem. A **5**, 9661–9670 (2017). https://doi.org/10.1039/C7TA01443K
109. Gao, H., Niu, J.Z., Zhang, C., et al.: A dealloying synthetic strategy for nanoporous bismuth–antimony anodes for sodium ion batteries. ACS Nano **12**, 3568–3577 (2018). https://doi.org/10.1021/acsnano.8b00643
110. Wang, X.X., Feng, B., Huang, L.M., et al.: Superior electrochemical performance of Sb–Bi alloy for sodium storage: Understanding from alloying element effects and new cause of capacity attenuation. J. Power. Sources **520**, 230826 (2022). https://doi.org/10.1016/j.jpowsour.2021.230826
111. Wei, X.J., Wang, X.P., Tan, X., et al.: Nanostructured conversion-type negative electrode materials for low-cost and high-performance sodium-ion batteries. Adv. Funct. Mater. **28**, 1804458 (2018). https://doi.org/10.1002/adfm.201804458
112. Thangavel, R., Samuthira Pandian, A., Ramasamy, H.V., et al.: Rapidly synthesized, few-layered pseudocapacitive SnS_2 anode for high-power sodium ion batteries. ACS Appl. Mater. Interfaces **9**, 40187–40196 (2017). https://doi.org/10.1021/acsami.7b11040
113. Li, W.H., Zeng, L.C., Yang, Z.Z., et al.: Free-standing and binder-free sodium-ion electrodes with ultralong cycle life and high rate performance based on porous carbon nanofibers. Nanoscale **6**, 693–698 (2014). https://doi.org/10.1039/C3NR05022J
114. Ma, J.Y., Guo, X.T., Yan, Y., et al.: FeO_x-based materials for electrochemical energy storage. Adv. Sci. **5**, 1700986 (2018). https://doi.org/10.1002/advs.201700986
115. Hou, T.Y., Sun, X.H., Xie, D.L., et al.: Mesoporous graphitic carbon-encapsulated Fe_2O_3 nanocomposite as high-rate anode material for sodium-ion batteries. Chem. A Eur. J. **24**, 14786–14793 (2018). https://doi.org/10.1002/chem.201802916
116. Zhong, W., Chen, Q., Liu, Z., et al.: Spindle-shaped core-shell Fe_3O_4@N-doped carbon composites scattered in graphene as excellent anode materials for lithium/sodium ion battery. J. Alloy. Compd. **832**, 154879 (2020). https://doi.org/10.1016/j.jallcom.2020.154879
117. Liu, Z., Yu, M.K., Wang, X.D., et al.: Sandwich shelled TiO_2@Co_3O_4@Co_3O_4/C hollow spheres as anode materials for lithium ion batteries. Chem. Commun. **57**, 1786–1789 (2021). https://doi.org/10.1039/d0cc07306g
118. Liu, J.N., Fu, A.P., Wang, Y.Q., et al.: Spraying coagulation-assisted hydrothermal synthesis of MoS_2/carbon/graphene composite microspheres for lithium-ion battery applications. ChemElectroChem **4**, 2027–2036 (2017). https://doi.org/10.1002/celc.201600769
119. Jing, L.Y., Kong, Z., Guo, F.A., et al.: Porous structures of carbon-doped Co_3O_4 with tunable morphologies from microflowers to cubes as anodes for high performance lithium/sodium-ion batteries. J. Alloys Compd. **881**, 160588 (2021). https://doi.org/10.1016/j.jallcom.2021.160588
120. Xu, M., Xia, Q.Y., Yue, J.L., et al.: Rambutan-like hybrid hollow spheres of carbon confined Co_3O_4 nanoparticles as advanced anode materials for sodium-ion batteries. Adv. Funct. Mater. **29**, 1807377 (2019). https://doi.org/10.1002/adfm.201807377
121. Li, L., Zheng, Y., Zhang, S.L., et al.: Recent progress on sodium ion batteries: potential high-performance anodes. Energy Environ. Sci. **11**, 2310–2340 (2018). https://doi.org/10.1039/C8EE01023D
122. Ni, J.F., Jiang, Y., Wu, F.X., et al.: Regulation of breathing CuO nanoarray electrodes for enhanced electrochemical sodium storage. Adv. Funct. Mater. **28**, 1707179 (2018). https://doi.org/10.1002/adfm.201707179
123. Zhao, J., Zhao, Y.Y., Yue, W.C., et al.: Facile fabrication of hollow CuO nanocubes for enhanced lithium/sodium storage performance. CrystEngComm **23**, 6107–6116 (2021). https://doi.org/10.1039/d1ce00704a
124. Wang, H.G., Jiang, C., Yuan, C.P., et al.: Complexing agent engineered strategy for anchoring SnO_2 nanoparticles on sulfur/nitrogen co-doped graphene for superior lithium and sodium ion storage. Chem. Eng. J. **332**, 237–244 (2018). https://doi.org/10.1016/j.cej.2017.09.081
125. Ma, D.T., Li, Y.L., Mi, H.W., et al.: Robust SnO_{2-x} nanoparticle-impregnated carbon nanofibers with outstanding electrochemical performance for advanced sodium-ion batteries. Angew. Chem. Int. Ed. **57**, 8901–8905 (2018). https://doi.org/10.1002/anie.201802672
126. Zhu, Y.Y., Nie, P., Shen, L.F., et al.: High rate capability and superior cycle stability of a flower-like Sb_2S_3 anode for high-capacity sodium ion batteries. Nanoscale **7**, 3309–3315 (2015). https://doi.org/10.1039/C4NR05242K
127. Anwer, S., Huang, Y.X., Li, B.S., et al.: Nature-inspired, graphene-wrapped 3D MoS_2 ultrathin microflower architecture as a high-performance anode material for sodium-ion batteries. ACS Appl. Mater. Interfaces **11**, 22323–22331 (2019). https://doi.org/10.1021/acsami.9b04260
128. Li, J.L., Qin, W., Xie, J.P., et al.: Rational design of MoS_2-reduced graphene oxide sponges as free-standing anodes for sodium-ion batteries. Chem. Eng. J. **332**, 260–266 (2018). https://doi.org/10.1016/j.cej.2017.09.088
129. Wang, S.T., Cao, F.J., Li, Y.T., et al.: MoS_2-coupled carbon nanosheets encapsulated on sodium titanate nanowires as superdurable anode material for sodium-ion batteries. Adv. Sci. **6**, 1900028 (2019). https://doi.org/10.1002/advs.201900028
130. Tu, F.Z., Han, Y., Du, Y.C., et al.: Hierarchical nanospheres constructed by ultrathin MoS_2 nanosheets braced on nitrogen-doped carbon polyhedra for efficient lithium and sodium storage. ACS Appl. Mater. Interfaces **11**, 2112–2119 (2019). https://doi.org/10.1021/acsami.8b19662
131. Zhang, X., Jin, Y.H., Zhang, K., et al.: Microscale and molecular regulation for molybdenum disulfide with extended layer spacing for high-performance sodium ion battery anodes. J. Power Sources **546**, 231994 (2022). https://doi.org/10.1016/j.jpowsour.2022.231994
132. Yao, K., Xu, Z.W., Huang, J.F., et al.: Bundled defect-rich MoS_2 for a high-rate and long-life sodium-ion battery: achieving 3D diffusion of sodium ion by vacancies to improve kinetics. Small **15**, 1805405 (2019). https://doi.org/10.1002/smll.201805405
133. Lim, H., Kim, H., Kim, S.O., et al.: Self-assembled N-doped MoS_2/carbon spheres by naturally occurring acid-catalyzed reaction for improved sodium-ion batteries. Chem. Eng. J. **387**, 124144 (2020). https://doi.org/10.1016/j.cej.2020.124144
134. Ye, W., Wu, F.F., Shi, N.X., et al.: Metal–semiconductor phase twinned hierarchical MoS_2 nanowires with expanded interlayers for sodium-ion batteries with ultralong cycle life. Small **16**, 1906607 (2020). https://doi.org/10.1002/smll.201906607

135. Wu, C.H., Song, H., Tang, C., et al.: Ultralarge interlayer distance and C, N-codoping enable superior sodium storage capabilities of MoS_2 nanoonions. Chem. Eng. J. **378**, 122249 (2019). https://doi.org/10.1016/j.cej.2019.122249
136. Li, B.S., Wang, R.R., Chen, Z.L., et al.: Embedding heterostructured MnS/$Co_{1-x}S$ nanoparticles in porous carbon/graphene for superior lithium storage. J. Mater. Chem. A **7**, 1260–1266 (2019). https://doi.org/10.1039/C8TA09740B
137. Zhan, J., Wu, K., Yu, X., et al.: α-Fe_2O_3 nanoparticles decorated C@MoS_2 nanosheet arrays with expanded spacing of (002) plane for ultrafast and high Li/Na-ion storage. Small **15**, 1901083 (2019). https://doi.org/10.1002/smll.201901083
138. Cao, L., Liang, X.H., Ou, X., et al.: Heterointerface engineering of hierarchical Bi_2S_3/MoS_2 with self-generated rich phase boundaries for superior sodium storage performance. Adv. Funct. Mater. **30**, 10732 (2020). https://doi.org/10.1002/adfm.201910732
139. Yang, K., Mei, T., Chen, Z.H., et al.: Chinese hydrangea lantern-like Co_9S_8@MoS_2composites with enhanced lithium-ion battery properties. Nanoscale **12**, 3435–3442 (2020). https://doi.org/10.1039/c9nr09260a
140. Chen, F.Z., Shi, D., Yang, M.Z., et al.: Novel designed MnS-MoS_2 heterostructure for fast and stable Li/Na storage: insights into the advanced mechanism attributed to phase engineering. Adv. Funct. Mater. **31**, 2007132 (2021). https://doi.org/10.1002/adfm.202007132
141. Chen, J.J., Ling, M.Y., Wan, L.Y., et al.: The construction of molybdenum disulfide/cobalt selenide heterostructures @ N-doped carbon for stable and high-rate sodium storage. J. Energy Chem. **71**, 1–11 (2022). https://doi.org/10.1016/j.jechem.2022.03.033
142. Wang, S.W., Jing, Y.P., Han, L.F., et al.: Ultrathin carbon-coated FeS_2 nanooctahedra for sodium storage with long cycling stability. Inorg. Chem. Front. **6**, 459–464 (2019). https://doi.org/10.1039/C8QI01144C
143. Lin, Z.H., Xiong, X.H., Fan, M.N., et al.: Scalable synthesis of FeS_2 nanoparticles encapsulated into N-doped carbon nanosheets as a high-performance sodium-ion battery anode. Nanoscale **11**, 3773–3779 (2019). https://doi.org/10.1039/c8nr10444a
144. Chen, Y.Y., Hu, X.D., Evanko, B., et al.: High-rate FeS_2/CNT neural network nanostructure composite anodes for stable, high-capacity sodium-ion batteries. Nano Energy **46**, 117–127 (2018). https://doi.org/10.1016/j.nanoen.2018.01.039
145. Zhao, W.X., Guo, C.X., Li, C.M.: Lychee-like FeS_2@$FeSe_2$ core–shell microspheres anode in sodium ion batteries for large capacity and ultralong cycle life. J. Mater. Chem. A **5**, 19195–19202 (2017). https://doi.org/10.1039/C7TA05931K
146. Hu, Z., Zhu, Z.Q., Cheng, F.Y., et al.: Pyrite FeS_2 for high-rate and long-life rechargeable sodium batteries. Energy Environ. Sci. **8**, 1309–1316 (2015). https://doi.org/10.1039/C4EE03759F
147. Yang, D., Chen, W.H., Zhang, X.X., et al.: Facile and scalable synthesis of low-cost FeS@C as long-cycle anodes for sodium-ion batteries. J. Mater. Chem. A **7**, 19709–19718 (2019). https://doi.org/10.1039/c9ta05664e
148. Chen, W.H., Qi, S.H., Yu, M.M., et al.: Design of FeS_2@rGO composite with enhanced rate and cyclic performances for sodium ion batteries. Electrochim. Acta **230**, 1–9 (2017). https://doi.org/10.1016/j.electacta.2017.01.176
149. Chen, W.H., Qi, S.H., Guan, L.Q., et al.: Pyrite FeS_2 microspheres anchoring on reduced graphene oxide aerogel as an enhanced electrode material for sodium-ion batteries. J. Mater. Chem. A **5**, 5332–5341 (2017). https://doi.org/10.1039/C7TA00114B
150. Lu, Z.X., Zhai, Y.J., Wang, N.N., et al.: FeS_2 nanoparticles embedded in N/S co-doped porous carbon fibers as anode for sodium-ion batteries. Chem. Eng. J. **380**, 122455 (2020). https://doi.org/10.1016/j.cej.2019.122455
151. Zhai, X.G., Zuo, Z.C., Xiong, Z.C., et al.: Large-scale CuS nanotube arrays@graphdiyne for high-performance sodium ion battery. 2D Mater. **9**, 025024 (2022). https://doi.org/10.1088/2053-1583/ac5d84
152. Shuang, W., Huang, H., Liu, M., et al.: Engineering of CuS_x@C derived from Cu-MOF as long-life anodes for sodium-ion batteries. J. Solid State Chem. **302**, 122348 (2021). https://doi.org/10.1016/j.jssc.2021.122348
153. Wu, Y.J., Shuang, W., Wang, Y., et al.: Implementation of structural and surface engineering strategies to copper sulfide for enhanced sodium-ion storage. J. Alloys Compd. **923**, 166308 (2022). https://doi.org/10.1016/j.jallcom.2022.166308
154. Han, Y., Huang, G.Y., Xu, S.M.: Structural reorganization–based nanomaterials as anodes for lithium-ion batteries: design, preparation, and performance. Small **16**, 1902841 (2020). https://doi.org/10.1002/smll.201902841
155. Xiong, X.H., Yang, C.H., Wang, G.H., et al.: SnS nanoparticles electrostatically anchored on three-dimensional N-doped graphene as an active and durable anode for sodium-ion batteries. Energy Environ. Sci. **10**, 1757–1763 (2017). https://doi.org/10.1039/C7EE01628J
156. Sang, Z.Y., Yan, X., Su, D., et al.: A flexible film with SnS_2 nanoparticles chemically anchored on 3D-graphene framework for high areal density and high rate sodium storage. Small **16**, 2001265 (2020). https://doi.org/10.1002/smll.202001265
157. Li, X., Sun, X.H., Gao, Z.W., et al.: A simple one-pot strategy for synthesizing ultrafine SnS_2 nanoparticle/graphene composites as anodes for lithium/sodium-ion batteries. Chemsuschem **11**, 1549–1557 (2018). https://doi.org/10.1002/cssc.201800073
158. Wang, Y.Y., Zhou, J.H., Wu, J.H., et al.: Engineering SnS_2 nanosheet assemblies for enhanced electrochemical lithium and sodium ion storage. J. Mater. Chem. A **5**, 25618–25624 (2017). https://doi.org/10.1039/C7TA08056E
159. Chen, Q., Lu, F.Q., Xia, Y., et al.: Interlayer expansion of few-layered Mo-doped SnS_2 nanosheets grown on carbon cloth with excellent lithium storage performance for lithium ion batteries. J. Mater. Chem. A **5**, 4075–4083 (2017). https://doi.org/10.1039/C7TA00236J
160. Wang, L.Q., Zhao, Q.Q., Wang, Z.T., et al.: Cobalt-doping SnS_2 nanosheets towards high-performance anodes for sodium ion batteries. Nanoscale **12**, 248–255 (2020). https://doi.org/10.1039/c9nr07849e
161. Choi, H., Lee, S., Eom, K.: Facile phosphorus-embedding into SnS_2 using a high-energy ball mill to improve the surface kinetics of P-SnS_2 anodes for a Li-ion battery. Appl. Surf. Sci. **466**, 578–582 (2019). https://doi.org/10.1016/j.apsusc.2018.09.241
162. Yang, Z.Y., Zhang, P., Wang, J., et al.: Hierarchical carbon@SnS_2 aerogel with "skeleton/skin" architectures as a high-capacity, high-rate capability and long cycle life anode for sodium ion storage. ACS Appl. Mater. Interfaces **10**, 37434–37444 (2018). https://doi.org/10.1021/acsami.8b14861
163. Li, J.H., Han, S.B., Zhang, C.Y., et al.: High-performance and reactivation characteristics of high-quality, graphene-supported SnS_2 heterojunctions for a lithium-ion battery anode. ACS Appl. Mater. Interfaces **11**, 22314–22322 (2019). https://doi.org/10.1021/acsami.9b04243
164. Cheng, Y.Y., Xie, H., Zhou, L., et al.: In-situ liquid-phase transformation of SnS_2/CNTs composite from SnO_2/CNTs for high performance lithium-ion battery anode. Appl. Surf. Sci. **566**, 150645 (2021). https://doi.org/10.1016/j.apsusc.2021.150645
165. Wang, L., Li, X.F., Jin, Z.Z., et al.: Spatially controlled synthesis of superlattice-like SnS/nitrogen-doped graphene hybrid nanobelts as high-rate and durable anode materials for sodium-ion batteries. J. Mater. Chem. A **7**, 27475–27483 (2019). https://doi.org/10.1039/c9ta08945d

166. Cui, Z., He, S.A., Liu, Q., et al.: Graphene-like carbon film wrapped tin (II) sulfide nanosheet arrays on porous carbon fibers with enhanced electrochemical kinetics as high-performance Li and Na ion battery anodes. Adv. Sci. **7**, 1903045 (2020). https://doi.org/10.1002/advs.201903045
167. Lu, J.M., Zhao, S.Y., Fan, S.X., et al.: Hierarchical SnS/SnS_2 heterostructures grown on carbon cloth as binder-free anode for superior sodium-ion storage. Carbon **148**, 525–531 (2019). https://doi.org/10.1016/j.carbon.2019.03.022
168. Daglar, H., Gulbalkan, H.C., Avci, G., et al.: Effect of metal–organic framework (MOF) database selection on the assessment of gas storage and separation potentials of MOFs. Angew. Chem. Int. Ed. **60**, 7828–7837 (2021). https://doi.org/10.1002/anie.202015250
169. Ahmad, A., Khan, S., Tariq, S., et al.: Self-sacrifice MOFs for heterogeneous catalysis: synthesis mechanisms and future perspectives. Mater. Today **55**, 137–169 (2022). https://doi.org/10.1016/j.mattod.2022.04.002
170. Liang, Z.B., Qu, C., Guo, W.H., et al.: Metal-organic frameworks: Pristine metal–organic frameworks and their composites for energy storage and conversion. Adv. Mater. **30**, 1702891 (2018). https://doi.org/10.1002/adma.201702891
171. Wang, J.J., Yue, X.Y., Xie, Z.K., et al.: MOFs-derived transition metal sulfide composites for advanced sodium ion batteries. Energy Storage Mater. **41**, 404–426 (2021). https://doi.org/10.1016/j.ensm.2021.06.025
172. Zhong, M., Kong, L.J., Li, N., et al.: Synthesis of MOF-derived nanostructures and their applications as anodes in lithium and sodium ion batteries. Coord. Chem. Rev. **388**, 172–201 (2019). https://doi.org/10.1016/j.ccr.2019.02.029
173. Hu, C., Xiao, J.D., Mao, X.D., et al.: Toughening mechanisms of epoxy resin using aminated metal-organic framework as additive. Mater. Lett. **240**, 113–116 (2019). https://doi.org/10.1016/j.matlet.2018.12.123
174. Abazari, R., Mahjoub, A.R., Shariati, J.: Synthesis of a nanostructured pillar MOF with high adsorption capacity towards antibiotics pollutants from aqueous solution. J. Hazard. Mater. **366**, 439–451 (2019). https://doi.org/10.1016/j.jhazmat.2018.12.030
175. Li, J.P., Cheng, S.J., Zhao, Q., et al.: Synthesis and hydrogen-storage behavior of metal-organic framework MOF-5. Int. J. Hydrog. Energy **34**, 1377–1382 (2009). https://doi.org/10.1016/j.ijhydene.2008.11.048
176. Areerob, Y., Cho, J.Y., Jang, W.K., et al.: Enhanced sonocatalytic degradation of organic dyes from aqueous solutions by novel synthesis of mesoporous Fe_3O_4-graphene/ZnO@SiO_2 nanocomposites. Ultrason. Sonochem. **41**, 267–278 (2018). https://doi.org/10.1016/j.ultsonch.2017.09.034
177. Annamalai, J., Murugan, P., Ganapathy, D., et al.: Synthesis of various dimensional metal organic frameworks (MOFs) and their hybrid composites for emerging applications: a review. Chemosphere **298**, 134184 (2022). https://doi.org/10.1016/j.chemosphere.2022.134184
178. Dong, C.F., Xu, L.Q.: Cobalt- and cadmium-based metal–organic frameworks as high-performance anodes for sodium ion batteries and lithium ion batteries. ACS Appl. Mater. Interfaces **9**, 7160–7168 (2017). https://doi.org/10.1021/acsami.6b15757
179. Liu, Y.J., Zhao, X.L., Fang, C., et al.: Activating aromatic rings as Na-ion storage sites to achieve high capacity. Chem **4**, 2463–2478 (2018). https://doi.org/10.1016/j.chempr.2018.08.015
180. Wang, L.B., Ni, Y.X., Hou, X.S., et al.: A two-dimensional metal–organic polymer enabled by robust nickel–nitrogen and hydrogen bonds for exceptional sodium-ion storage. Angew. Chem. Int. Ed. **59**, 22126–22131 (2020). https://doi.org/10.1002/anie.202008726
181. Chen, Y., Tang, M., Wu, Y.C., et al.: A one-dimensional π–d conjugated coordination polymer for sodium storage with catalytic activity in negishi coupling. Angew. Chem. Int. Ed. **58**, 14731–14739 (2019). https://doi.org/10.1002/anie.201908274
182. Shuang, W., Wang, Y., Chen, F.Y., et al.: Engineering the modulation of the active sites and pores of pristine metal–organic frameworks for high-performance sodium-ion storage. Inorg. Chem. Front. **10**, 396–405 (2023). https://doi.org/10.1039/D2QI02117J
183. Li, C., Yang, Q., Shen, M., et al.: The electrochemical Na intercalation/extraction mechanism of ultrathin cobalt(II) terephthalate-based MOF nanosheets revealed by synchrotron X-ray absorption spectroscopy. Energy Storage Mater. **14**, 82–89 (2018). https://doi.org/10.1016/j.ensm.2018.02.021
184. Yin, X., Lv, L.P., Tang, X., et al.: Designing cobalt-based coordination polymers for high-performance sodium and lithium storage: from controllable synthesis to mechanism detection. Mater. Today Energy **17**, 100478 (2020). https://doi.org/10.1016/j.mtener.2020.100478
185. Park, J., Lee, M., Feng, D.W., et al.: Stabilization of hexaaminobenzene in a 2D conductive metal-organic framework for high power sodium storage. J. Am. Chem. Soc. **140**, 10315–10323 (2018). https://doi.org/10.1021/jacs.8b06020
186. Zhang, Y., Yang, S.H., Chang, X.Y., et al.: MOF based on a longer linear ligand: electrochemical performance, reaction kinetics, and use as a novel anode material for sodium-ion batteries. Chem. Commun. **54**, 11793–11796 (2018). https://doi.org/10.1039/C8CC06248J
187. Yi, X.L., Li, X.H., Zhong, J., et al.: Unraveling the mechanism of different kinetics performance between ether and carbonate ester electrolytes in hard carbon electrode. Adv. Funct. Mater. **32**, 2209523 (2022). https://doi.org/10.1002/adfm.202209523
188. Wen, L.Z., Wang, L., Guan, Z.W., et al.: Effect of composite conductive agent on internal resistance and performance of lithium iron phosphate batteries. Ionics **28**, 3145–3153 (2022). https://doi.org/10.1007/s11581-022-04491-w
189. Yang, M., Chang, X.Q., Wang, L.Q., et al.: Interface modulation of metal sulfide anodes for long-cycle-life sodium-ion batteries. Adv. Mater. **35**, e2208705 (2023). https://doi.org/10.1002/adma.202208705
190. Jin, Y., Le, P.M.L., Gao, P.Y., et al.: Low-solvation electrolytes for high-voltage sodium-ion batteries. Nat. Energy **7**, 718–725 (2022). https://doi.org/10.1038/s41560-022-01055-0
191. Wu, Y.W., Shen, J.D., Sun, Z.Y., et al.: Nine-electron transfer of binder synergistic π-d conjugated coordination polymers as high-performance lithium storage materials. Angew. Chem. Int. Ed. **62**, e202215864 (2023). https://doi.org/10.1002/anie.202215864
192. Li, R.R., Yang, Z., He, X.X., et al.: Binders for sodium-ion batteries: progress, challenges and strategies. Chem. Commun. **57**, 12406–12416 (2021). https://doi.org/10.1039/d1cc04563f
193. Gu, Z.Y., Sun, Z.H., Guo, J.Z., et al.: High-rate and long-cycle cathode for sodium-ion batteries: enhanced electrode stability and kinetics via binder adjustment. ACS Appl. Mater. Interfaces **12**, 47580–47589 (2020). https://doi.org/10.1021/acsami.0c14294
194. Yao, Q., Zhu, Y.S., Zheng, C., et al.: Intermolecular cross-linking reinforces polymer binders for durable alloy-type anode materials of sodium-ion batteries. Adv. Energy Mater. **13**, 2202939 (2023). https://doi.org/10.1002/aenm.202202939
195. Xia, J.L., Lu, A.H., Yu, X.F., et al.: Rational design of a trifunctional binder for hard carbon anodes showing high initial coulombic efficiency and superior rate capability for sodium-ion batteries. Adv. Funct. Mater. **31**, 2104137 (2021). https://doi.org/10.1002/adfm.202104137
196. Yang, J.L., Zhao, X.X., Zhang, W., et al.: Inside back cover: "pore-hopping" ion transport in cellulose-based separator

towards high-performance sodium-ion batteries (angew. Chem. Int. ed. 15/2023). Angew. Chem. Int. Ed. **62**, 258 (2023). https://doi.org/10.1002/anie.202302568
197. Li, X.L., Zhang, J.Y., Guo, X.N., et al.: An ultrathin nonporous polymer separator regulates Na transfer toward dendrite-free sodium storage batteries. Adv. Mater. **35**, e2203547 (2023). https://doi.org/10.1002/adma.202203547
198. Shi, C.H., Wang, L.G., Chen, X.A., et al.: Challenges of layer-structured cathodes for sodium-ion batteries. Nanoscale Horiz. **7**, 338–351 (2022). https://doi.org/10.1039/d1nh00585e
199. Ren, H.X., Li, Y., Ni, Q., et al.: Unraveling anionic redox for sodium layered oxide cathodes: breakthroughs and perspectives. Adv. Mater. **34**, 2106171 (2022). https://doi.org/10.1002/adma.202106171
200. Chen, T., Ouyang, B.X., Fan, X.W., et al.: Oxide cathodes for sodium-ion batteries: designs, challenges, and perspectives. Carbon Energy **4**, 170–199 (2022). https://doi.org/10.1002/cey2.153
201. Jin, T., Li, H.X., Zhu, K.J., et al.: Polyanion-type cathode materials for sodium-ion batteries. Chem. Soc. Rev. **49**, 2342–2377 (2020). https://doi.org/10.1039/c9cs00846b
202. Chen, M.Z., Liu, Q.N., Zhang, Y.Y., et al.: Emerging polyanionic and organic compounds for high energy density, non-aqueous potassium-ion batteries. J. Mater. Chem. A **8**, 16061–16080 (2020). https://doi.org/10.1039/C9TA11221A
203. Xie, B.X., Sun, B.Y., Gao, T.Y., et al.: Recent progress of Prussian blue analogues as cathode materials for nonaqueous sodium-ion batteries. Coord. Chem. Rev. **460**, 214478 (2022). https://doi.org/10.1016/j.ccr.2022.214478
204. Wu, Y.J., Yuan, Y.F., Shuang, W., et al.: Reducing carbonaceous salts for facile fabrication of monolayer graphene. Small Methods **7**, 2201596 (2023). https://doi.org/10.1002/smtd.202201596

Yujun Wu received his B.S. degree (2013) and M.S. degree (2016) from Henan Normal University. He obtained his Ph.D. degree from Beijing Institute of Technology in 2020. He did a three-year postdoctoral work in Henan Normal University under the supervision of Prof. Lin Yang. He joined the School of Chemistry and Chemical Engineering in Henan normal university in 2023. His main research focuses on nanomaterials for energy storage and conversion devices.

Wei Shuang received her B.S. degree in 2013 and M.S. degree in 2016 from Henan Normal University under the supervision of Prof. Lin Yang. She obtained her Ph.D. degree in 2020 from Nankai University under the supervision of Prof. Xian-He Bu. She joined the School of Chemistry and Chemical Engineering in Henan normal university in 2020. Her main research focuses on MOFs-based materials for energy storage and conversion devices.

Ya Wang is presently a graduate student in Prof. Lin Yang's group at Henan Normal University. Her main research interest is about anode materials for energy storage and conversion devices.

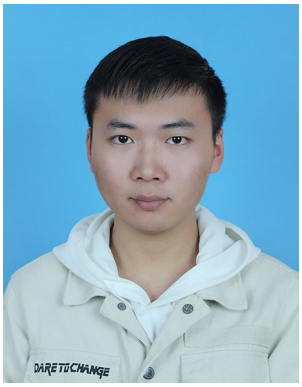

Fuyou Chen is presently a graduate student in Prof. Lin Yang's group at Henan Normal University. His main research interest is about anode materials for energy storage and conversion devices.

Shaobing Tang is presently a graduate student in Prof. Lin Yang's group at Henan Normal University. His main research interest is about nanomaterials for energy storage and conversion devices.

Xing-Long Wu is currently a professor at Northeast Normal University, China. He received his Ph.D. degree from the Institute of Chemistry, Chinese Academy of Sciences (ICCAS), in 2011. After continuing a two-year postdoctoral work in ICCAS, he moved to Northeast Normal University as an associate professor in 2013 and became full professor in 2018. His current research interests focus on high-performance materials for advanced secondary batteries such as Na-/K-/Li-ion batteries and dual-ion batteries, as well as the reuse and recycle of spent Li-ion batteries.

Zhengyu Bai is a professor at the School of Chemistry and Chemical Engineering at Henan Normal University. She obtained her Ph.D. degree in 2010 from Henan Normal University. Dr. Bai has published over 56 peer-reviewed journal articles. She is also listed as an inventor on 25 national patents, with 8 patents licensed in China. She received the Distinguished Young Investigator Awards at the 4th International Conference on Electrochemical Energy Science and Technology 2018 (EEST 2018). Her research is focused on new green energy nanomaterials, such as nanostructured electrocatalysts for fuel cell and metal-air batteries.

Lin Yang is a professor, Ph.D. supervisor and academic leader at Henan Normal University, China. He received his Ph.D. degree in Physical Chemistry from Lanzhou Institute of Chemical Physics of CAS. Dr. Yang is the vice president of Henan Normal University from 2008 and the associate director of the Key Laboratory of Green Chemical Media and Reactions, Ministry of Education. He was engaged in scientific research in Germany at TU Braunschweig during 1989–1991 and at University of Halle during 1994–1995. The technical expertise areas of Dr. Yang are new materials of electrochemical energy and inorganic/organic hybrid nanomaterials.

Jiujun Zhang is a professor at College of Materials Science and Engineering, Fuzhou University and Institute for Sustainable Energy, Shanghai University. Dr. Zhang is the former principal research officer at the National Research Council of Canada (NRC). Dr. Zhang is a Fellow of the Canadian Academy of Engineering (FCAE), Fellow of the Academy of Science of the Royal Society of Canada (FRSC-CA), Fellow of the Engineering Institute of Canada (FEIC), Fellow of the International Society of Electrochemistry (FISE), and Fellow of the Royal Society of Chemistry (FRSC-UK). Dr. Zhang's main research areas are electrochemistry, electrocatalysts, fuel cells, lithium batteries, metal-air batteries, supercapacitors and $H_2O/CO_2/N_2$ electrolysis.